ALMA MATER STUDIORUM - UNIVERSITÀ DI BOLOGNA

FACOLTÀ DI SCIENZE MATEMATICHE, FISICHE E NATURALI
Dottorato di Ricerca in Fisica - Ciclo XXII - FIS/01

Measurement of top quark pairs production cross-section in the semi-leptonic channel with the ATLAS experiment

Presentata da: Riccardo Di Sipio

Coordinatore di Dottorato
prof. FABIO ORTOLANI

Relatore:
Prof. ANTONIO ZOCCOLI

Correlatori:
dr. Lorenzo Bellagamba
dr. Graziano Bruni

Esame Finale anno 2010

To Elena

To boldly go
where no man has gone before

Contents

Introduction

The Large Hadron Collider (LHC) is entering its first phase of physics run. The objective over the first 18 to 24 months is to deliver one inverse femtobarn of data to the experiments, enough to make significant advances in several physics channels. The first months will be very important for the commissioning of the detector and its computing support, and top quarks will play a significant role. In fact, thanks to the complex topology of their decays, most of the sub-detectors of which ATLAS is composed will perform together, triggering events with charged leptons, reconstructing particle jets and calculating the missing transverse energy. To some extent, an accurate description of the decay of the top quark pairs is a majestic accomplishment of the Standard Model. Measuring their properties at a new energy range will be an important step to take before the eventual leap toward new territories that could lie ahead.

This thesis is about three major aspects of the identification of top quarks. First comes the understanding of their production mechanism, their decay channels and how to translate theoretical formulae into programs that can simulate such physical processes using Monte Carlo techniques. In particular, the author has been involved in the introduction of the POWHEG generator in the framework of the ATLAS experiment. POWHEG is now fully used as the benchmark program for the simulation of $t\bar{t}$ pairs production and decay, along with MC@NLO and AcerMC: this will be shown in chapter one. The second chapter illustrates the ATLAS detectors and its sub-units, such as calorimeters and muon chambers. It is very important to evaluate their efficiency in order to fully understand what happens during the passage of radiation through the detector and to use this knowledge in the calculation of final quantities such as the $t\bar{t}$ production cross section. The last part of this thesis concerns the eval-

uation of this quantity deploying the so-called "golden channel" of $t\bar{t}$ decays, yielding one energetic charged lepton, four particle jets and a relevant quantity of missing transverse energy due to the neutrino. The most important systematic errors arising from the various part of the calculation are studied in detail. Jet energy scale, trigger efficiency, Monte Carlo models, reconstruction algorithms and luminosity measurement are examples of what can contribute to the uncertainty about the cross-section.

Chapter 1

Top Quark Physics and Monte Carlo Generation

1.1 Top Quark and its Decay Channels

1.1.1 Discovery of the top quark

In 1964 Murray Gell-Mann and George Zweig proposed the "quark hypothesis" to explain the so-called particle zoo: At that time, more than one hundred particles, called hadrons, had been observed in cosmic rays and particle accelerators, most of them very short-lived and strongly interacting. The quark hypothesis suggested that hadrons were not elementary particles, but had an internal structure that could be rearranged during the decay processes. The two researchers suggested that three objects, the up (u), down (d) and strange (s) quarks were sufficient to explain most of the observed phenomenology. Each quark must had a $1/2$ spin and electric charge multiple of $1/3e$. This model gained popularity since the predicted states of quark/antiquark (*mesons*) and three quark groups (*baryons*) agreed remarkably well with the observed spectrum. Moreover, quarks shared with the known leptons (the electron e, the muon μ and their neutral partners ν_e and ν_μ) both the elementariness and the spin. However, this theory was far from convincing: The fractional electric charge seemed quite bizarre, no quark had ever been observed outside an hadron (and so it is at present) and the difference in number of leptons (4) and quark (3) gave rise to several conceptual problems.

Other major experiments provided more hints during the 70s: The deep inelastic scattering (DIS), *i.e.* the interaction of high-energy leptons with nucleons at rest in the laboratory frame, proved that they had an internal structure made of point-like objects with spin and charge identical of the hypothesized quarks. In 1974, scientists at SLAC discovered the J/ψ meson, which proved to be constituted of a quark/antiquark pair of a "new" quark, now called charm (c), as predicted by Nicola Cabibbo. This situation changed suddenly as a third lepton, called tau (τ), was discovered again at SLAC. A year later, a new meson discovered at Fermilab, very similar to the J/ψ but much more massive, called upsilon (Υ), confirmed the existence of a new flavor of quarks, called beauty or bottom (b). Physicists at DESY measured its spin and electric charge, that are the same of the up and strange quarks. At this point, it was straightforward to classify quarks and leptons in three generations (see table 1.1). But a quark was still missing in the third generation: the top quark (t).

Table 1.1: The three generations of matter constituents: Quarks and Leptons

	Charge	**First Generation**	**Second Generation**	**Third Generation**
Quarks	$+2/3$	up (u)	charm (c)	top (t)
	$-1/3$	down (d)	strange (s)	bottom (b)
Leptons	-1	electron (e)	muon (μ)	tau (τ)
	0	electron neutrino (ν_e)	muon neutrino (ν_μ)	tau neutrino (ν_τ)

At first, physicists started looking for a $t\bar{t}$ meson at about $30\ GeV$, but neither PEP nor PETRA managed to find this phantom meson [22]. Was it more massive? High hopes were put in a new generation of accelerators: With the *Super Proton Synchrotron* (SPS) at CERN, a center of mass energy of $600\ GeV$ could be achieved[1], so if the $t\bar{t}$ meson existed, it should have materialized at some point. Another possibility was given by the decay of the W and Z bosons, discovered with the SPS in 1983, for instance in $Z \rightarrow t\bar{t}$ or $W \rightarrow t\bar{b}$. None of the three possibilities yielded the top quark. However, experiments demonstrated another property of quarks, their ability to produce collimated streams of hadrons. Although quarks cannot be extracted from bound states, they can

[1] An upgrade raised this number to the actual $900\ GeV$.

be accelerated via scattering, and this process gives rise to a subsequent production of more quark-antiquark pairs that combine into hadrons along the axis of the original quark. A cluster of such hadrons is called "particle jet", and it played a key role in the observation of the first top quarks.

In 1988, Fermilab turned on its new superconducting $\sqrt{s} = 1.8TeV$ collider called Tevatron: The experiments CDF and D0 aimed at detecting a direct production of $t\bar{t}$ pairs decaying into observable final state particles, such as leptons and particle jets. A key feature of CDF was the inner tracker, tailored to detect B mesons flying through it. Typically, a B meson can survive for a distance of $d = c\gamma\tau \sim 3mm$, that can be measured inside the detector with good precision. Conversely, if a track is detected with a measured lifetime compatible with the one of the B meson ($\sim 10^{-12}s$), and a jet is found whose tracks intersect into a point which is not the interacting point (a *secondary vertex*), these informations can be used to "tag" a particle jet as originated from the decay of B meson, which contains a b quark.

With the run of 1992-1993, D0 published the last lower-limit of 131 GeV for the t quark. Finally, in 1995, Fermilab announced the observation of 12 candidate events that could not be ascribed to any known background. Top quark mass was estimated to be $175 \pm 20\, GeV$, with a $t\bar{t}$ production cross section in the order of $13pb$. Later on the same year a paper was submitted to *Physical Review Letters*, reporting 6 di-lepton and 43 single-lepton events with a probability of one in a million that these events were generated by a statistical fluctuation of the background. Top quark mass was estimated to be $176 \pm 8 \pm 10\, GeV$ with a $t\bar{t}$ production cross-section of $6.8^{+3.6}_{-2.4}pb$ [31].

At present, a large number of papers have been published concerning the determination of the properties of the top quark. As usual, the most recent and accurate values can be found on the *Particle Data Book*. For convenience, quark properties are shown in table 1.2.

Is this the end of the story? One can naturally wonder if at least a fourth generation of quarks and leptons exists. In fact, the number of families is not fixed by the general theory of the Standard Model. It has been proved that the asymptotic freedom of QCD constraints the number of quark families to be less than 9. The measurement at LEP of the Z boson decay width is consistent with only 3 types of light ($m_\nu << m_Z$) neutrinos [33], leaving room for a

Table 1.2: Quark properties as in PDG2008

Quark	mass	charge	$\mathbf{I(J^P)}$
u	$1.5 - 3.3 MeV$	$+2/3e$	$\frac{1}{2}(\frac{1}{2}^+)$
d	$3.5 - 6.0 MeV$	$-1/3e$	$\frac{1}{2}(\frac{1}{2}^+)$
c	$1.27^{+0.07}_{-0.11}\ GeV$	$+2/3e$	$0(\frac{1}{2}^+)$
s	$104^{+26}_{-34} MeV$	$-1/3e$	$0(\frac{1}{2}^+)$
t	$171.2 \pm 2.1\ GeV$	$+2/3e$	$0(\frac{1}{2}^+)$
b	$4.20^{+0.17}_{-0.07}\ GeV$	$-1/3e$	$0(\frac{1}{2}^+)$

quite unlikely "sterile" neutrino which does not interact via Z boson exchange. However, neutrino oscillations suggest a new mass scale that is beyond the Standard Model and the possibility of additional heavier neutrinos cannot be excluded so easily [41]. The current 95% CL mass limits from the PDG are [33]:

$$\begin{aligned} m_{b'} &> 199\ GeV \\ m_{t'} &> 256\ GeV \\ m_{\tau'} &> 100.8\ GeV \end{aligned}$$

1.1.2 Top quark pair production at the Tevatron and at the LHC

Events in which top-quark pairs are produced will be extremely important at the LHC, as they will provide a unique environment to study physics within the Standard Model and beyond [13]. Top quark decays (see section 1.1.3) produce complex signatures within the detector, involving missing transverse energy, charged leptons, light-particle jets and b-jets. Therefore, in order to study these events accurately at the LHC, the understanding of all the parts of the detectors is mandatory, as for instance the trigger system, lepton and jet reconstruction, the measurement of missing transverse energy, reconstruction of vertices and b-tagging. Due to its rich topology and thanks to its large cross-section ($\sigma_{t\bar{t}} \sim 830\ pb$ at $\sqrt{s} = 14 TeV$, more than 100 times larger than at the Tevatron) the top quark production will also play a crucial role in detector studies and calibrations in the first phase of LHC commissioning [9].

Top quarks, other than this, could be the major *Standard Model* background to discoveries of "new" physics. In particular, $t\bar{t}$ could be produced via some resonant channel [49] at very high mass range, never explored before.

We briefly discuss the kinematics of heavy quark production at hadron colliders. In the centre-of-mass frame of the two incoming hadrons, the momenta of the colliding partons read (in the collinear approximation):

$$\begin{aligned} p_1 &= \frac{\sqrt{s}}{2}(x_1, 0, 0, x_2)\,, \\ p_2 &= \frac{\sqrt{s}}{2}(x_2, 0, 0, -x_2)\,, \end{aligned} \tag{1.1}$$

where s is the square of the hadron-hadron centre-of-mass energy and x_1 and x_2 the fractions of the parent hadrons carried by the colliding quarks. The square of the parton centre-of-mass energy is $\hat{s} = x_1 x_2 s$. The 4-momentum $p = (E, \vec{p}_T, p_z)$ of a particle of mass m can be parametrized in terms of its rapidity y and tranverse mass m_T, defined by:

$$\begin{aligned} y &= \frac{1}{2}\ln\frac{E+p_z}{E-p_z} \\ m_T &= \sqrt{m^2+p_T^2}\,. \end{aligned} \tag{1.2}$$

From eq. (1.2) one gets:

$$p = (m_T \cosh y, \vec{p}_T, m_T \sinh y)\,. \tag{1.3}$$

Using this representation for the 4-momenta of the heavy quarks (say t and $\bar{t}$) and using momentum conservation we arrive at:

$$\begin{aligned} x_1 &= \frac{m_T}{\sqrt{s}}(e^{y_t} + e^{y_{\bar{t}}}) \\ x_2 &= \frac{m_T}{\sqrt{s}}(e^{-y_t} + e^{-y_{\bar{t}}})\,. \end{aligned} \tag{1.4}$$

From eq. (1.4) one can see how the dependence on the partons pdfs vary when producing different heavy quarks (the range being from $m_c \simeq 1.5\,GeV$ and $m_t \simeq 175\,GeV$) or at different collider energies trough the $\sim 1/\sqrt{s}$ dependence.

There are two main production channels for quark-antiquark pairs at leading order, *i.e.* gluon-gluon fusion and quark-antiquark annihilation (Fig. 1.2). Given the average parton momentum fraction (x) for each collider, at the Tevatron top quark pairs are produced mainly through quark-antiquark annihilation (85% of the times at $\sqrt{s} = 1.8TeV$) [27] while at the LHC the most common production mechanism will be gluon-gluon fusion, which accounts for 90% of the total cross section. Evolution of the cross-sections *w.r.t.* $\sqrt{s}$ for various important processes are shown in figure 1.1.

Table 1.3 shows the evolution of the $t\bar{t}$ production cross section evaluated at NLO with increasing values of the center of mass energy for pp and $p\overline{p}$ interactions. Values are plotted in figure 1.4. Figure 1.5 shows the relative contribution of each production channel for pp and $p\overline{p}$ colliders as calculated at *next-to-leading order* with POWHEG-hvq [35]. At NLO other processes appear, because of the emission of a quark/gluon in the initial state or in the final state radiation. Examples are given in figure 1.3.

Table 1.3: $t\bar{t}$ production cross-section at NLO

$\sqrt{s}\ [TeV]$	pp [pb]	$p\overline{p}$ [pb]
1.8	1.178	5.328 ± 0.003
3	10.36	20.92 ± 0.01
4	28.20 ± 0.02	42.42 ± 0.03
5	56.98 ± 0.02	73.60 ± 0.05
6	97.45 ± 0.08	115.6 ± 0.09
7	149.8 ± 0.1	169.0 ± 0.1
8	214.3 ± 0.2	234.0 ± 0.2
9	290.4 ± 0.3	310.5 ± 0.3
10	378.1 ± 0.3	398.4 ± 0.3
11	477.0 ± 0.4	497.3 ± 0.4
12	586.8 ± 0.5	607.0 ± 0.5
13	707.1 ± 0.7	727.3 ± 0.7
14	837.6 ± 0.8	857.6 ± 0.8

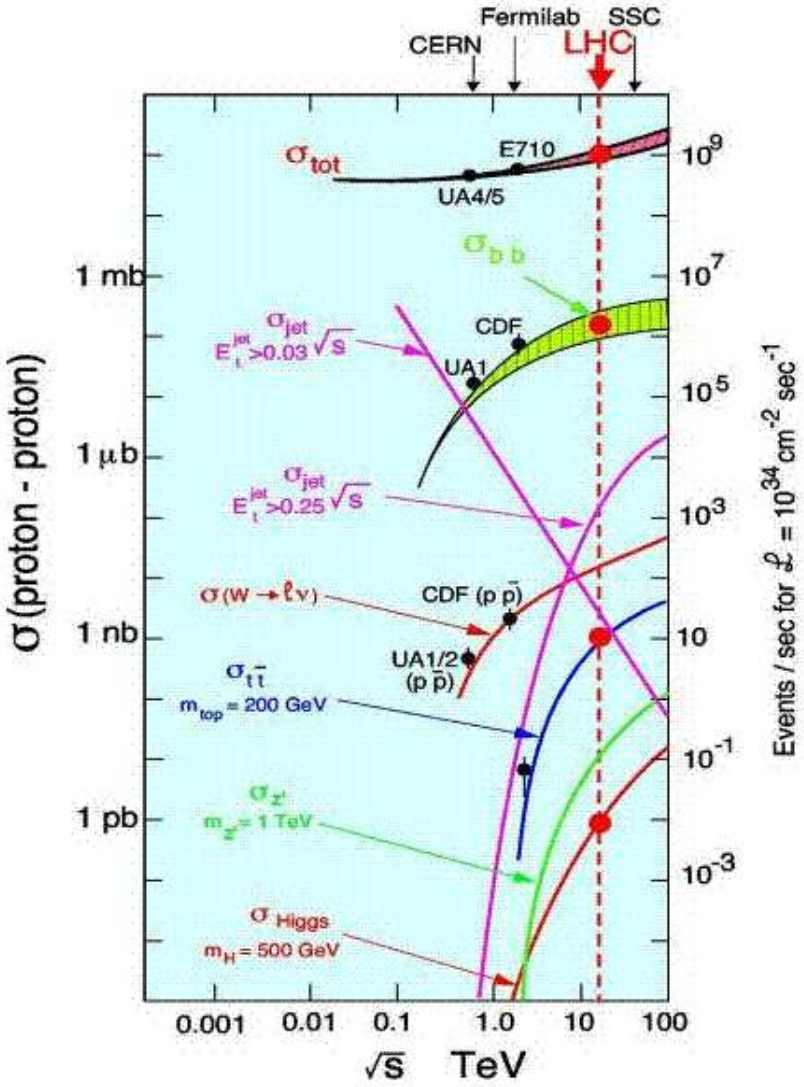

Figure 1.1: Evolution *w.r.t.* $\sqrt{s}$ of cross-sections for pp and sub-processes.

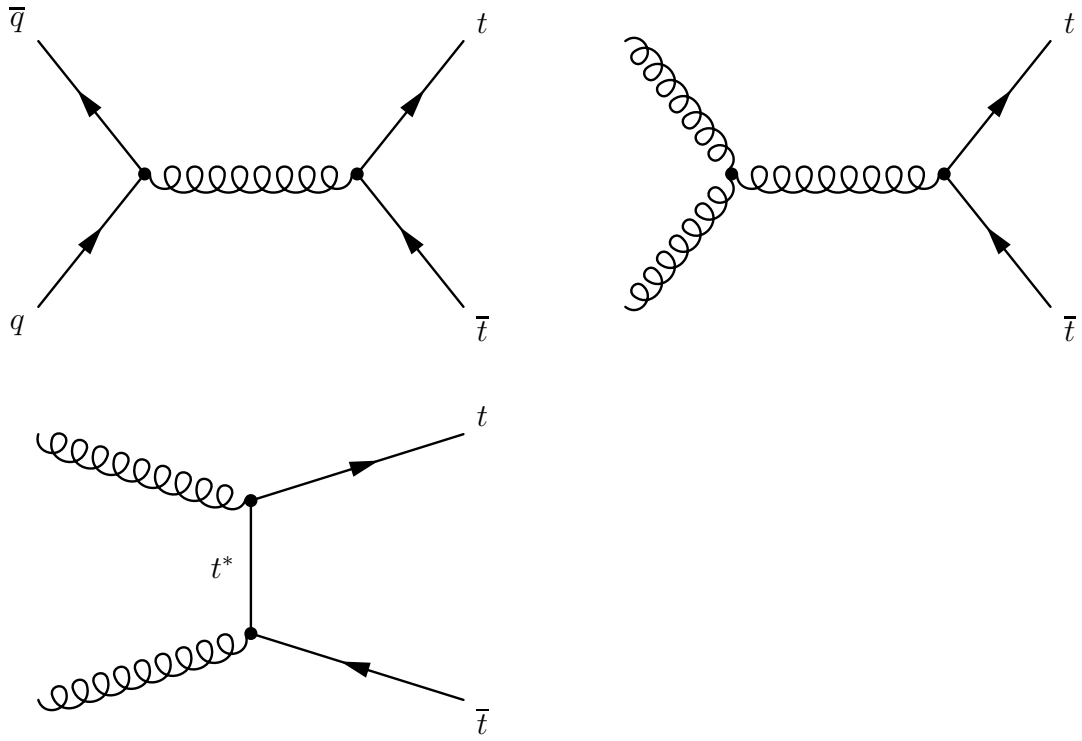

Figure 1.2: $t\bar{t}$ pair production channels at tree level.

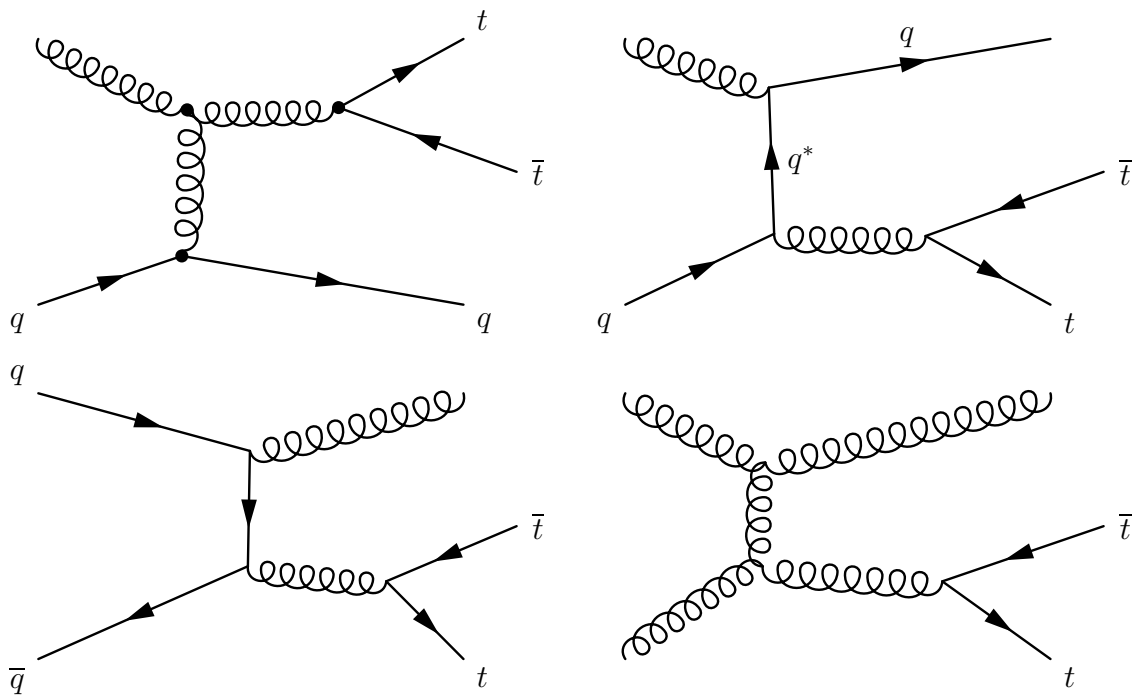

Figure 1.3: Examples of $t\bar{t}$ pair production channels at NLO.

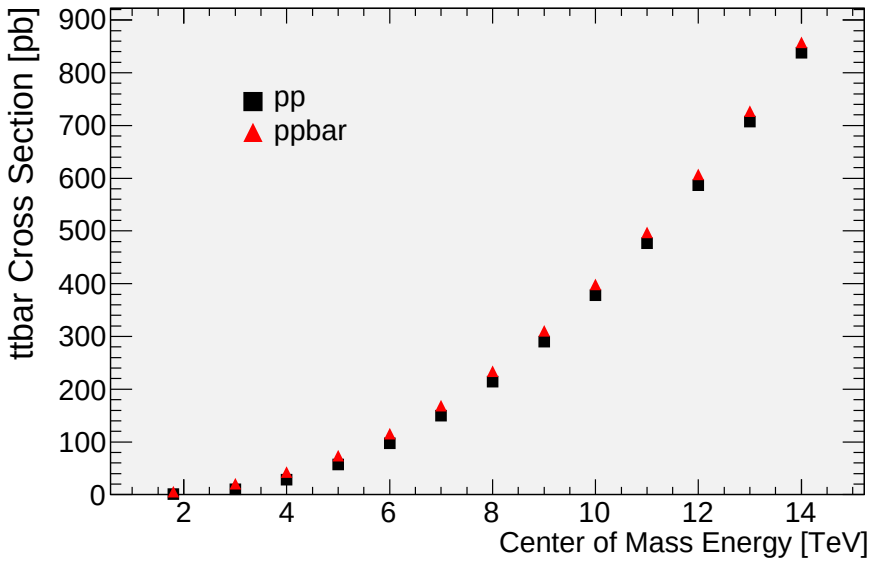

Figure 1.4: $t\bar{t}$ cross-section @ NLO evolution with increasing $\sqrt{s}$

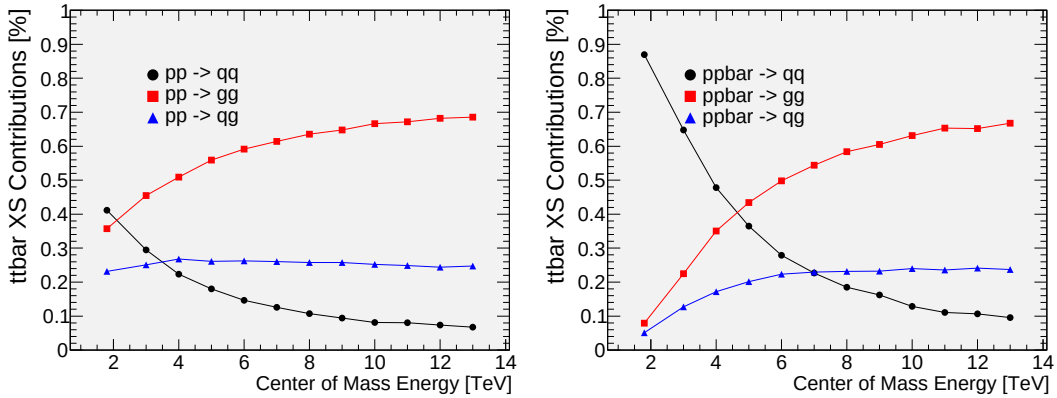

Figure 1.5: $t\bar{t}$ cross-section @ NLO: Relative contributions of production channels.

1.1.3 Top Quark Decay Channels

Top quark couples almost 100% of the times with a W boson and a b quark in a $t \rightarrow Wb$ vertex. This can be explained theoretically from the Cabibbo-Kobayashi-Maskawa (CKM) matrix:

$$\begin{pmatrix} |V_{ud}| & |V_{us}| & |V_{ub}| \\ |V_{cd}| & |V_{cs}| & |V_{cb}| \\ |V_{td}| & |V_{ts}| & |V_{tb}| \end{pmatrix} \sim \begin{pmatrix} 0.974 & 0.226 & 0.004 \\ 0.226 & 0.973 & 0.041 \\ 0.009 & 0.041 & 0.999 \end{pmatrix} \tag{1.5}$$

This matrix encodes the strength of the flavour-changing weak interaction between quarks of different flavours. In our case, $|V_{tb}| >> |V_{td}|, |V_{ts}|$ so we can say that for every practical purposes, top quarks interacts weakly only in tWb vertices (see figure 1.6). The decay width can be explicitly calculated [48], neglecting the b quark mass:

$$\Gamma_t = \frac{G_F m_t^3}{8\pi\sqrt{2}} \left(1 - \frac{m_W^2}{m_t^2}\right)^2 \left(1 + 2\frac{m_W^2}{m_t^2}\right) \left[1 - \frac{2\alpha_s}{3\pi}\left(\frac{2\pi^2}{3} - \frac{5}{2}\right)\right] \tag{1.6}$$

where G_F is the Fermi coupling constant, m_W is the mass of the W boson and m_t is the mass of the top quark. For a top mass $\sim 170\, GeV$, the decay width of this vertex yields $\Gamma = \alpha_W m_t = 1.7\ GeV/c^2$, meaning that the top quark is highly unstable, with a corresponding lifetime of $\tau = \Gamma^{-1} = 4 \times 10^{-25} s$. According to relativity, a hadron of typical radius $\sim 1 fm$ cannot form in less than $10^{-22} s$, so this explains why a meson containing a top quark has never been found. On the other hand, thanks to the high value of its mass, the t is the only quark that can be observed "bare". In fact, its decay width is much larger than the QCD scale $\Lambda_{QCD} = 217^{+25}_{-23}\, MeV$, so the top quark decays before hadronization and thus forms no bound states. It is worth to remember that the very definition of the mass of a heavy quark is not uniquely defined: in fact, at higher orders the propagator behaves like $\sim (\not{p} - m_0 - \Sigma)^{-1}$, where m_0 is the "bare" mass. Two schemes of renormalization are used: $\bar{M}S$ and **on-shell**. The "pole" mass M, *i.e.* the real part of the pole of the propagator, is more physical but is affected by long- distance effects: it can never be determined with accuracy better than the QCD scale Λ_{QCD}. The $\bar{M}S$ mass $\bar{m}(\mu)$ is a fully perturbative object, not sensitive to long-distance dynamics. It can be determined

as precisely as the perturbative calculation allows. The two masses are related by the perturbative relation:

$$\begin{aligned}\frac{M}{\bar{m}(\mu=\bar{m})} &= 1+\frac{4}{3}\left(\frac{\bar{\alpha}_S}{\pi}\right)+\left(\frac{\bar{\alpha}_S}{\pi}\right)^2(-1.0414N_L+13.4434)\\ &\quad+\left(\frac{\bar{\alpha}_S}{\pi}\right)^3\left(0.6527N_L^2-26.655N_L+190.595\right)+O(\Lambda_{QCD}(1.7)\end{aligned}$$

However, in experiments only invariant masses are actually measured. How to link this mass to bare mass or pole mass is beyond the scope of this work.

Figure 1.6: Top quark weak interaction. tWb vertex is dominant *w.r.t.* tWd and tWs.

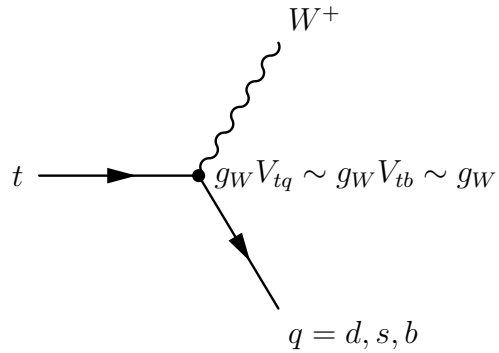

After the weak interaction, b quark evolves directly into a particle jet, while the W boson decays into a pair of leptons ($l^{\pm}, \nu_l$) or a pair of quarks (q, q') which in turn produces two particle jets. Given the universality of the weak interaction, the resulting branching fractions can be easily evaluated and are shown in table 1.4. In the case of $t\bar{t}$ production, there are two W bosons, so the possible combined final states are reported in table 1.5. A pictorial representation of decay channels and branching fractions is shown in figure 1.8.

Table 1.4: W boson decay branching fractions.

$W^{\pm} \rightarrow$	$e^{\pm}\nu_e$	fraction = $1/9$
	$\mu^{\pm}\nu_{\mu}$	fraction = $1/9$
	$\tau^{\pm}\nu_{\tau}$	fraction = $1/9$
	$l^{\pm}\nu_l$	fraction = $3 \times 1/9 = 1/3$
	$q\overline{q}'$	fraction = $4 \times 1/9 = 2/3$

Table 1.5: $t\bar{t}$ decay branching fractions.

$t\bar{t} \rightarrow W^+b + W^-\bar{b} \rightarrow$	$l^+\nu_l b + l^-\overline{\nu}_l\bar{b}$	fraction = $1/3 \times 1/3 = 1/9$	(full-leptonic)
	$l^+\nu_l b + q\overline{q}'\bar{b}$	fraction = $1/3 \times 2/3 = 2/9$	(semi-leptonic)
	$q\overline{q}'b + l^-\overline{\nu}_l\bar{b}$	fraction = $2/3 \times 1/3 = 2/9$	(semi-leptonic)
	$q\overline{q}'b + q\overline{q}'\bar{b}$	fraction = $2/3 \times 2/3 = 4/9$	(full-hadronic)

Figure 1.7: Top quark decay chain.

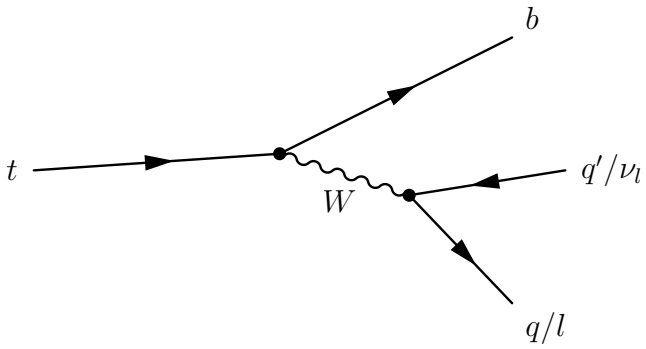

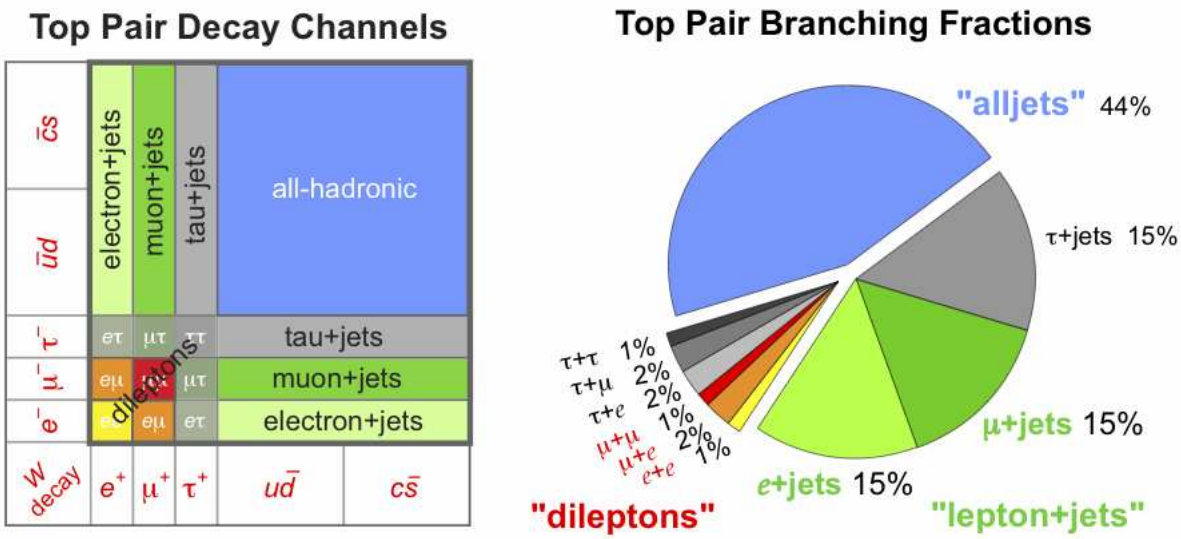

Figure 1.8: Top pair decay channels (left) and branching rations (right).

1.1.4 Top pairs signal

Events containing a $t\bar{t}$ pair are classified according to the decays of the W bosons: *full-hadronic* if both Ws decay into quarks, *di-leptonic* if both Ws decay into leptons and *semi-leptonic* if one W decays into leptons and the other one into quarks. The picture is actually complicated by the fact that the τ lepton decays hadronically $\sim 64\%$ of the times. Since the tagging of τ-jets is more difficult than the identification of electrons and muons, at least at the beginning of data taking attention will be paid mostly towards $t\bar{t}$ decays with electrons and/or muons in the final state. In addition, in hadronic colliders such as the LHC most of the events present only particle jets originated from QCD interactions, and these events constitute a background to high-p_T physics searches such as $t\bar{t}$ decays. For instance, from the expected production cross-section on average one $t\bar{t}$ event will be produced every 10^9 QCD multijet events. For this reason, identification of $t\bar{t}$ full-hadronic events against QCD multijet background seems an extremely difficult task compared to channels containing one or two charged isolated leptons. This channels share another useful feature for background rejection, *i.e.* the presence of neutrinos in the final state. Neutrinos escape from the detector, leaving an unbalance in the sum of the p_T of the observed particles, the so-called *missing transverse energy* (E_T^{miss}). As will be shown in the next chapter, QCD multijet events have no or very few real E_T^{miss} , so this quantity is very effective for the rejection of this kind of background. Besides this, in $t\bar{t}$ di-leptonic events the presence of two neutrinos coming from the two separate W decays makes the determination of m_t more challenging than in the semi-leptonic case. Furthermore, di-leptonic events account only for $1/9$ of the $t\bar{t}$ production cross-section. Eventually, one concludes that the simplest and most-promising channel, at least in early LHC running, for the study of top quark pairs is actually the semi-leptonic channel in which the leptonic W decays into an electron or a muon. A summary of the three top quark decay channels is shown in table 1.1.4.

1.1.5 Backgrounds to Top-antitop Decays

Given the high mass of the top quarks, their decay products are often emitted at high momentum and large angles with respect to the initial beam direction.

Channel	Topology	Backgrounds
Semi-leptonic	2 jets + 2 b-jets, 1 isolated lepton, E_T^{miss}	W+jets
Di-leptonic	2 b-jets, 2 isolated leptons, E_T^{miss}	di-boson WW+jets, Z+jets
Full-hadronic	4 jets + 2 b-jets, no isolated leptons, no E_T^{miss}	QCD multijet

Table 1.6: Summary of top decay channels and their principal backgrounds.

On the contrary, hadrons produced in pp or $p\overline{p}$ collisions have usually high momenta but small angles *w.r.t.* the beam direction [44]. Thus, most of the background events could be discarded if a preselection is applied requiring in the final state:

$$l^{\pm} + \nu_l(E_T^{miss}) + Njets \tag{1.8}$$

This will be discussed extensively throughout the rest of this work.

1.1.5.1 QCD Multi-jet

In hadronic colliders, the most common events are QCD di-jet, with a cross-section in the order of $10^9 pb$ at the LHC. Sub-leading QCD processes, called multi-jet events, present three or more particle jets originated by radiated gluons or $q\overline{q}$ pairs. Since no electroweak processes are included in the hard-scattering (as happens in di-bosons events, for example), theoretically this kind of events provides no or only a small amount of missing transverse energy. Thus, such events acts as a background differently for $t\bar{t}$ events, according to the classification of the decay of the two top quarks:

Semi-leptonic channel Mis-measurement of missing transverse energy in combination with the appearance of a fake high-p_T lepton are quite uncommon, but given the extremely high rate of QCD Multi-jet background, a certain number of events can pass the selection criteria. Event selection involving the reconstruction of electrons are typically prone to this kind of mis-identification, but tight requests on electron isolation and track matching can tame this problem effectively.

Di-leptonic channel QCD MJB can mimic a $t\bar{t}$ di-leptonic decay in the very rare case of an event with mis-measured missing E_T and *two* fake high-p_T leptons.

Full-hadronic channel This channel presents at least 6 jets (2 b-jets and 2 jets coming from each W bosons). Rejection of QCD MJB is much more complicated than in the leptonic case, however b-tagging and some more advanced techniques can improve selection efficiency.

Examples of QCD multi-jet backgrounds are shown in figure 1.9

Figure 1.9: QCD Multi-jet events.

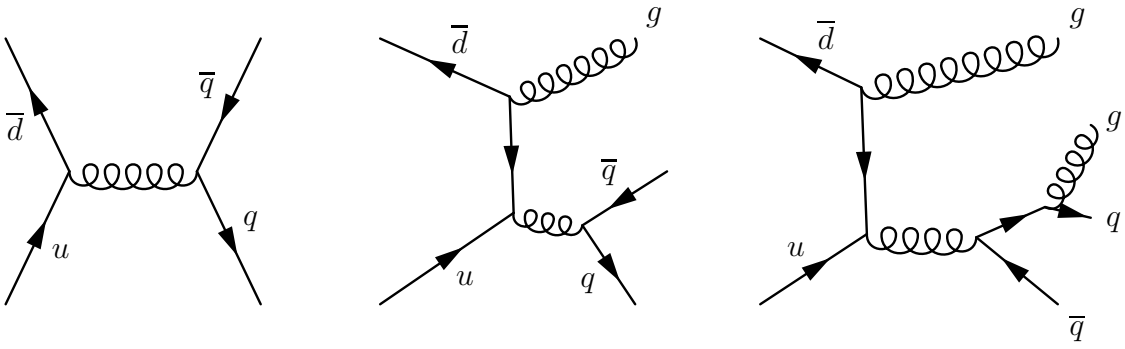

1.1.5.2 W+jets and Z+jets

QCD multijet background is not at all the only background that is present in such collisions. In fact, charged isolated leptons can arise from *Drell-Yan* production, *e.g.* $q\overline{q} \rightarrow Z \rightarrow l^+l^-$, or from the decay of a W boson, and both can be produced in association with particle jets originated from a radiated quark or gluon. Furthermore, real E_T^{miss} is present in $W \rightarrow l^{\pm}\nu_l$ decays due to neutrinos. Some examples are given in figure 1.10. Of course, detector effects such as dead materials, misreconstruction of leptons and jets and miscalibration must be considered, since they can give rise *i.e.* to fake missing transverse energy and fake leptons reconstructed from jets. All these effects will be studied in depth in the following chapters. All in all, $W + jets$ events will be the most important Standard Model background to $t\overline{t}$ studies at the LHC.

1.1.5.3 Single top

Top quarks can even be produced individually through weak interactions. These *single-top* production processes are usually divided into three classes, depending on the virtuality of the W boson involved at the leading order [11]:

Figure 1.10: Examples of W+jets (left) and Z+jets (right) events.

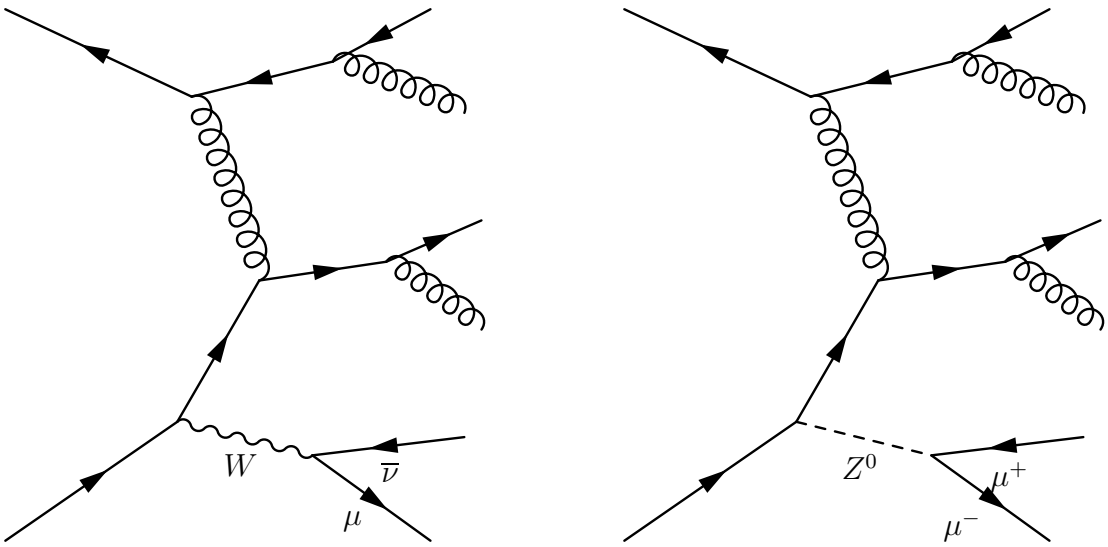

- Quark-antiquark annihilation (*s-channel*) such as $u + \overline{d} \rightarrow t + \overline{b}$
- W boson exchange (*t-channel*) such as $u + b \rightarrow t + d$
- Wt associated production such as $b + g \rightarrow W + t$

At the LHC, the most important production channel will be *t-channel* [8] with a cross section of $124pb$ at $\sqrt{s} = 10TeV$, followed by Wt ($32pb$) and *s-channel* ($6pb$). Single top productions will provide a measurement to the V_{tb} element of the CKM matrix, and could unravel the existence of a fourth generation of fermions and of a W' boson.

1.1.5.4 Diboson

Diboson processes are interactions in which two boson are produced and decay subsequently, the most important being WW, WZ and ZZ. This is considered a minor background since the requirement of at least two b-tagged jets reduces its contamination considerably. However, b-tagging will not be used in the analysis presented here as it is not clear if the efficiency of the tracker will be high enough at the beginning of the operations. Events of type $WbWb$ (two radiated b quarks) could survive event selection (see figure 1.12).

Figure 1.11: Single top production channels at LO: *s-channel*, *t-channel* and *Wt* associated production

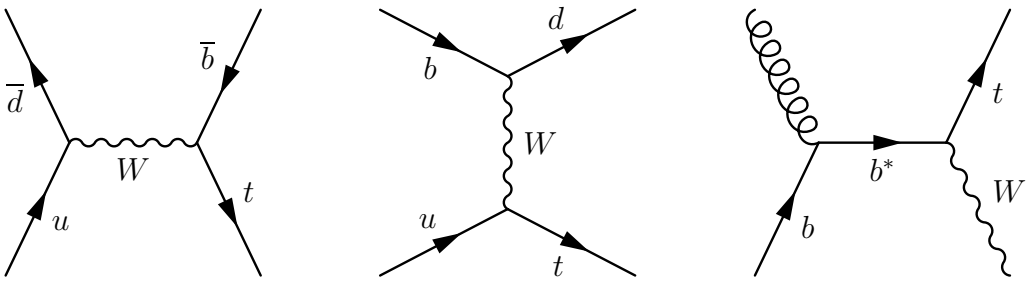

Figure 1.12: Diboson event $WbWb$.

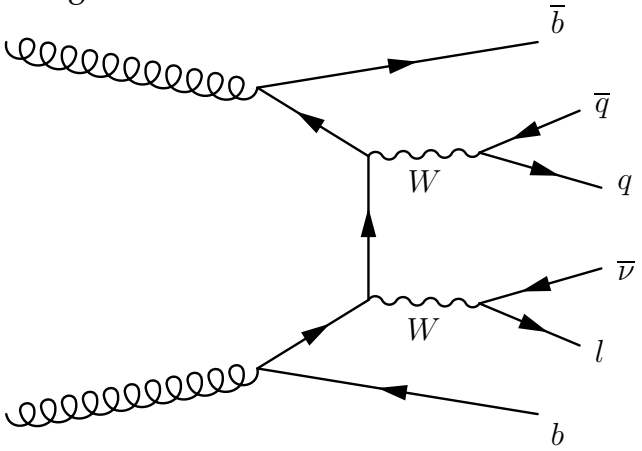

1.2 Monte Carlo Generators

1.2.1 Generation at LO and NLO

The simulation of an arbitrarily complex event is usually factorized in several steps, *i.e.* :

Hard Process This can be seen as the core of the interaction, usually the theoretically best understood and experimentally most interesting part. Tipically, fixed-order perturbative *matrix elements* are used. *Leading-order* calculations can be largely automated since the squared m.e. are positive definite. At present, the most commonly used programs [10] that can perform these kind of calculations are Madgraph/Madevent [12], COMPHEP [28], AMEGIC++ (Sherpa) [39], AlpGen [43]. *Next-to-Leading-order* calculations are more difficult to automate since real and virtual contributions have equal and opposite divergences, and generators need to know beforehand how to carry on to the hadronization level. Programs that can do NLO generation are at present, for instance, MC@NLO [36], POWHEG [35], MCFM [2], NLOJET++ [23].

Parton Shower As accelerated QED charges emit photons, so accelerated QCD charges radiate colour charges. Thus, cascades of partons are expected, and they are usually referred to as *parton showers*. An example of parton shower is shown in Fig. 1.13.

Figure 1.13: Example of Parton Shower mechanism

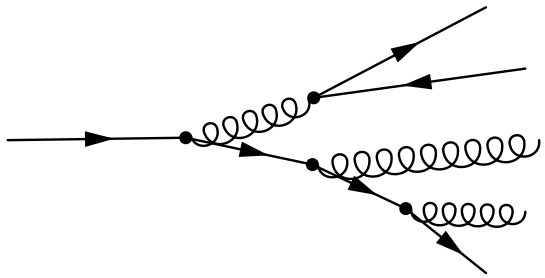

For instance, a 3-jets cross section can be written in terms of quark-gluon

opening angle θ and the *light-cone momentum fraction* [2] z as follow:

$$d\sigma = \sigma_0 \sum_{jets} C_F \frac{\alpha_S}{2\pi} \frac{d\theta}{\theta} dz \frac{1+(1-z)^2}{z} \tag{1.9}$$

This expression becomes singular as $z \to 0$ or $\theta \to 0$ and holds for every quantity that behaves like θ^2, usually:

- transverse momentum $k_\perp^2 = z^2(1-z)^2\theta^2 E^2$
- invariant mass $q^2 = z(1-z)\theta^2 E^2$

This property leads to a generalization know as *Universal Collinear Limit*:

$$d\sigma = \sigma_0 C_F \frac{\alpha_S}{2\pi} \frac{d\theta^2}{\theta^2} P_i(z,s) ds \tag{1.10}$$

Where $P_i(z,s)$ is known as *Altarelli-Parisi splitting kernel* and is a function depending on the kind of branching i and spin s. Examples of splitting kernels are given in Tab.1.7.

Table 1.7: Altarelli-Parisi splitting kernels for common Standard Model branchings.

$$\begin{aligned}
P_{q\to qg} &= \frac{C_F}{1-z}\left[1+z^2-\frac{2m_q^2}{2q^2}\right] \\
P_{g\to gg} &= C_A\left[\frac{z}{1-z}+\frac{1-z}{z}+z(1-z)\right] \\
P_{g\to q\bar{q}} &= T_R\left[1-2z(1-z)+\frac{2m_q^2}{z(1-z)q^2}\right]
\end{aligned}$$

In order to resolve two partons, a separation criteria must be introduced, *e.g.* $k_\perp^2 > Q_0^2$. The *A.P.* splitting kernel is in turn used to define the probability that an emission occours at an energy scale between q^2 and $q^2 + dq^2$

$$d\mathcal{P} = \frac{\alpha_S}{2\pi}\frac{dq^2}{q^2}\int_{Q_0^2/q^2}^{1-Q_0^2/q^2} dz P(z) \equiv \frac{dq^2}{q^2}\bar{P}(z) \tag{1.11}$$

[2] Given a branching $A \to b + c$, variable z parameterizes how the momentum component of the parent parton A is divided between its two daughter partons: $z_i \equiv \frac{p_i}{p_A}$

In analogy to radioactive decay, one can calculate the non-emission probability between a higher and a lower energy scales Q^2 and q^2, so that:

$$\frac{d\Delta(Q^2,q^2)}{dq^2} = \Delta(Q^2,q^2)\frac{d\mathcal{P}}{dq^2} \tag{1.12}$$

$$\Delta(Q^2,q^2) = \exp\left(-\int_{q^2}^{Q^2}\frac{dk^2}{k^2}\bar{P}(k^2)\right) \tag{1.13}$$

$$\Delta(Q^2,Q_0^2) \equiv \Delta(Q^2) \sim \exp\left(-C_F\frac{\alpha_S}{2\pi}\log^2\frac{Q^2}{Q_0^2}\right) \tag{1.14}$$

Equation (1.14) defines the *Sudakov form factor*, representing the probability that the emitted radiation is non-resolvable, *i.e.* it is impossibile to distinguish the two partons (Fig. 1.14). In order to preserve unitarity:

$$P(resolved) + (P(unresolved) + P(virtual)) = 1 \tag{1.15}$$

At this point one can choose a starting scale Q^2, and generate branchings according to:

$$d\mathcal{P} = \frac{dq^2}{q^2}\bar{P}(q^2)\Delta(Q^2,q^2) \tag{1.16}$$

Choosing a random number $0 < \rho < 1$ uniformly, if $\rho < \Delta(Q^2,q^2)$ the evolution stops, otherwise one solves the equation $\rho = \Delta(Q^2,q^2)$ for q^2 as the emission scale of the next branching.

Actually, it is also possible to use θ^2 or $k_\perp^2$ as evolution parameter, but even if all of these quantities are formally on equal footing, differences in calculation time can be important. The angular separation θ^2 is often employed to manage *soft gluons* that are emitted at large angles *w.r.t.* hard partons. In principle, soft gluons can interact with particle in the showers. However, it can be demonstrated that the intensity of radiation is proportional to the coherent sum of emissions from the emitting parton (the jet parent). While angular ordering produces wide-angle soft emission first, this is not obvious with other evolution-driving variables. This problem is particularly well-treated with the POWHEG method (see section 1.4).

Hadronization Given the enormous complexity of this step and the lack of a

Figure 1.14: Resolvable (left), unresolvable (center) and virtual (right) emissions

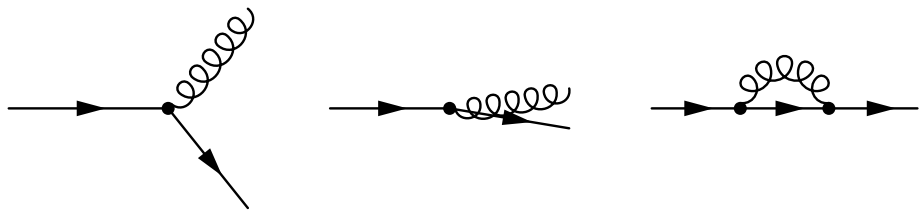

theory for a correct treatment of non-perturbative QCD, only phenomenological models are actually used. Historically, one of the fist proposed model was the **Independent Fragmentation Model** (also known as "Feynman-Field" model). Experimentally, in $e^+e^- \rightarrow q\bar{q}$ events the number of hadrons produced is flat in rapidity and shows a limited distribution in transverse momentum like $\rho(p_T^2) \sim \exp(-p_T^2/2p_0^2)$. With this model, one can estimate jet energy and momentum:

$$E = \int_0^{\eta_M} dy d^2p_T \rho(p_T^2) p_T \cosh y = \lambda \sinh \eta_M \quad (1.17)$$

$$P = \int_0^{\eta_M} dy d^2p_T \rho(p_T^2) p_T \sinh y = \lambda \left(\cosh \eta_M - 1\right) \sim E - \lambda \quad (1.18)$$

$$\lambda = \int d^2p_T \rho(p_T^2) p_T \sim 1/R_{had} \sim m_{had} \quad (1.19)$$

Unfortunately, this model is unsatisfactory since there is no obvious relation with perturbative emission, is not infrared safe and it doesn't include confinement.

A more advanced model is the **Lund string model** [54]. At present, this model is implemented in two important generators, Pythia and Sherpa. From the experiments, at long distances, interquark potential gluon self-interaction makes field lines attract each other, resulting in an effective potential which is linear at first order approximation:

$$V(R) = V_0 + \kappa R - e/R + f/R^2 \quad (1.20)$$

with $\kappa \sim 1\ GeV/fm$. The mass of a meson is thus $m^2 = 2\kappa^2$ and $q\bar{q}$ pairs are created by tunneling with a probability $\sim \exp(-b(m_q^2 + p_T^2))$. One can

Figure 1.15: Cluster model: gluons are represented by colour-anticolour lines.

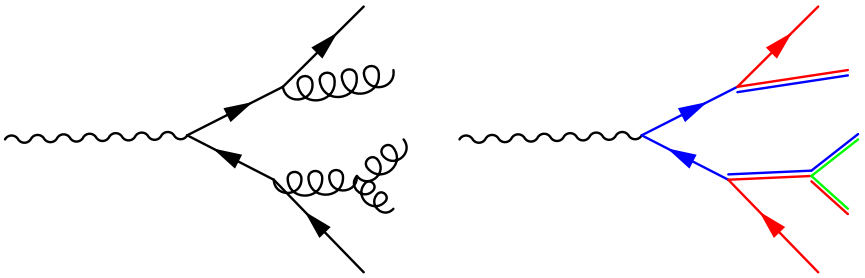

adjust parameters for each quark flavour and meson from experiments. As for the baryons, one considers two quarks tightly bounded, so that a "diquark" state is treated just like an antiquark.

Another successful hadronization model is the **Cluster Model**, which makes use of colour charge flow. This model has been successfully implemented in HERWIG. The mass spectrum of colour-singlet pairs is asymptotically independent of energy and production mechanism, peaked at a low mass Q_0. Clusters represent mesonic resonances that decay to lighter resonances and stable hadrons. In this model, heavy hadron production is suppressed.

After the perturbative parton showering, all outgoing gluons are split non-pertubatively into quark-antiquark pairs so that only quarks can effectively give rise to particle jets. Each final state colour line links a quark to an anti-quark, *i.e.* a *colour singlet cluster*. At this point, clusters fragment into lighter hadrons. If a cluster is too light to decay into two hadrons, it is taken as a representation of that hadron. A fraction of clusters have masses too high so that this mechanism is not directly applicable. Instead, an interative fission model is used until the mass of the daughter clusters is low enough. In HERWIG, for instance, three main parameters determine the threshold over which a cluster is split, according to the formula [1]:

$$M_f^{CLPOW} = CLMAX^{CLPOW} + (m_{q1} + m_{q2})^{CLPOW} \tag{1.21}$$

where m_{q1} and m_{q2} are the quark nominal masses. Usually, only a small

fraction of clusters undergoes fission, so only the tail of the cluster mass spectrum is actually affected from changing these parameters. Unfortunately, the production rates of high p_T of heavy particles depends strongly on the tail of the mass spectrum. For examples, a low value of $CLPOW$ increases the yield of heavy clusters. However, the b-quark hadronization is still not satisfactory so that another parameter ($B1LIM > 0$) is introduced to allow clusters with mass above $M_{B\pi}$ to form a single B-meson if $M_f < (1 + B1LIM)M_{B\pi}$. As result, the probability of single-meson clustering decreases linearly for $M_{B\pi} < M_f < (1 + B1LIM)M_{B\pi}$ and the B-spectrum is hardened. The tuning can also be applied specifying two different sets of $(CLPOW, CLMAX)$, one for light quarks and one for b-quarks.

Decay String and clusters decay mainly to unstable resonances, which in turn decay further according to PDG data tables. Unfortunately, so far not all the resonances have been measured, and even when it has been done, branching fractions do not add up to 100% everywhere. This uncertainty is reflected in tunable parameters in these models, which are "updated" as soon as new data appear.

Multiple Interaction and beam remnants Since protons are extended objects, a hard scattering leaves two colour-charged objects (the *remnants*) which in turn interact between each others. It is possible to describe this interaction with a perturbative or a non-perturbative model. Experimentally it has been measured that for high $\sqrt{s}$ and small p_T, inclusive parton-parton cross section is larger than the total proton-proton cross section. Thus, more than one parton-parton interaction occurs per event. Using the perturbation theory, n-scatter distributions can be calculated once that the spatial distribution of partons (*i.e.* the *PDF*) is known.

1.3 Comparison among generators

1.3.1 Objects definition

Comparisons have been performed using Rivet [19], a tool that belongs to the CEDAR project [18], developed and maintained by MCnet [5]. This tool provides a generator-independent framework for comparison of event generator predictions, useful, in particular, for generator validation and tuning. Rivets makes use of the FastJet plugin [37] to cluster final state particles into particle jets. Before any deeper analysis, three different jet algorithms have been tested with four possible values of the aperture parameter, in order to determine the most suited jet algorithm. In the following, *good jets* are defined as jets with $pT > 20\ GeV$ and $|\eta| < 2.5$ and events with at least 4 jets are tagged with a $4j20$ label. The analysis has been run on a $QCD\ 2 \rightarrow 2$ partons sample of 20k events generated at $10\ TeV$ with HERWIG/Jimmy 6.510. Details will be given in section 1.3.4.

1.3.2 Particle Jets

A high-quality and efficient jet reconstruction is an important tool for a large number of analyses to be performed with the ATLAS detector. A systematic uncertainty of 1% [24] is desirable for the reconstruction of invariant masses of heavy quarks, gauge boson and possibly yet undiscovered particles. At present there is not a single recipe to choose the ”best” jet reconstruction algorithm, but some tightening guidelines can be suggested:

Infrared safety The presence of additional soft particles should not affect the overall jet reconstruction;

Collinear safety A jet should be reconstructed independently of the fact that a certain amount of transverse energy is carried by a single particle, or if this particles is split into two collinear particles;

Order independence The same hard-scattering should be reconstructed at parton, particle and detector level;

Detector independence Reconstruction should be affected as less as possible from resolution, provided that signals from the detector are stable;

Environment independence Additional activities such as multiple interactions, pile-up, underlying event and sudden change of instantaneous luminosity should not prevent the reconstruction of a jet. In particular, jets from hard-scattering partons should be found with a very high efficiency;

Implementation Jet finder algorithms should be as fast as possible, avoiding the use of excessive computational resources.

The benchmark algorithm is *iterative seeded fixed-cone*, but higher efficiency and stability can be reached using other and more elaborate jet finders:

Iterative seeded fixed-cone (Cone) All input objects are ordered in decreasingly transverse momentum. If the leading object has a p_T greater than a threshold set to $1\ GeV/c$, all objects within a cone in (η, ϕ) space of radius

$$\Delta R = \sqrt{\Delta\eta^2 + \Delta\phi^2} \leq R_{cone} \tag{1.22}$$

are combined with the seed object. In Atlas, R_{cone} is commonly 0.4 (*narrow jets*) or 0.7 (*wide jets*). A new direction is calculated from the sum of four-momenta of objects inside and the cone axis is updated. This process is iteratively applied until the direction of the cone does not change anymore. The cone is considered stable and a jet has been found. The next seed is taken into account and a new cone is formed using the same iterative procedure. The jet finding algorithm is stopped when no seeds are available.

This algorithm is simple and fast, but not infrared safe. A split-merge procedure can be applied in order to partially get around this problem: Jets which share constituents with *more* than 50% of the p_T of the less energetic jet are *merged*, while they are *split* if the amount of shared transverse momentum is *less* than 50%.

From a theoretical point of view, cone jet finder is only meaningful to leading order for inclusive jet cross-section measurement and final states like $W/Z + 1$ jet, so its application is deprecated for final states with 3 objects like $W/Z + 2$ jets or a di-jet invariant mass + X.

There problems can be overcome with the aid of *SISCone* (Seedless Infrared Safe Cone) algorithm developed by Salam, Soyez et al. [37]. A

smart implementation based on geometrical considerations makes it relatively fast. The existing approach takes $N2^N$ time to find jets among N particles, making it unusable at hadron level. This can be reduced to $N \ln N$ time, leading to the *SISCone* code whose speed is similar to that of public so-called *midpoint* implementations. Monte Carlo tests provide a strong cross-check of an analytical proof of the IR safety of the new algorithm. This algorithm proved to be less sensitive to the Underlying Event. It is very likely that in the near future *SISCone* will be used as the standard cone algorithm in Atlas.

Sequential recombination (Clustering) All pairs of input objects are analysed with respect to their relative transverse momentum, using [20]:

$$d_{ij} = min(p_{T,i}^{2n}, p_{T,j}^{2n}) \frac{\Delta R_{ij}^2}{R^2} = min(p_{T,i}^{2n}, p_{T,j}^{2n}) \frac{\Delta\eta^2 + \Delta\phi^2}{R^2} \tag{1.23}$$

These jet finder take different names according to the value of the n exponent:

- $n = 0$ Cambridge
- $n = 1$ Kt
- $n = -1$ Anti Kt

The miminum d_{min} of all d_{ij} is found, and the objects i and j are removed from the list and replaced with a new object k whose four-momentum is the sum of two. If d_{min} is equal to a d_i, *i.e.* its distance *w.r.t.* the beam, this object is considered to be a jet and is removed from the list. The procedure is repeated until all objects are removed from the list. All original objects end up to be part of a jet (or are taken as a jet directly, *e.g.* if the reconstruction is performed at parton level in Monte Carlo simulations).

Contrary to the cone algorithm, this procedure is infrared and collinear safe: no final state objects remain unassigned, and the parameter R (the *only* free parameter) allows some control over the size of the jet. In Atlas, R parameter is usually set to 0.4 or 0.6. Given its accuracy, expecially important for studies at *next-to-leading* order, it is suggested to use *AntiKt* as the most appropriate clustering algorithm in LHC experiments such as Atlas.

Figure 1.16 shows a comparison of complexity among FastJet and other common algorithms such as MidPoint, JetClu and KtJet.

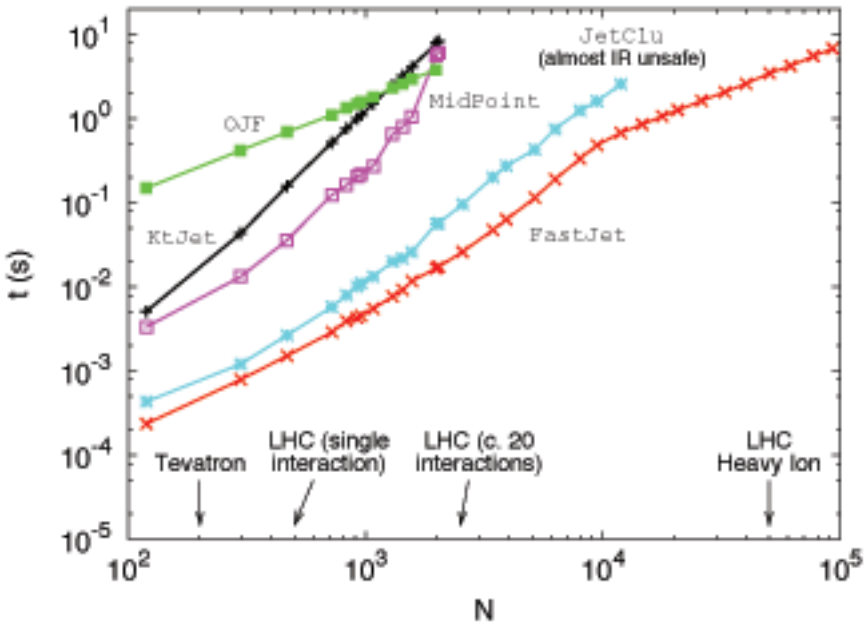

Figure 1.16: **Algorithm complexity for FastJet compared to other commonly used reconstruction algorithm.**

Observing the jet multiplicity plots for each aperture (0.4, 0.5, 0.6, 0.7) it is evident that the number of events with 0 reconstructed jets is highest for an aperture of $.4$ and reaches its minimum for $.7$. On the other hand, the number of events with 2 jets is highest for $.7$ jets. Since we are generating two-partons events, we conclude that an aperture of 0.7 is the most suited for this kind of study. Examining the p_T distribution for this aperture, one can find out that $AntiKt$ algorithm shows a behaviour halfway between SISCone (softest) and Kt (hardest). Thus, in conclusion, $AntiKt$ $.7$ jets will be used in the following to cluster particle jets. For an insight of the jet algorithm, see section 1.3.2.

1.3.3 Top Quark Events Generation

Commonly, Monte Carlo generators offer separate routines for the production of light quark (treated as they were massless) and heavy quark pairs. In fact,

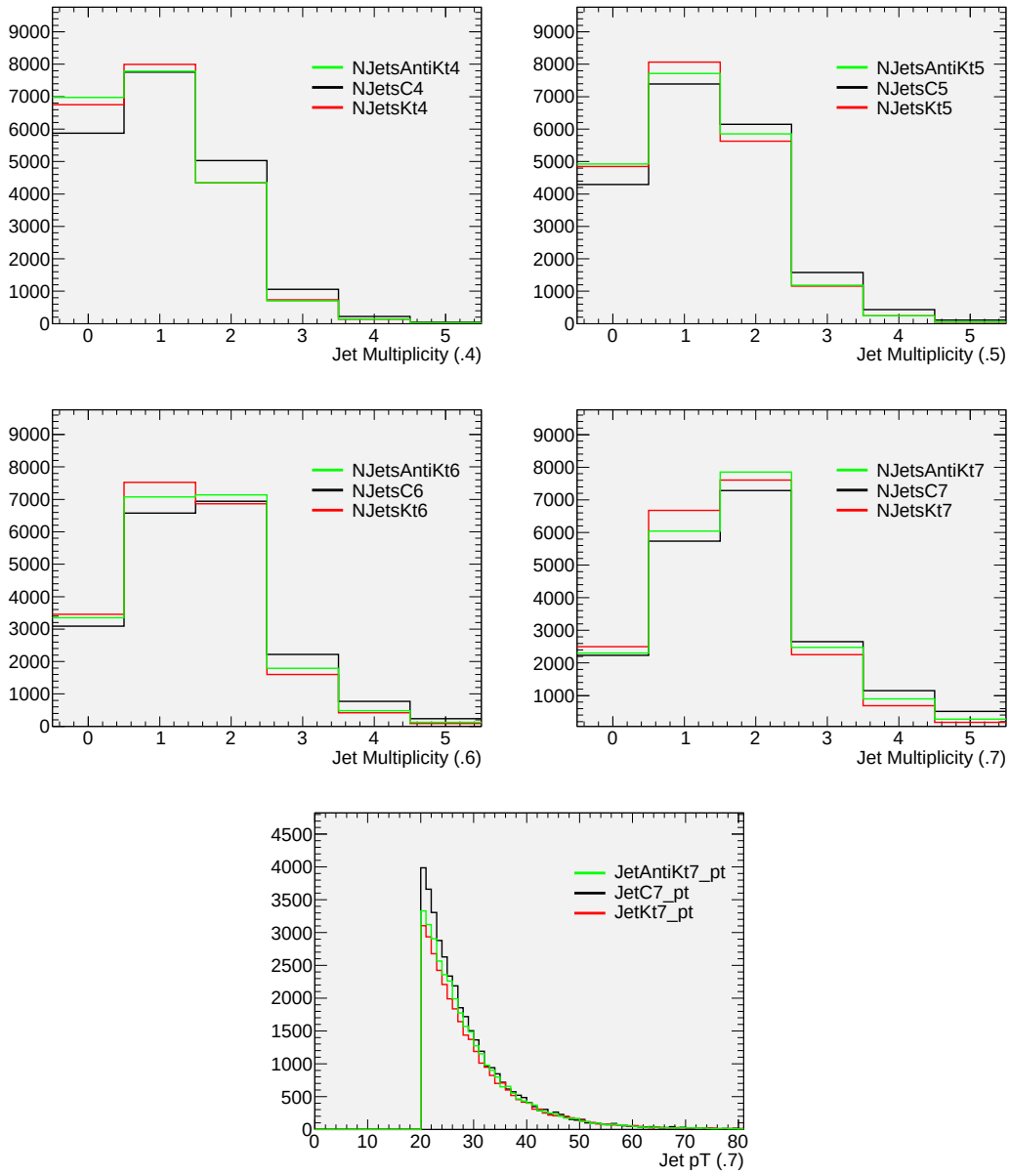

Figure 1.17: **Jet multiplicity for different jet apertures and p_T distribution for .7 jets.**

for light quarks the perturbative scale is determined by their k_T^2 only, while heavy quarks have in addition threshold effects due to their mass. As a consequence, the cross section are finite for $k_T \to 0$. Obviously, top quark pairs are effectively described with heavy quark production. In this study, the following generators have been used to produce $t\bar{t}$ samples:

- MC@NLO 3.3 (NLO) and HERWIG 6.510
- Powheg (NLO) and HERWIG++ 2.3.0
- Sherpa 1.1.3 (LO)
- Pythia 8 (LO)

As shown in Tab 1.8, events have been generated using particle properties taken from the Particle Data Book 2009. In particular, the top mass has been set to $171.2\ GeV$.

Table 1.8: $t\bar{t}$: generation parameters

m_t [GeV]	Γ_t [GeV]	m_W [GeV]	Γ_W [GeV]	m_b [GeV]	PDF
171.2	1.4	80.398	2.141	5.0	CTEQ 6l1

A number of kinematical and event shape variables have been studied:

- Particle jet multiplicity, pseudorapidity (η) and transverse momentum (p_T) distributions
- Leading jet p_T
- Transverse missing energy (E_T^{miss}), Effective mass (M_{eff}) and Transverse Energy Significance (E_T^{sig})
- Transverse sphericity (S_T)
- Aplanarity (A)
- Thrust, major and minor axis (Θ, Θ_{maj}, Θ_{min}) and Oblateness Ω
- Fox-Wolfram moments of order 1 and 2 (Φ_n)

Where the definition of M_{eff} and E_T^{sig} are:

$$M_{eff} \equiv E_T^{miss} + \sum_{j=0,1,2,3} p_T^{(j)} \equiv E_T^{miss} + H_T \tag{1.24}$$

$$E_T^{sig} \equiv \frac{E_T^{miss}}{\sqrt{\sum E_T}} \tag{1.25}$$

$$\sum E_T = \sum E_T(v.f.s.p.) \tag{1.26}$$

Where the sum in 1.26 is carried over visible final state particles (*v.f.s.p.*), *i.e.* charged particles, neutral hadrons but not neutrinos. Event shape variables such as Transverse sphericity S_T and Aplanarity A can be calculated from the sphericity matrix:

$$S^{\alpha\beta} = \frac{\sum_i p_i^\alpha p_i^\beta}{\sum_i |p_i|^2} \tag{1.27}$$

Where $\alpha, \beta = 1, 2, 3$ corresponds to the x, y and z components of each momentum vector p_i. Diagonalizing this matrix, one can obtain its eignevalues λ_1, λ_2 and λ_3 and thus define:

$$S_T = 2\frac{\lambda_2}{\lambda_1 + \lambda_2} \tag{1.28}$$

$$A = \frac{3}{2}\lambda_3 \tag{1.29}$$

Since the sphericity is quadratic in the particle momenta, it is not an infrared safe observable in perturbative QCD. This can be fixed by adding a regularizing power of r to the definition:

$$S^{\alpha\beta} = \frac{\sum_i |p_i|^{r-2} p_i^\alpha p_i^\beta}{\sum_i |p_i|^r}$$

The scalar quantity thrust is defined as:

$$\Theta = \max_{\vec{n}} \frac{\sum_i |\vec{p}_i \cdot \vec{n}|}{\sum_i |p_i|} \tag{1.30}$$

with the direction of the unit vector $\vec{n}$ which maximises T being identified as the thrust axis. The unit vector which maximises the thrust scalar in the

plane perpendicular to $\vec{n}$ is the *thrust major* direction, and the vector perpendicular to both the thrust and thrust major directions is the thrust minor. Both the major and minor directions have associated thrust scalars Θ_{max} and Θ_{min}. The difference between the two is called oblateness: $\Omega \equiv \Theta_{max} - \Theta_{min}$.

Fox-Wolfram moments are defined by:

$$\Phi_l = \sum_{i,j} \frac{|p_i||p_j|}{E_{vis}^2} P_l(\cos\theta_{ij}) \tag{1.31}$$

Where θ_{ij} is the opening angle between two hadrons i and j, E_{vis} is the total visible energy and $P_l(x)$ are the *Legendre* polynomials. If masses can be neglected, $\Phi_0 \equiv 1$. It is customary to normalize the results to Φ_0. If momentum is balanced, $\Phi_1 \equiv 0$. Di-jet events tends to have $\Phi_l \sim 1$ for l even and ~ 0 for l odd.

Events pass through a preselection, inspired by $t\bar{t}$ searches in the semileptonic channel with the Atlas detector [24]. Event shape variables are calculated for events with at least 4 good jets. As for the QCD case shown in the previous section, preselection efficiency varies with the definition of particle jet. For consistency, $AntiKt$ .7 algorithm has been used for jet reconstruction.

Events generated with Mc@NLO are used as benchmark, since this is a next-to-leading order generator, and has been tested against real data at Tevatron []. As can be seen in Fig. 1.18 and Fig. 1.19, all the generators considered here agree quite well among each other for the studied quantities. It can be seen that Sherpa produces on average less particle jets than Mc@NLO, while Pythia8 jets are harder and have on average a slightly higher multiplicity, reflecting this property in the M_{eff} distribution.

1.3.4 QCD Multijet Events Generation

The following LO generators have been used to produce separate samples of QCD multijet background, using the same set of parameters of $t\bar{t}$:

- Pythia 6.20
- HERWIG 6.510

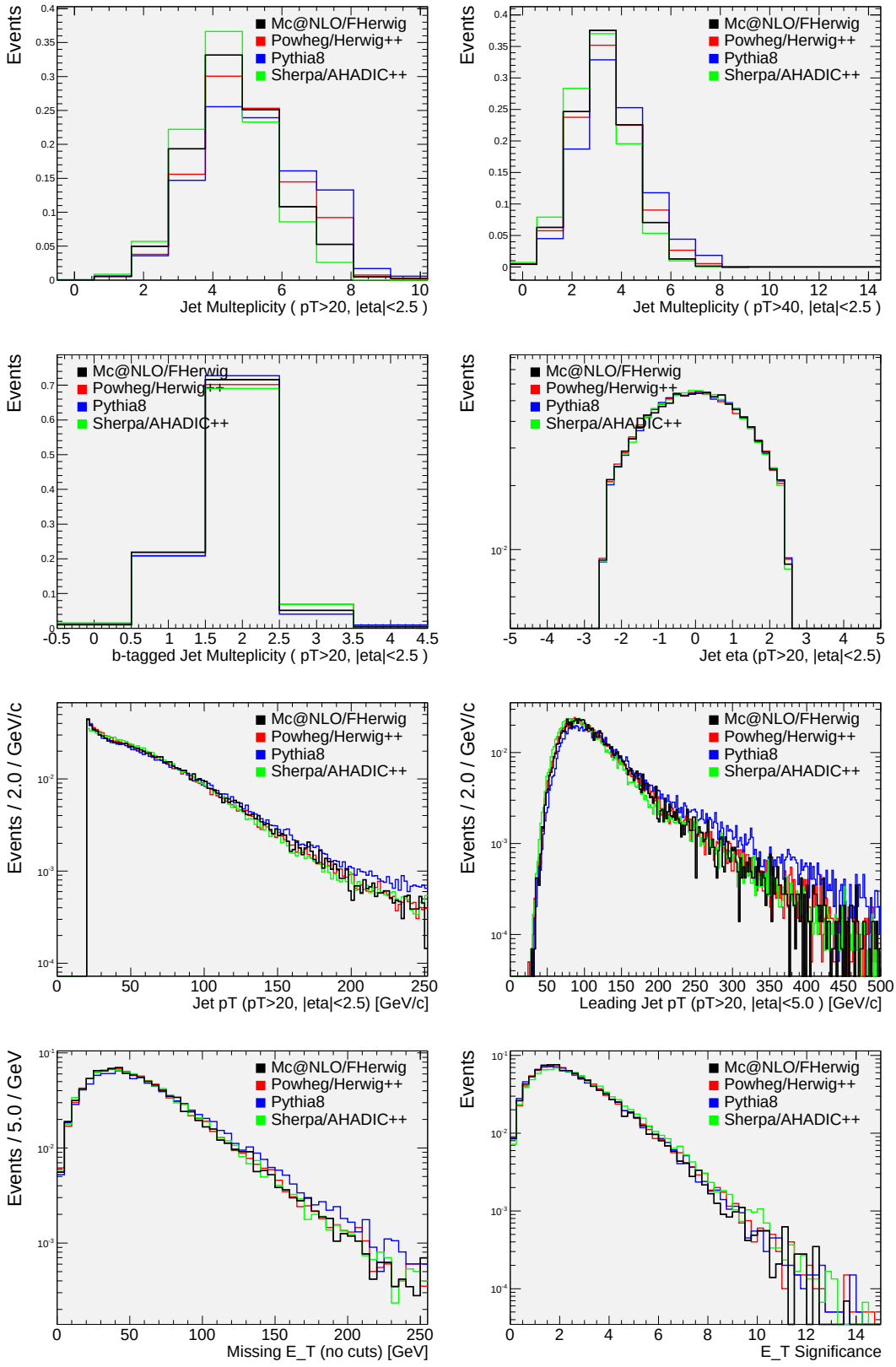

Figure 1.18: $t\bar{t}$ **: Kinematical variables**

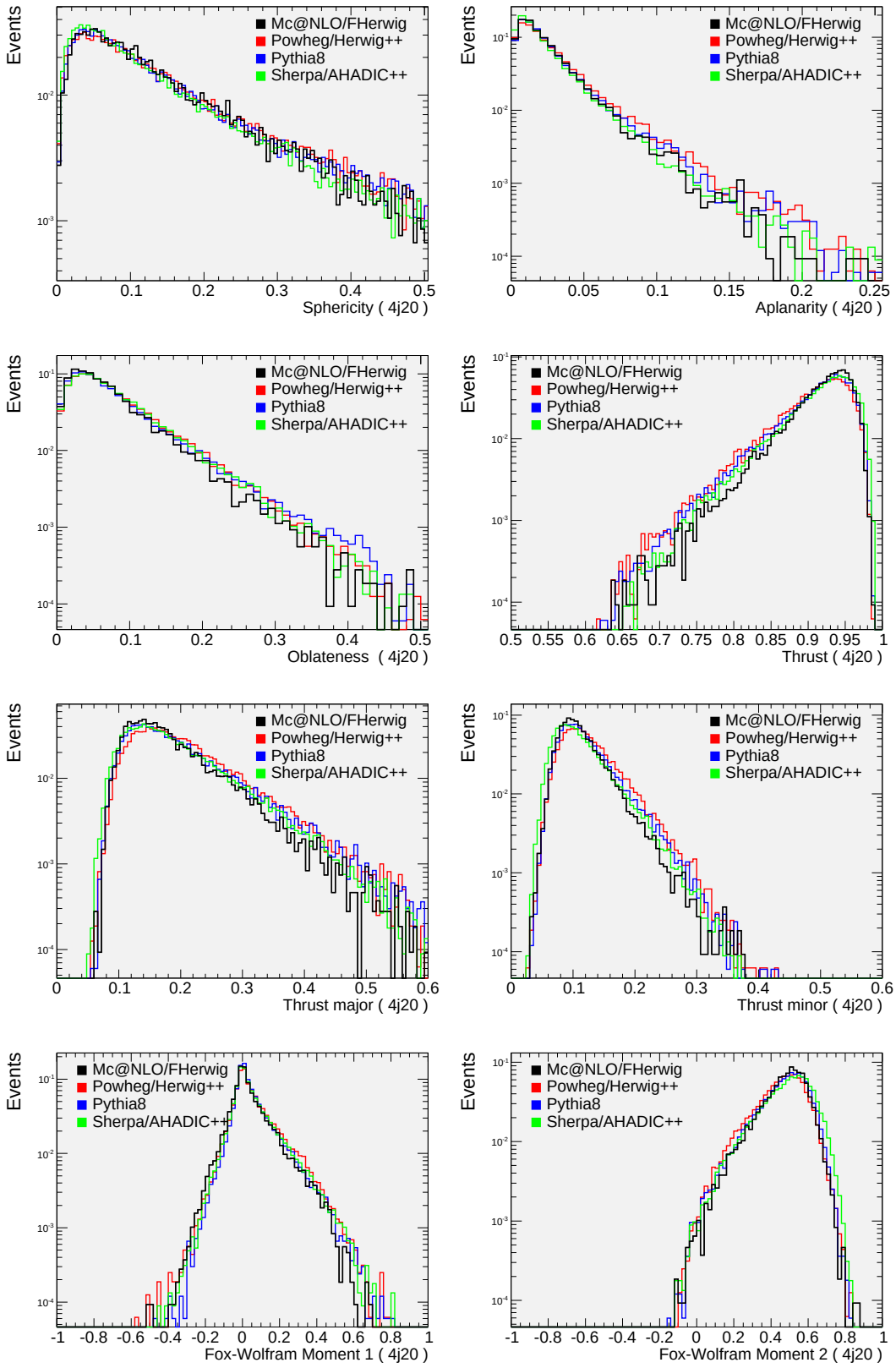

Figure 1.19: $t\bar{t}$ **: Event shape variables**

- Sherpa 1.1.3

Given the large production cross section of about $10^8 pb$, the storage of such a large amount of data proved to be challenging. As a matter of fact, only HERWIG and Pythia gave the possibility to generate few pb of data applying the preselection *on-the-fly*, so that events have been analyzed but not stored on disk. However, it must be stressed that those programmes can generate only 2-partons matrix elements, so that their description of QCD multijet background is less accurate than Sherpa's.

Event generation with Sherpa has been split in sub-samples with homogeneous parton multiplicity. In order to improve the preselection efficiency, cuts have been applied on partons' p_T, depending on parton multiplicity. Every parton must have a transverse momentum $p_T > 17\ GeV/c$.

As result, HERWIG events have a leading jet p_T on average greater than Pythia, and contain more central jets. Sherpa events are even more central, with a leading jet p_T halfway between the other two generators. Event shape variables are less in agreement among each other than for $t\bar{t}$ events.

1.3.5 A Possible Further Development: Discrimination Using a Likelihood Function

In order to discriminate between the $t\bar{t}$ signal and the QCD MJB it is possible to use a likelihood function built up from the topological variables studied so far. These variables are histogrammed for the two samples and normalized to unity. The logarithms of probability ratios $\ln \frac{\mathcal{P}(t\bar{t})}{\mathcal{P}(QCD)}$ are parametrized with functional fits to obtain the probability density functions $\ln(S_i/B_i)$ for the input variables. Assuming that the input variables are uncorrelated, the likelihood function can be approximated to:

$$\mathcal{L} = \frac{S(q_1, q_2 ... q_N)}{S(q_1, q_2 ... q_N) + B(q_1, q_2 ... q_N)} \sim \frac{\Pi_i S_i}{\Pi_i S_i + \Pi_i B_i} = \frac{\exp\left(\sum_i \left(\ln \frac{S_i}{B_i}\right)\right)}{\exp\left(\sum_i \left(\ln \frac{S_i}{B_i}\right)\right) + 1} \quad (1.32)$$

However, it is already well known that the QCD multi-jet background does not represent a huge challenge for searches regarding $t\bar{t}$ semi-leptonic decays. Cutting on E_T^{miss} , the number of jets and requiring an isolated leptons throws

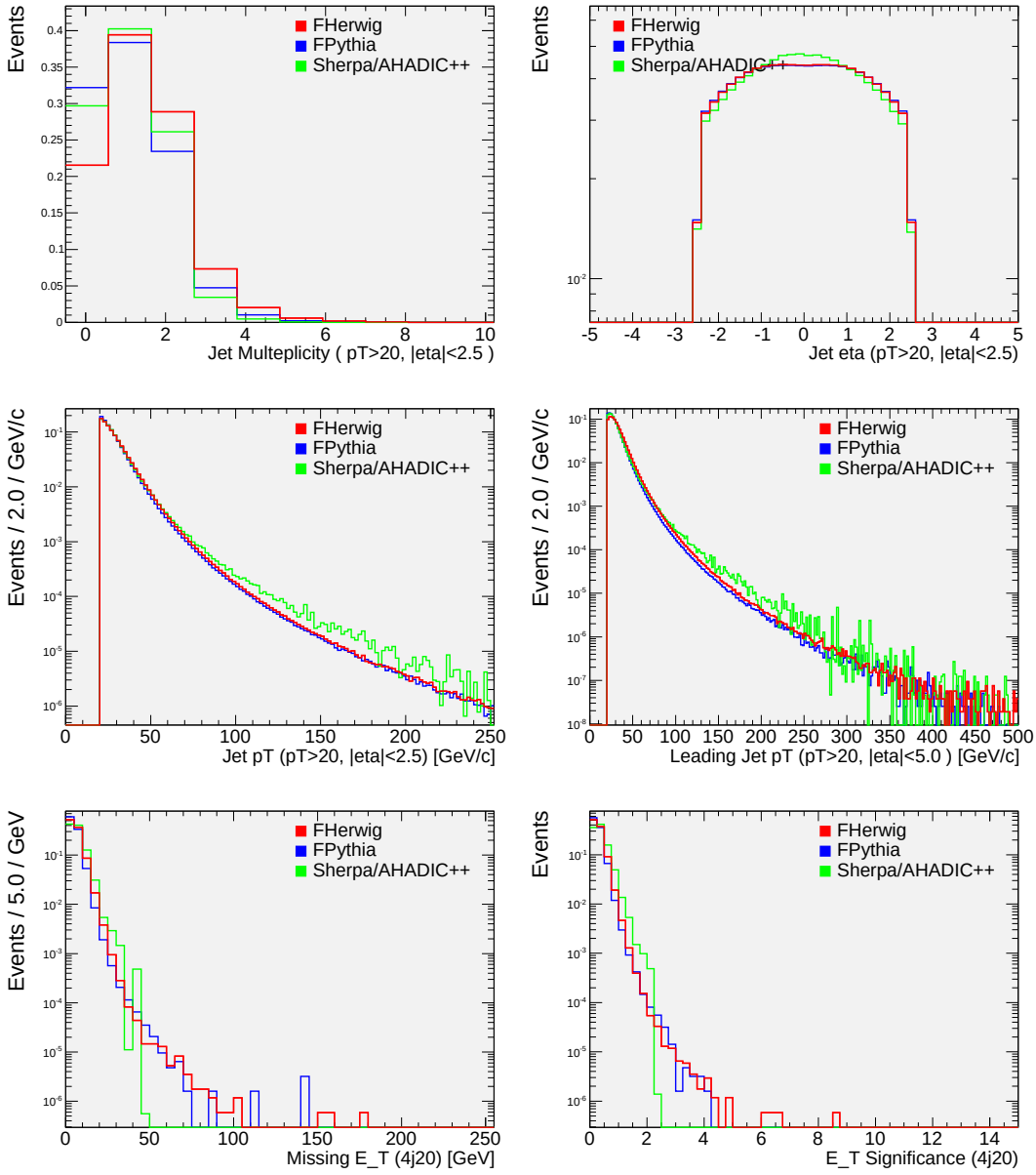

Figure 1.20: **QCD : Kinematical variables**

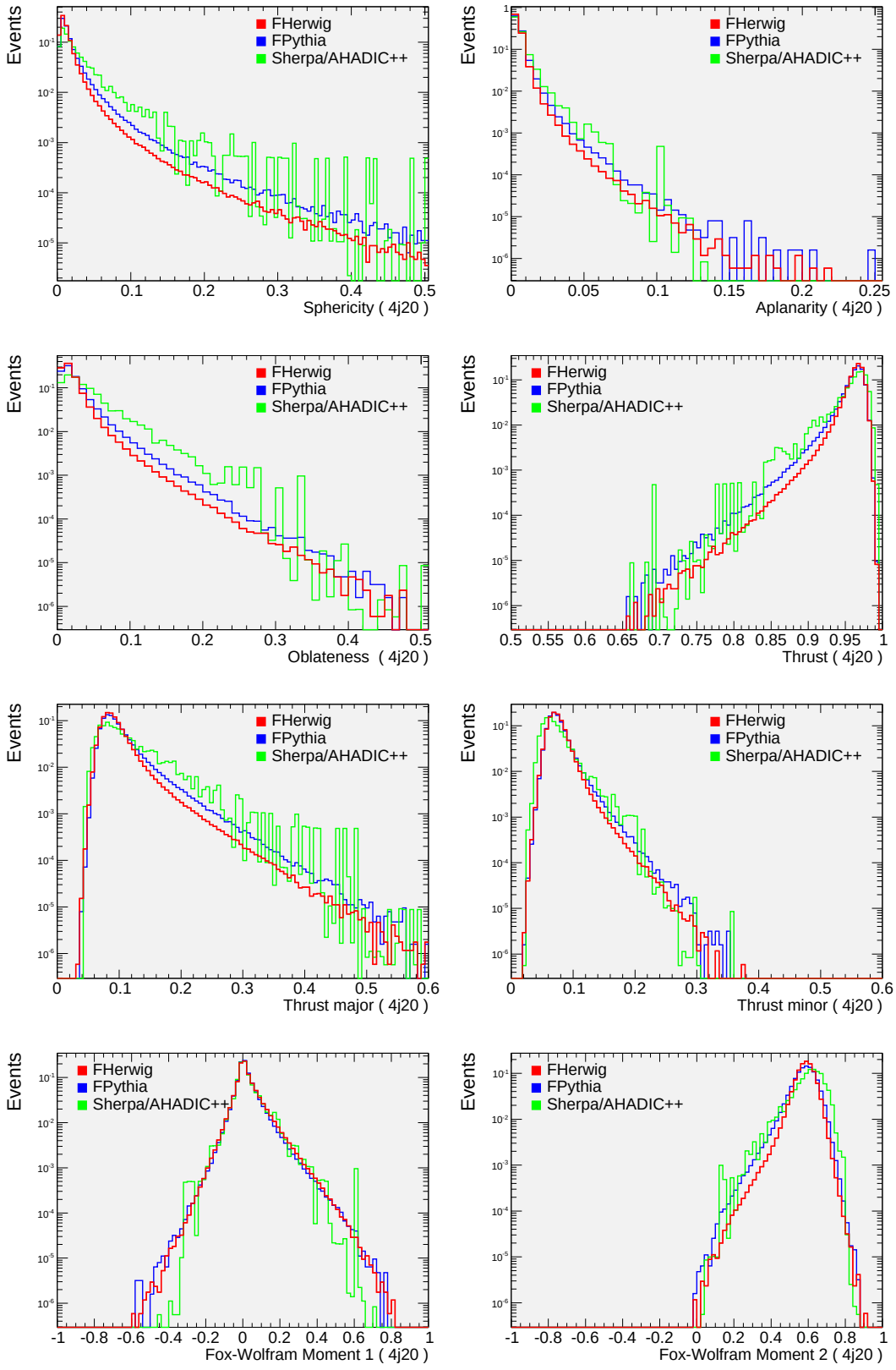

Figure 1.21: **QCD : Event shape variables**

away all this background, at least for all practical purpouses. This will be discussed in chapter 3. The likelihood method, along with neural networks can be used for other decay channels, in particular for the full-hadronic.

1.3.6 Conclusions

Generators for top quark events show an overall very good agreement among each other. In this work, "new" generators have been compared to the benchmark, MC@NLO. The overall agreement assures that the systematic errors linked to the choice of the Monte Carlo generator is small if not negligible. As for the QCD multi-jet background, there are some differences in event shape variables between PYTHIA and HERWIG. The statistics obtained with SHERPA is too small and it is almost impossible to evaluate these differences at the tails of the distributions. In the end, in the case of QCD multi-jet it is suggested to evaluate systematics error linked to the Monte Carlo generator with a deeper level of accuracy.

1.4 The POWHEG method and its implementation

The POWHEG (*POsitive-Weighted Hard-Emission-first Generator*) method is a prescription for interfacing NLO calculations with parton shower generators. Until now, the POWHEG method has been applied to the following processes: Z pair hadro-production, heavy-flavour production, e^+e^- annihilation into hadrons and into top pairs, Drell-Yan vector boson production, W' production, Higgs boson production via gluon fusion, Higgs-strahlung and vector boson fusion, single-top production and Z+1 jet production [46]. Unlike MC@NLO, POWHEG produces events only with positive and constant weight, and does not depend on the Monte Carlo program used for subsequent showering. It has been successfully interfaced to HERWIG and PYTHIA.

1.4.1 The POWHEG Formalism

In a shower Monte Carlo, the radiation of a light parton is generated using an algorithm that resums all the leading log corrections to the tree-level ampli-

tude (also known as *Born process*, *i.e.* the squared matrix elements). The hardest emission is generated according to the formula:

$$d\sigma = B(\Phi_B)d\Phi_B \left[\Delta(0) + \frac{R(\Phi_B, \Phi_R)}{B(\Phi_B)}\Delta(k_T)d\Phi_R\right] \tag{1.33}$$

where k_T is the transverse momentum of the radiated parton, $B(\Phi_B)d\Phi_B$ is the differential cross section at tree level, $Rd\Phi_R d\Phi_B$ is the real part of the radiation cross section in the MC approximation, which has a collinear singularity when the radiated parton is aligned with the emitting one. The full phase space is composed by the N-body process, typically $2 \to 2$, called Born phase space Φ_B, plus the phase space of the radiated parton Φ_R:

$$\Phi = \Phi^{(N+1)} = \left(\Phi_B^N, \Phi_R\right) \tag{1.34}$$

In turn, Φ_R is parametrized by the variables characterizing the collinear splitting, *e.g.* the momentum fraction z, the splitting angle θ and the azimuthal angle φ.

In the POWHEG method, formula (1.33) is "upgraded" in order to reach next-to-leading order accuracy. This is done as follows:

$$\begin{aligned} d\sigma &= \overline{B}(\Phi_B)d\Phi_B \left[\Delta^{NLO}(0) + \Delta^{NLO}(k_T)\frac{R(\Phi)}{B(\Phi_B)}d\Phi_R\right] + \\ &\quad + [R - C]\, d\Phi \qquad (1.35) \\ \overline{B}(\Phi_B) &= B(\Phi_B) + V(\Phi_B) + \int d\Phi_R \left[R(\Phi_B) - C(\Phi)\right] \qquad (1.36) \\ \Delta^{NLO}(k_T) &= \exp\left[-\int d\Phi_R \frac{R(\Phi)}{B(\Phi_B)}\Theta(k_T - P_T)\right] \qquad (1.37) \end{aligned}$$

The NLO cross section is calculated from the leading-order cross-section $B(\Phi_B)$, enhanced by virtual (loops) plus unresolvable $V(\Phi_B)$ and real $R(\Phi_B)$ corrections. Real corrections are regulated by a counterterm $C(\Phi)$ that tames singularities due to collinearity. Since $C \leq R$ and in the soft and collinear limits $R \to C$, the choice $C = R$ is often made. $\Delta^{NLO}(k_T)$ is the POWHEG Sudakov form factor, representing the probability of non-emission at next-to-leading order, where P_T is the transverse momentum of the hardest emission and Θ is the Heaviside step function which prevents k_T to be less than the

threshold P_T.

In a parton shower simulation, one generates a N-body configuration at the leading-order according to $B(\Phi_B)$ and then showers it using the Sudakov form factor. In the POWHEG mechanism, a N-body configuration is generated according to $\overline{B}(\Phi_B)$, and is kept as-is with a probability $\Delta^{NLO}(0)$ (non-radiative event) or showered to give the hardest emission with $k_T = P_T$ and probability $\Delta^{NLO}(P_T)$. From this point onward, lower k_T emissions are indeed at NNLO and beyond, so the usual parton shower Monte Carlo process can be used.

Provided the perturbative approach is valid, next-to-leading order terms are *smaller* than LO ones, thus $\overline{B}(\Phi_B)$ is *positive* and no events with negative weights are ever generated. Moreover, parton showers are angularly-decomposed in a very neat way: first come wide-angle soft-gluon emissions (*truncated shower*), then *hardest-emissions* (the POWHEG method), and eventually *vetoed showers* are produced at lower p_Ts, towards collinear emissions. To preserve the soft radiation distribution, the addition of the truncated shower of soft coherent radiation before the hardest emission is necessary. This radiation has a low energy and it does not appreciably lower the hardest emission. This is the main reason why in the POWHEG method soft gluons are generated before the hardest emission. One show keep in mind that this is only a first-order but reasonable approximation since the probability of emitting an extra gluon is small.

1.4.2 Comparison at Generator Level

POWHEG has been extensively validated against its principal "competitor" MC@NLO, which is a generator at next-to-leading order [45]. In fact, in these two programs the hardest radiation can be described by a similar formula thus allowing a better understanding of the agreement and discrepancies between the two approaches.

The comparison has been done for a semi-leptonic sample validated against the standard MC@NLO sample used as a benchmark in the ATLAS experiment. Both samples are showered using HERWIG (this is so far the only choice for MC@NLO). However, the same POWHEG sample has been showered with

Pythia, and validated against the HERWIG-showered one. A test is under way in order to shower the same sample with HERWIG++ [17].

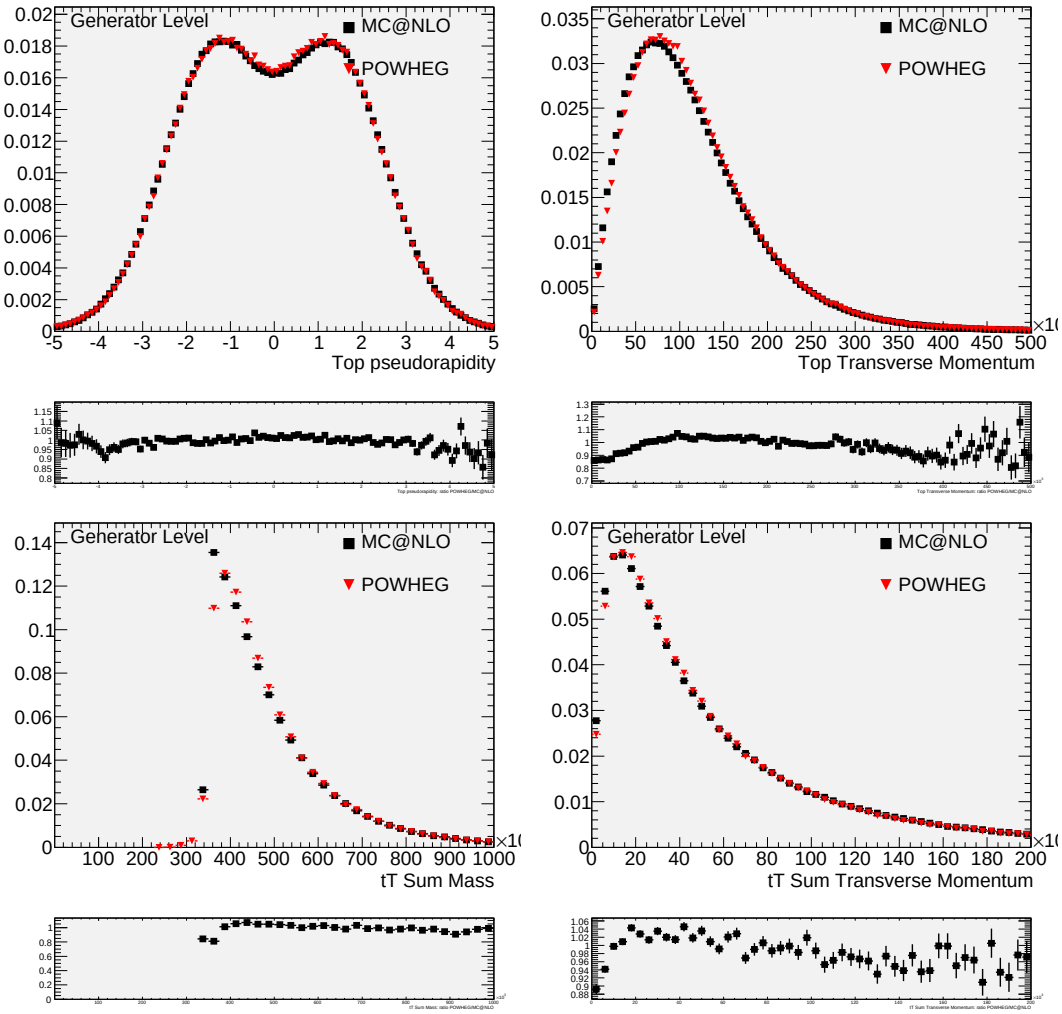

Figure 1.22: Comparison between POWHEG and MC@NLO at the generator level. Top quarks pseudorapidity, transverse momentum (upper row), mass and momentum of the sum of $t\bar{t}$ four-vectors (lower row).

1.4.3 The Dip Problem

A remarkable discrepancy has been spotted between POWHEG and MC@NLO [45], which is known as "the dip problem". In fact, a dip in the rapidity distribution of the hardest jet of MC@NLO was found, that is not present neither in

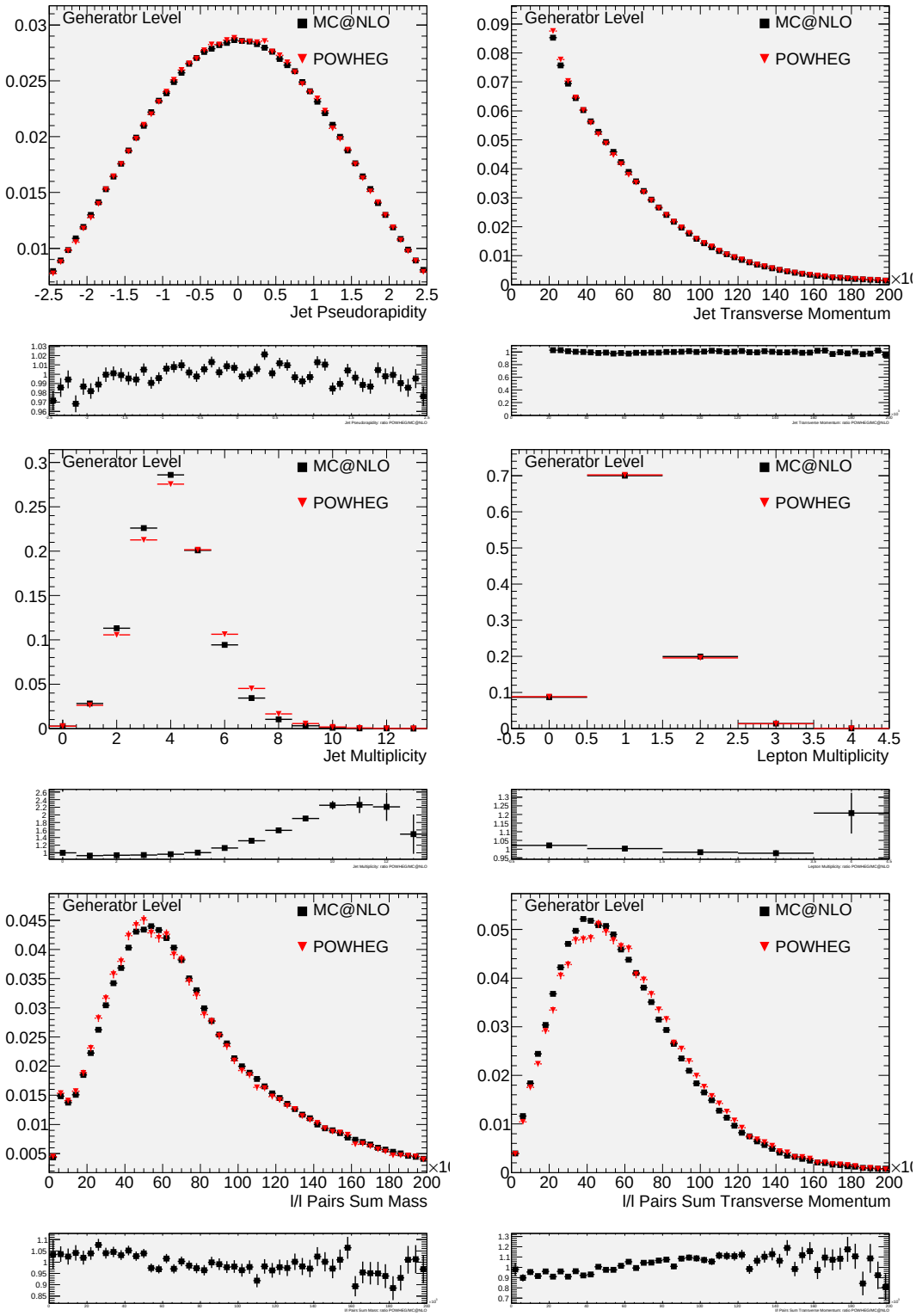

Figure 1.23: Comparison between POWHEG and MC@NLO at the generator level. Jet (upper row) pseudorapidity, p_T, multiplicity of jets and leptons (middle), mass and p_T of the sum of lepton four-vectors.

ALPGEN nor in POWHEG (see figure 1.24). This feature has been proven to be present in several processes, and is particularly evident for the Higgs production. The HERWIG sample has a dip in the rapidity distribution at zero. MC@NLO has a similar dip, although less pronounced. No dip is present in POWHEG. In HERWIG, multiple radiation is treated in the soft or collinear approximation and no emission is permitted in the so-called *dead zones*, which correspond to hard and large-angle parton radiation. In fact, the HERWIG algorithm can be improved by applying matrix-element corrections so that the dead zone is populated by the use of the exact first-order matrix element (*hard correction*) and the $O(\alpha_S)$ result is used in the already-filled region any time an emission is the hardest so far (*soft correction*) [25].

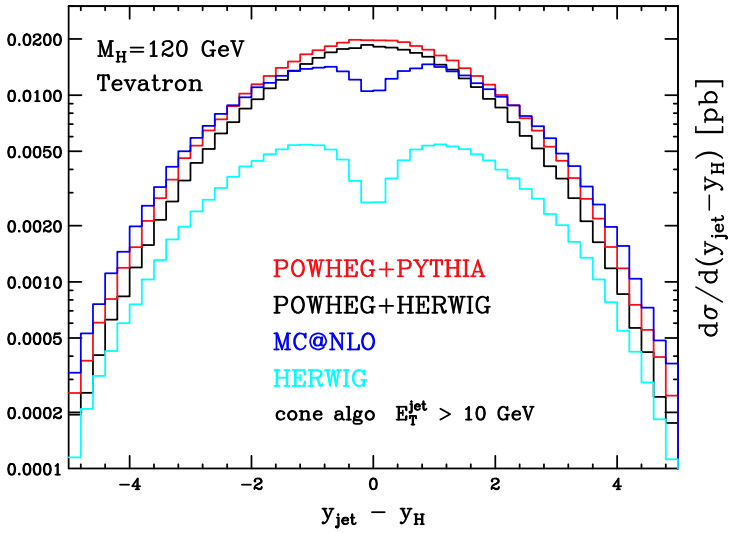

Figure 1.24: The rapidity distribution of the hardest jet for HERWIG, MC@NLO and POWHEG, giving rise to the so-called "dip problem".

The explanation can be found in equation 1.35: in the limit of large k_T the cross-section approaches:

$$\lim_{k_T\to\infty} d\sigma = \overline{B}\frac{R}{B}d\Phi + (R-C)d\Phi = Rd\Phi + \left[\frac{\overline{B}}{B} - 1\right] Rd\Phi \qquad (1.38)$$

The second term is in the order of α_S and can be considered "small" in a perturbative sense. However, it is not always true that NLO corrections are small: in fact, for some processes like Higgs production, they can lead to a cor-

rection up to $\sim 100\%$ and the second term is in the order ~ 1 . Since $R(\Phi_B, \Phi_R)$ represent the Monte Carlo approximation (in this case by HERWIG) of the real cross-section, it turns out that its "dip" due to *dead zones* propagates to the NLO cross-section as calculated by MC@NLO. It has been shown that replacing the B cross section contribution in MC@NLO with $\overline{B}$, this effect disappears.

1.4.4 Comparison after full simulation of the Atlas detector

At present, comparison can be done only between MC@NLO and POWHEG samples showered with HERWIG, due to the lack of other datasets. Anyway, once the validation has been done at generator level, this kind of comparison adds little information about the compatibility of the two generators. However, it remains extremely important to have more than just one program, so that an evaluation of the systematic error related to the two different methods can be carried out. As shown in figures 1.25 and 1.26, the two programs agree remarkably well with only small departures for few bins with low statistics for the POWHEG sample, where the errors are anyway quite large.

1.4.5 Standard commissioning analysis for semileptonic $t\bar{t}$ decays

The standard commissioning analysis has been applied to both POWHEG and MC@NLO samples. For a detailed discussion of how it is performed, see [16] and section 3.2. It is worth remembering that the requirements are a single electron or muon, missing transverse energy greater than $20\ GeV$, four jets with $p_T > 20\ GeV$ of which at least 3 with $p_T > 40\ GeV$. After that, the combination of jets with highest transverse momentum is picked to reconstruct the top quark decayed hadronically. Additionally, two of these "top" jets are selected to reconstruct the W boson that decayed hadronically. Figure 1.26 shows the comparison between the reconstructed quantities for the two $t\bar{t}$ samples. It is evident that their agreement is as good as for the other variables.

1.4.6 Conclusions

Recently, POWHEG proved to be a viable alternative to MC@NLO, fixing some problems (like the dip issue) and being easier to be utilized for end-used since

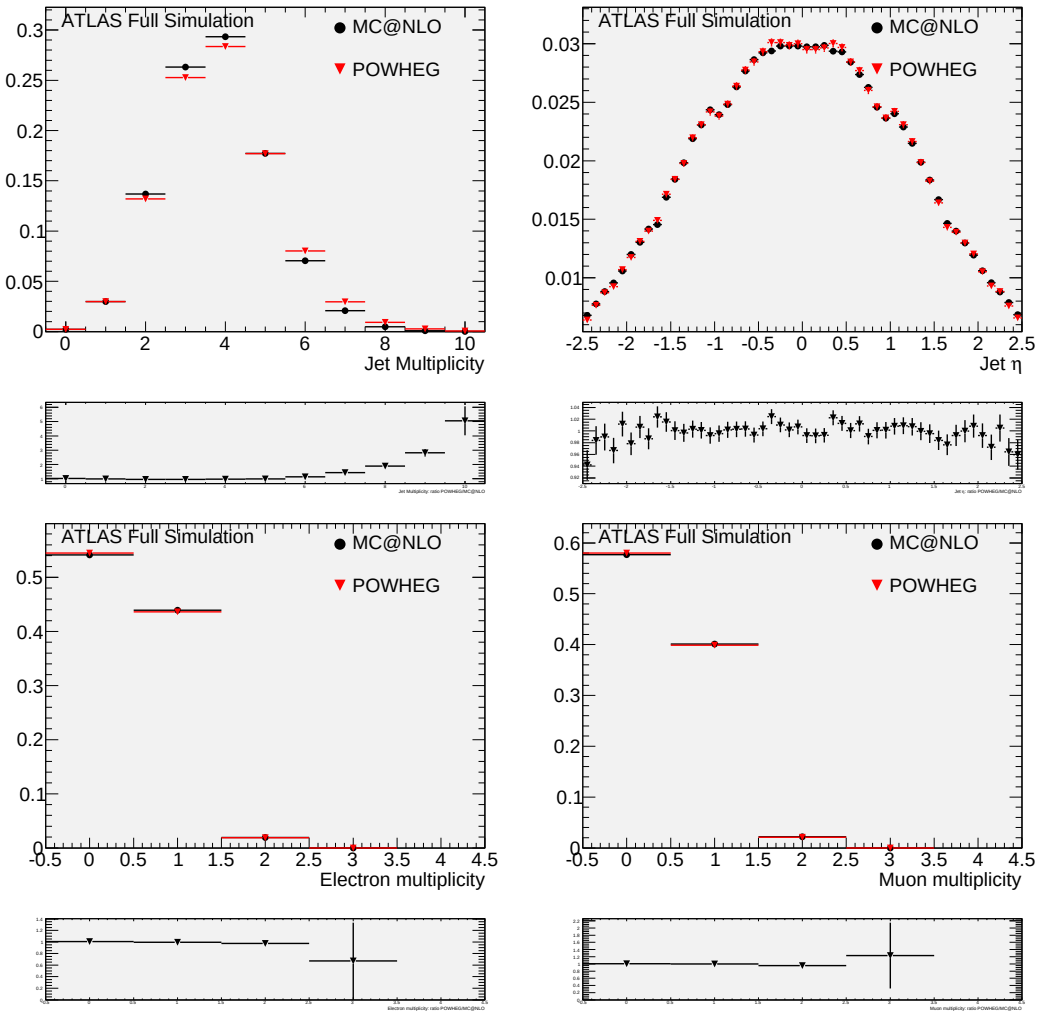

Figure 1.25: Comparison between POWHEG and MC@NLO after the full simulation of the ATLAS detector. Jet multiplicity and pseudorapidity (top), multiplicity of electrons and muons (down).

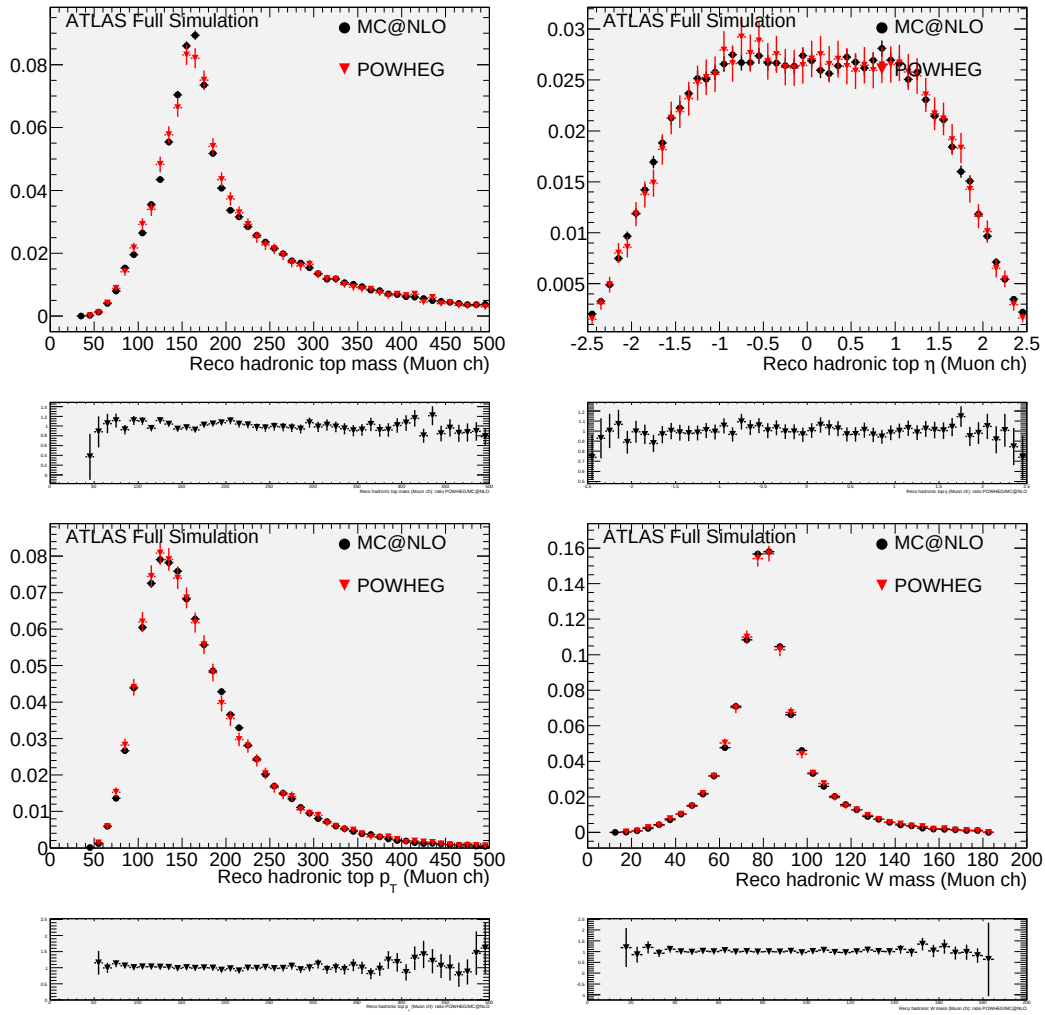

Figure 1.26: Comparison between POWHEG and MC@NLO after the full simulation of the ATLAS detector. Reconstructed hadronic top mass and pseudorapidity (upper row), hadronic W mass and p_T (lower row).

it does not give rise to cumbersome negative-weighted events. The POWHEG method is being implemented in several processes in HERWIG++ and will be probably considered an important milestone in the development of Monte Carlo generators for the physics at the LHC, where computations at next-to-leading order will be mandatory. In fact, searches for New Physics require an extremely high accuracy in the simulation of processes due to the smallness of some predicted and very interesting Beyond the Standard Model scenarios [52] [53] [24].

Chapter 2

The ATLAS Detector and its Expected Performances

2.1 The ATLAS detector: An Overview

At the interaction Point 1 of the Large Hadron Collider (*LHC*) is placed Atlas (**A** **T**oroidal **L**HC **A**pparatu**S**). Atlas is a multi-pourpose detector which makes use of *state-of-the-art* techniques to detect particle in the high-energy regime. Atlas has been designed and built in order to understand the origin of electroweak symmetry breaking and, entering into a new range of energy never observed before in a laboratory, possibly to discover so-called New Physics such as additional symmetries of Nature (*e.g.* Supersymmetry) or even extra dimensions (*e.g.* via Z' bosons and mini black holes production). Not knowing what to expect exactly, Atlas has been designed to have much flexibility as possible in a large range of energy, spanning from 900 GeV to 14TeV in the *center-of-mass*.

A schematic picture of the detector is shown in figure 2.1. The detector is segmented in three sections, the central being called the barrel and the outer two the end-caps. It is customary to use the coordinate system (η, ϕ, z) to tell the position of a particular point in Atlas *w.r.t.* the *interaction point*, where $\eta = -\ln\tan\frac{\theta}{2}$ is the pseudorapidity, θ is the polar angle, the z direction is defined to be along the beam axis and ϕ is the azimuthal angle.

The pseudorapidity η is particularly useful: in fact, the quantity called *rapidity* $y \equiv \ln\frac{E+p_z}{E-p_z}$ is invariant under longitudinal boosts, and this quantity ap-

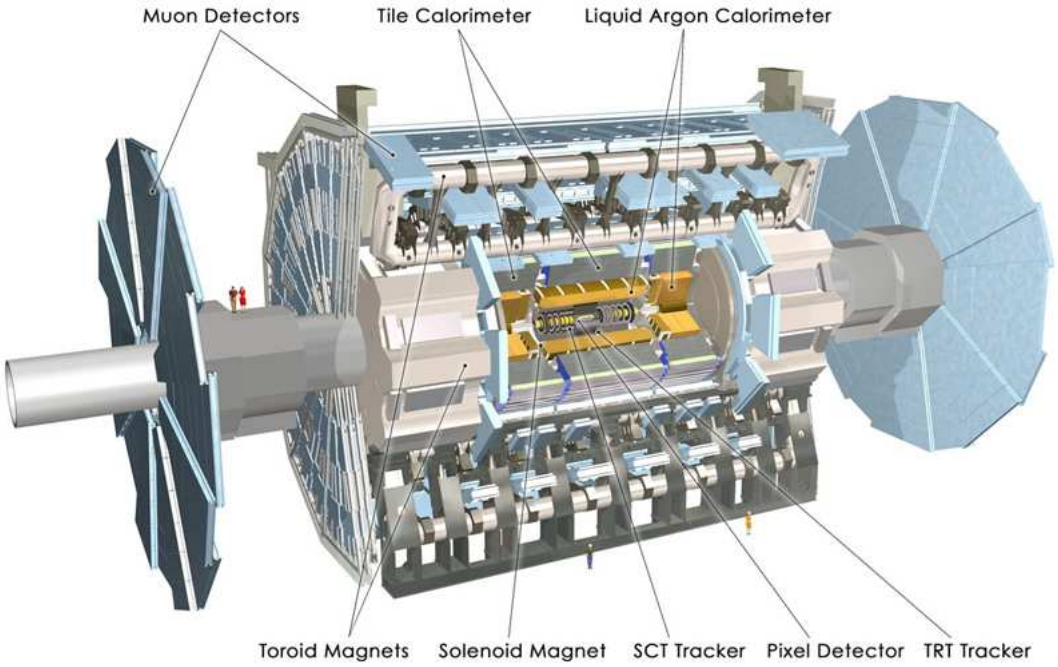

Figure 2.1: Layout of the Atlas Detector.

proaches the pseudorapidity in the limit $m \to 0$. Moreover, the production of particles is almost uniform in ϕ for a given value of η. The vertical plane placed at $z = 0$ splits the detector in the two halves referred to as side A ($z > 0$) and C ($z < 0$).

Magnet System The Atlas detector has a peculiar magnetic system designed to minimize the multiple scattering of muons. To do that, the muon spectrometer in placed in air, immersed in a toroidal magnetic field. The magnetic system is made of a central solenoid (CS), an air-core central toroid (CT) and two end-caps air-core toroids (ECT). The CS surrounds the Inner Detector and provides a magnetic field of $2\ T$ along its length of $5.3\ m$. The barrel toroid (BT) consists of eight flat coils assembled radially and symmetrically around the beam axis. The magnet system is completed by the two ECT placed at the end of the BT, aligned to the CS. Like the BT, each of the ECT is made of 8 coils rotated by an angle of $22,5^o$ with respect to the BT coils to overlap the two fields and to optimize the particle bending in the transition regions. The magnetic field outside the CS has a strength of $0.5\ T$

Tracking System The main reason of placing a magnetic field in a particle detector is to bend charged particles while detecting them with a tracking system. In a high-rate environment such as the LHC, the Atlas inner tracker must be able to reconstruct a large number of tracks at the highest possible luminosity that the accelerator will be able to deliver. The inner tracker system is based on three different technologies, Silicon Pixels, Silicon Strips (SCT) and Transition Radiation Tubes (TRT, or Straw Tube Tracker).

The Silicon Pixel detector consists of three coaxial layers in the barrel region and four end-cap disks on each side for a total of 140 million detecting elements. The fine segmentation of $50\mu m$ in $R-\phi$ plane and $300\mu m$ in z provides enough resolution to reconstruct tracks using a pattern recognition system near the interaction point. This will be very important to identify primary and secondary vertices of particles such as B mesons. The inner tracker has been designed to survive to a huge amount of radiation that will be accumulated in 10 years of operations, yielding almost $500\ fb^{-1}$ of data.

The TRT is based on $4\ mm$ tubes filled with a xenon gas mixture, containing a sense wire. These tubes are placed parallel to the beam direction in the barrel, and arranged in disks on the end-caps. TRT tubes are capable to detect the radiation emitted by a charged particle while traversing the interface between two media of different dielectric constants travelling at relativistic speed. It can discriminate on the particle velocity, allowing electron/pion rejection. The transition radiation emitted by a charged particle depends on its Lorentz factor $\gamma = E/mc^2$ and it is mostly directed forward, peaking at an angle of the order of $1/\gamma$ relative to the particle path. The intensity of the emitted radiation is roughly proportional to the particle's energy E. For a given energy, this allows a discrimination between a lighter particle (which has a high γ and therefore radiates) and a heavier particle (which has a lower γ and radiates much less).

This system as a whole is able to provide 36 hits per track, with a resolution of about $170\mu m$ on each hit and of $50\mu m$ on a fitted track.

Calorimeters Most of the physics channels will rely heavily on the performance of the calorimeters (figure 2.2). A very accurate measurement of energy and position of electromagnetic and hadronic showers will be extremely important for solid measurement of missing transverse energy. In fact, this quan-

tity will play an important role in the search for Beyond the Standard Model physics.

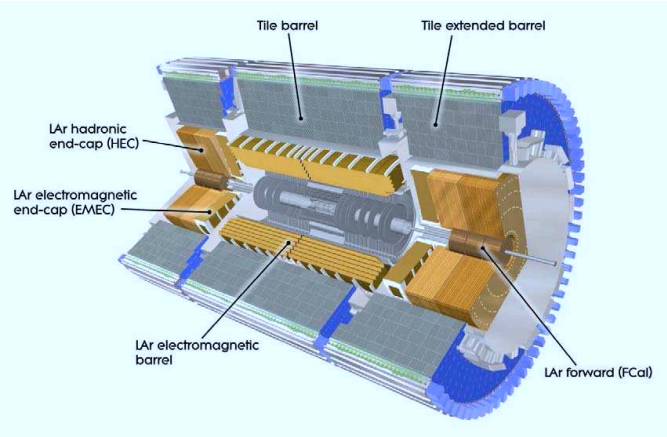

Figure 2.2: Layout of Atlas Calorimeters.

The electromagnetic calorimeter of Atlas (ECAL) is a sampling calorimeter made of lead and liquid argon (LAr), with the absorbers resembling the shape of an accordion to provide good uniformity along the ϕ direction. It is segmented into a barrel region ($|\eta| < 2.3$) and two end-caps. Three levels of granularity ($\Delta\eta \times \Delta\phi = 0.003 \times 0.1$ for 6 radiation lengths (X_0), 0.025×0.025 for $16X_0$ and 0.1×0.0982 for the outer $2X_0$) provide an energy resolution of:

$$\frac{\sigma_E}{E} = \frac{9.23 \pm 0.09\%\ GeV^{1/2}}{\sqrt{E(\ GeV)}} \oplus 0.21 \pm 0.02\% \tag{2.1}$$

as measured in test beams. The ECAL has been designed to identify electrons and photons with a transverse momentum ranging from $1\ GeV$ to $5TeV$. This will be important in order to reconstruct, among others, Higgs boson decays such as $H \to \gamma\gamma$, $H \to ee$, heavy bosons decay such as a$Z' \to ee$ with high statistical significance.

The ECAL is surrounded by the Hadronic Calorimeter (HCAL), which main purpose is to measure the energy and direction of jets of particles coming from the decayed hadrons (see section 1.3.2). The HCAL consists of a *Hadronic Tile Calorimeter* (HTC) made of iron and plastic scintillator in the barrel region ($|\eta| < 1.7$), a LAr sampling calorimeter in the end-caps (*Hadronic End-caps Calorimeter*, HEC) for $1.5 < |\eta| < 3.1$ and a Forward Calorimeter (FCAL), very

close to the beam pipe, made of LAr, iron and tungsten. There is a small gap ($600mm$) between the barrel ($|\eta| < 1$) and the extended barrel ($1 < |\eta| < 1.7$) regions to allow the passage of ID and ECAL cables. The total interaction length (λ_I) is $10\lambda_I$.

Atlas HCAL has an energy resolution has been measured in test beams:

$$\frac{\sigma_E}{E} = \frac{50\%}{\sqrt{E(\,GeV)}} \oplus 3\% \qquad (HTC, |\eta| < 1.7) \tag{2.2}$$

$$\frac{\sigma_E}{E} = \frac{50\%}{\sqrt{E(\,GeV)}} \oplus 10\% \quad (HEC, 1.5 < |\eta| < 3.2) \tag{2.3}$$

$$\frac{\sigma_E}{E} = \frac{100\%}{\sqrt{E(\,GeV)}} \oplus 3\% \quad (FCAL, 3.1 < |\eta| < 4.9) \tag{2.4}$$

The granularity is $\Delta\eta \times \Delta\phi = 0.1 \times 0.1$ for $|\eta| < 2.5$ and 0.2×0.2 for $2.5 < |\eta| < 3.2$.

Muon Spectrometer The outer section of the Atlas detector is the muon spectrometer (figure 2.3). It will play a very important part in many cutting-edge searches for both SM and BSM physics, such as Higgs boson, top quark and Z'. The requirements of high quality measurements for muons has characterized significantly the design of the ATLAS detector. The muon spectrometer, in principle, should to be able to perform physical measurements without informations coming from other subdetector. This is usually referred to as *standalone operation*. Particle trajectories are measured three times inside the toroidal magnetic field in order to measure the momentum of each muon candidate.

The MS is made of 16 sectors associated with each of the coils of the magnetic system. Four kind of detectors are deployed: *Monitored Drift Tubes* (MDT) and *Cathode Strips Chambers* (CSC) provide coordinates in the bending plane, while *Resistive Plate Chambers* (RPC) and *Thin Gap Chambers* (TGC) generate the trigger signal in the barrel and end-cap regions (fig.2.8). MDTs and RPCs are coupled in small triggering sub-systems called *stations*. The solid angle coverage is not complete due to gaps left for cables and lift in the very central area. The end-cap chambers will cover the pseudo-rapidity range $1 < |\eta| < 2.7$ and are arranged in four disks at distance of $7\ m$, $10\ m$, $14\ m$ and $21 - 23\ m$ from the

interaction point (IP). In the barrel region, the MS is divided in three coaxial cylindrical regions defined as *Inner*, *Medium* and *Outer*. In the transverse plane the eight coils divide the MS in 16 sectors.

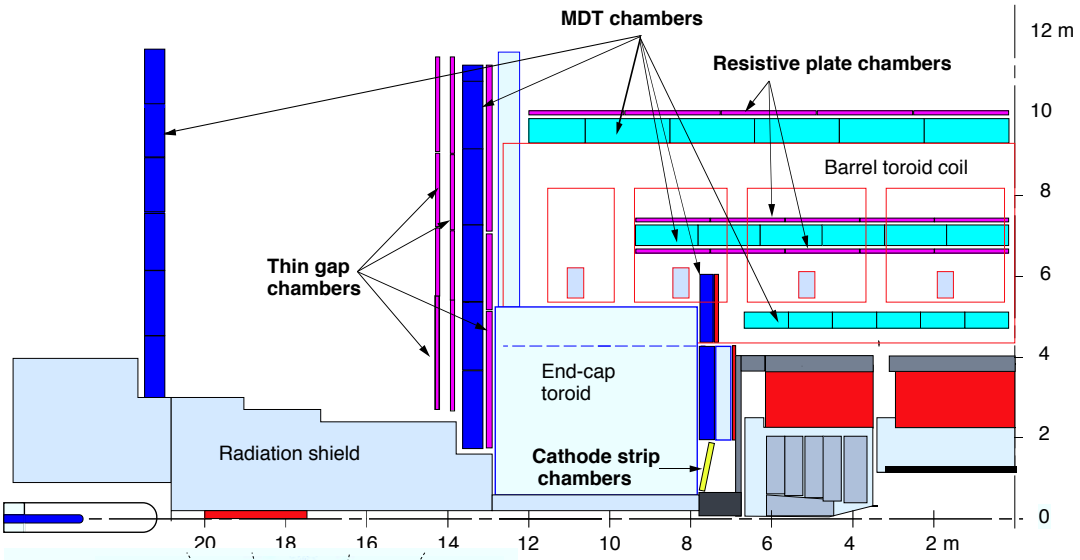

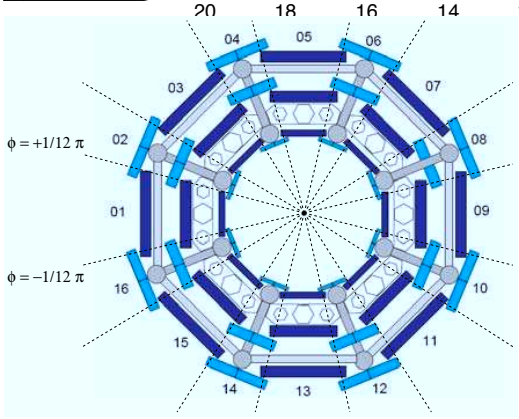

(a) ϕ-binning

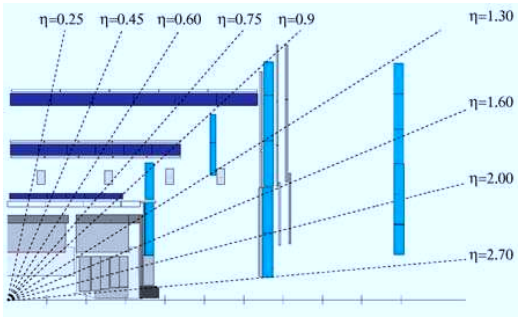

(b) η-binning

Figure 2.3: Layout (top) and η- and ϕ-binning (bottom) of the muon spectrometer.

Precision measurement of the trajectory is made using **Monitored Drift Tubes** (figure 2.4). These are straw tubes filled with an admixture of Ar/CO_2, which provide a gain of 2×10^4 when operated at $3\ bar$ pressure. A single tube is able to provide a spatial resolution of $80\ \mu m$, while a multilayer block improves this value to $50\ \mu m$. To keep the geometry of a multilayer as constant as possible, each group is monitored with an optical alignment system.

Cathode Strips Chambers provide better spatial resolution than MDT in

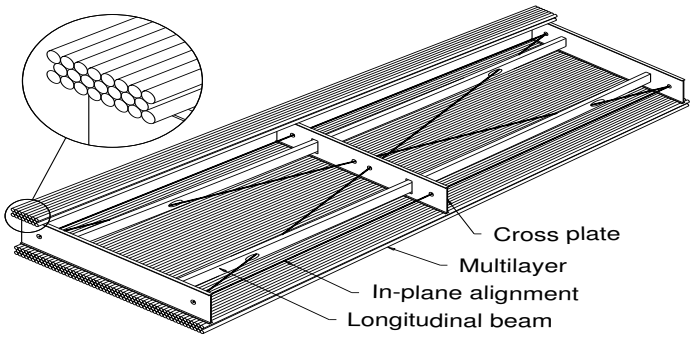

Figure 2.4: Layout of a Monitored Drift Tube (MDT).

the $2 < |\eta| < 2.7$ region, where the background is larger than the one measured in the barrel. CSC are *Multi-wire projection chambers* (MWPC) filled with an admixture of $Ar/CO_2/CF_4$. The sense-wire pitch is $2.54\ mm$. The cathode is segmented into strips orthogonal to the anode wires. A charge interpolation method is deployed to determine which wire was the closest to the particle passage. This provides a spatial resolution of $60\ \mu m$.

Resistive Plate Chambers (figure 2.5) give the trigger to Atlas in the barrel region, thus they have been designed to have a dead-time shorter than the LHC's bunch-crossing time (a few ns). The threshold in muon momentum is set to reject low-p_T background *e.g.* from the cavern, and they provide an additional position measurement with a resolution of $10 - 20\ mm$. In fact, MDTs provide position measurement only along the bending direction. Each RPC unit uses two gas volumes made of low resistivity plastic laminated electrodes, and four planes of read-out strips. The active material is a gas mixture composed by 94.7% of $C_2H_2F_4$, 5% of $isoC_4H_{10}$ and 0.3% of SF_6.

Thin Gap Chambers (figure 2.6) give the trigger in the end-caps region. Time resolution has been measured to be in the order of $4\ ns$. TCG are basically MWPC with sense-wire pitch of $1.8mm$ and filled with an admixture of CO_2/n-pentane, operating in saturation mode. Pickup strips provide the coordinate along the wire axis. Multilayers made of TGCs are placed in the middle tracking station. The inner station features some TGC to increase the tracking ability.

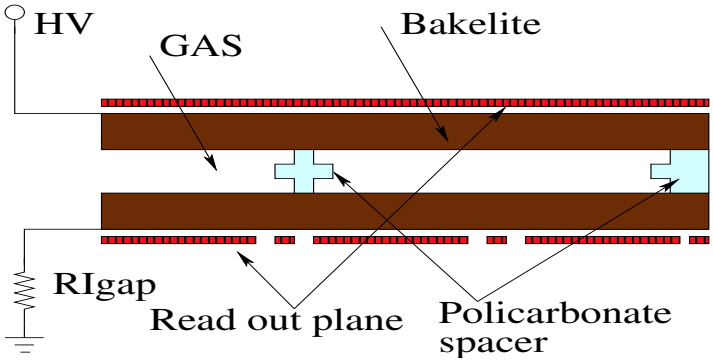

Figure 2.5: Layout of a Resistive Plate Chamber (RPC).

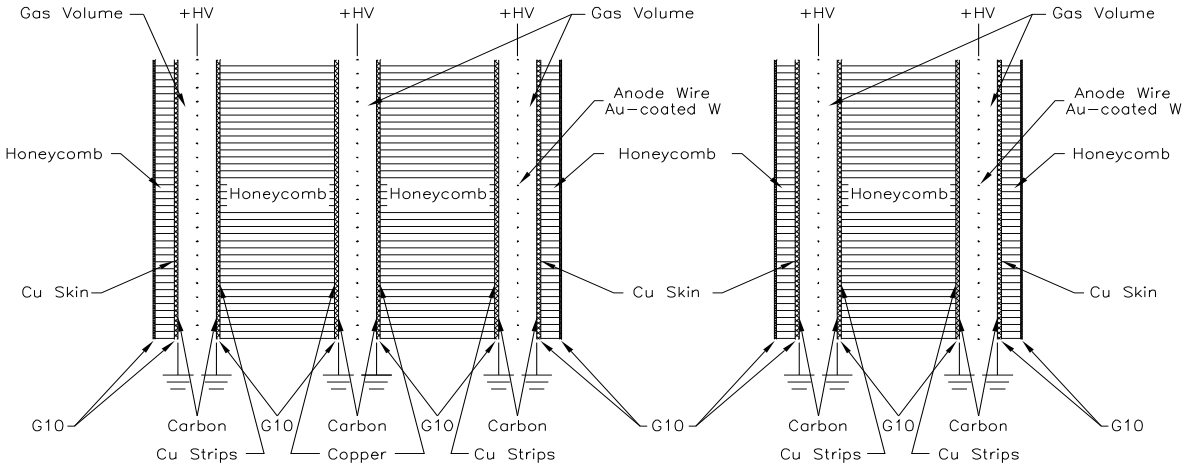

Figure 2.6: Layout of a Thin Gap Chamber (TGC).

2.2 Triggering $t\bar{t}$ events

The Atlas trigger is segmented in three levels: Level-1 (L1), which is hardware-based, Level-2 (L2) and the Event Filter (EF), known together as High-Level Trigger (HLT), that are performance-optimised software-based, running on a dedicated computer farm. These three level must reduce the initial event rate ($\sim$ 40 MHz) to an acceptable storage rate of $\sim$ 200 Hz. A large rejection is needed against QCD processes, whose cross section is about $1\ mb$, while maintaining a high efficiency in identifying low cross-section physics such as electroweak interaction and possible BSM events.

At the beginning, at a center of mass energy of than 7TeV, the instantaneous luminosity won't exceed a low value of about $10^{31} cm^{-2} s^{-1}$. Thus, several trigger chains have been prepared for the commissioning of the system and for the selection of the first data. The low luminosity conditions are favourable for efficiently triggering on top quark events with leptons in the final state. A single lepton (e or μ) trigger with low threshold and loose selection requirements can run without any prescaling, providing a high acceptance trigger for $t\bar{t}$ events. At the initial luminosity of $10^{31} cm^{-2} s^{-1}$, single electron and muon triggers with a 10 GeV threshold have an estimated rate of 14Hz and 11Hz respectively. As the luminosity increases, higher thresholds and tighter selection at HLT will be needed to reject background events. A combination of leptonic, E_T^{miss} and b-tagging triggers will be needed to cope with the higher rates. Table 2.1 shows two trigger chains used in the following studies. In ATLAS, triggers are defined by a prefix indicating the level (L1, L2, EF), the stream name (EGAMMA, MU, JET, XE among others) and a suffix indicating the threshold. If no prefix is present, the whole trigger chain is intended. For instance, mu20 identify the trigger chain that selects events with at least one muon with p_T greater than $20\ GeV/c$, which is made by the logic "AND" of L1_MU20, L2_mu20 and EF_mu20. Some triggers are combination of others (such as mu20_xe30, meaning an event with at least one muon with $p_T > 20 GeV/c$ and missing transverse energy greater than $20\ GeV$) or combined objects such as 2MU10 (at least two muons with $p_T > 10 GeV/c$). It is expected that most of the initial $200\ pb^{-1}$ will be acquired at a luminosity of $10^{32} cm^{-2} s^{-1}$, for which some of the leptonic triggers of interest for $t\bar{t}$ physics (*e.g.* mu10, mu15) will be prescaled, while mu20 will remain unprescaled.

Trigger efficiencies for the single lepton trigger can be evaluated using a *tag and probe* method on $Z \rightarrow ll$ events [24]. One of the leptons that trigger the event is "tagged", and the other is used as a "probe" to measure the trigger efficiency. An uncertainty of 1% can be reached during early data taking, thanks to the very high rate of Z boson production and decay.

In section 2.7 a similar technique is applied to $t\bar{t}$ di-leptonic events, showing that also top quarks can provide a unique environment for an *in-situ* tag-and-probe for low-p_T muons.

Table 2.1: Muon trigger chains used for tag and probe. See text (sec. 2.2) for a more detailed description of these triggers.

	mu10	mu20
L1	L1_MU10	L1_MU20
L2	L2_mu10	L2_mu20
EF	EF_mu10	EF_mu20

2.3 Identification of Electrons

Several interesting channels have small cross-sections and suffer from large backgrounds, as for example QCD multi-jet events, which have a cross-section of $\sim 10^9\ pb$. Therefore powerful and efficient electron identification is needed to observe such signals. The ratio between the rates of isolated electrons and the rate of QCD jets with p_T in the range $20 - 50\ GeV$ is expected to be $\sim 10^{-5}$ at the LHC, almost two orders of magnitude smaller than at the Tevatron $p\overline{p}$ collider. Thus, to achieve comparable performances, the electron identification capability of the LHC detectors must be almost two orders of magnitude better than what has been achieved so far.

Physics channels of prime interest at the LHC are expected to produce electrons with p_T between a few GeV and $5TeV$. In the moderate p_T region ($p_T \sim 20 - 50\ GeV/c$) a jet-rejection factor of $\sim 10^5$ is needed to extract a pure inclusive signal of electrons, rejecting jets faking electrons [24]. Instead, for multi-lepton final states such as $h \rightarrow eeee$, a rejection of ~ 3000 per jet should be sufficient to reduce the fake-electron backgrounds to a level well below that

from real electrons.

The reconstruction and identification of electrons is based on seed-clusters in the electromagnetic calorimeter matched to tracks.

At present, two electron reconstruction algorithms have been implemented in the ATLAS offline software, both integrated into one single package and a common event data model.

- The standard one,which is seeded from the electromagnetic calorimeters, starts from clusters reconstructed in the calorimeters and then builds the identification variables based on information from the inner detector and the EM calorimeters.

- A second algorithm, which is seeded from the inner detector tracks, is optimized for electrons with energies as low as a few GeV, and selects good-quality tracks matching a relatively isolated deposition of energy in the EM calorimeters. The identification variables are then calculated in the same way as for the standard algorithm.

Standard identification of electrons is based on a set of many cuts defined in [24], all of which can be applied independently. The cuts were optimized in up to 7 bins of η and in up to 6 bins of p_T. Three sets of cuts have been defined: loose, medium and tight. This provides flexibility to the users, who may e.g. wish to improve their signal efficiency for rare processes which are not subject to large backgrounds from fakes.

As a consequence, in Atlas electrons are classified as follows:

Loose This set of cuts performs a simple electron identification based only on partial information from the calorimeters. Cuts are applied on the hadronic leakage and shower shape variables involving the middle layer of the EM calorimeter (lateral shower shape and lateral shower width). This set of cuts provides excellent identification efficiency, but low background rejection.

Medium This set of cuts improves the quality by adding cuts on the strips in the EM calorimeter and on the tracking variables. Strip-based cuts are effective in the rejection of $\pi^0 \to \gamma\gamma$ decays. Among these variables there are

- $\Delta E_{max,2}$ the second largest energy deposit in the chosen window, normalized to the cluster energy;
- $\Delta E_s = E_{max,2} - E_{min}$ the difference between the second largest energy deposit and the smallest energy deposit between the two leading maxima in the chosen window;
- $w_{s,tot}$ the shower width over the strips covering 2.5 cells of the second layer;
- $w_{s,3}$ the shower width over three strips around the one with the maximal energy deposit;
- F_{side} energy outside the shower core.

The tracking variables include the number of hits in the pixels, the number of silicon hits (pixels plus SCT) and the tranverse impact parameter. The medium cuts increase the jet rejection by a factor of 3-4 with respect to loose cuts while reducing the identification efficiency by 10%.

Tight This set of cuts makes use of all available information concerning electron candidates. In addition to the medium set, cuts are applied on the number of vertexing-layer hits (to reject electrons from conversions), the number of hits in the TRT, the ratio of high-threshold hits to the number of hits in the TRT (to reject the dominant background from charged hadrons), the difference between the cluster and the extrapolated track positions in eta and phi and to the ratio of cluster energy to track momentum.

An additional energy isolation cut is applied to the cluster, using all cell energies within a cone of $\Delta R < 0.2$ around the electron candidate. This set of cuts gives in general the best isolated electron identification and the best rejection against jets but can be analysis dependent.

In order to measure electron reconstruction efficiency the *tag-and-probe* method can be applied to $Z^0 \rightarrow e^+e^-$ events. The tag electron is a reconstructed electron selected using tight cuts and also required to pass the trigger e15i, that selects events with at least one isolated electron with $p_T > 15\ GeV/c$. The tag electron is also required to be outside the barrel/end-cap transition region ($1.37 < \eta < 1.52$). The probe electron is pre-selected by identifying a cluster in

the opposite hemisphere and the invariant mass of the lepton pair is required to be in a window of $10\ GeV$ around the Z^0 mass peak. Only electrons with $p_T > 15\ GeV$ are used. Figure 2.7 compares the efficiency of reconstruction for Monte Carlo truth matching and the tag and probe method [24].

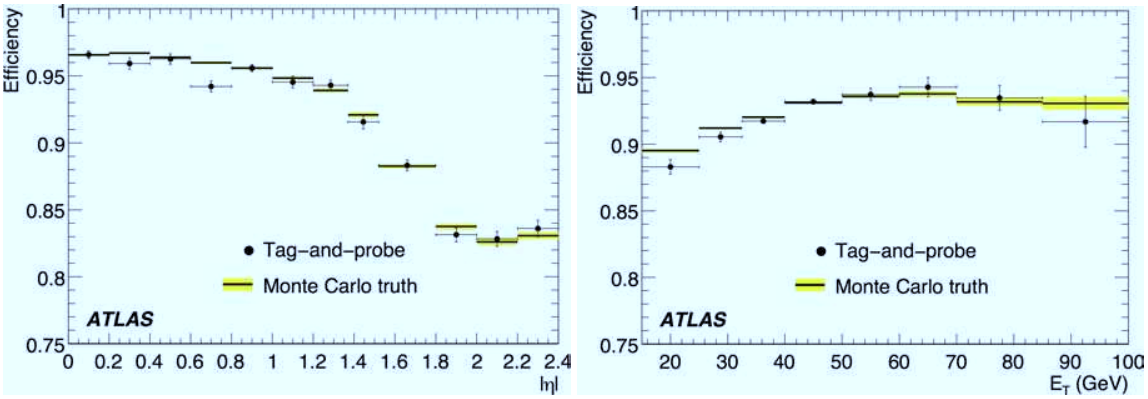

Figure 2.7: Efficiency of the electron pre-selection as a function of η (left) and E_T (right) for $Z^0 \rightarrow e^+e^-$ decays, using the tag-and-probe method and the Monte Carlo truth information.

A number of uncertainties may affect these tag-and-probe measurements once the accumulated data will provide high enough statistics to perform measurements similar to the ones quoted above, *i.e.* [24]:

- The difference in efficiency between MC matching and tag-and-probe is mainly due to the matching ΔR angle. This effect is estimated to be $< 0.1\%$;

- The size of the available Z boson sample is a source of systematic error. With an integrated luminosity of $100\ pb^{-1}$, the error is expected to be in the range $1 - 2\%$ for $p_T > 25\ GeV$, and $\sim 4\%$ in the low-p_T bin;

- The cut on the reconstructed invariant mass introduces another systematic error estimated to be 0.5% for $p_T > 40\ GeV/c$ and $< 2\%$ for low p_T bin;

- The cut on electron isolation gives rise to a systematic error of 1%.

2.4 Identification of Muons

The ATLAS outer muon spectrometer is designed to detect and measure the momentum of muons with a precision on $2-3\%$ at $10-100$ GeV and 10% at 1TeV. Tracking is done using 1150 stations of *Monitored Drift Tubes* (MDT) for pseudorapidity $|\eta| < 2$ and 32 *Cathode Strip Chambers* for $2 < |\eta| < 2.7$. A well-reconstructed muon usually crosses three tracking chambers. Muon triggers (figure 2.8) are given by 606 *Resistive Plate Chambers* (RPC) in the barrel region and 3588 *Thin Gap Chambers* (TGC) in the end-caps, allowing the system to match tracks found in the muon spectrometer (MS) to the ones measured in the inner detector (ID). In fact, RPC and TCG provide a second coordinate along the wire axis that is used to match tracks. In ATLAS, two main algorithms are used for reconstruction: MuID and STACO. Muon identification is performed in three complementary ways:

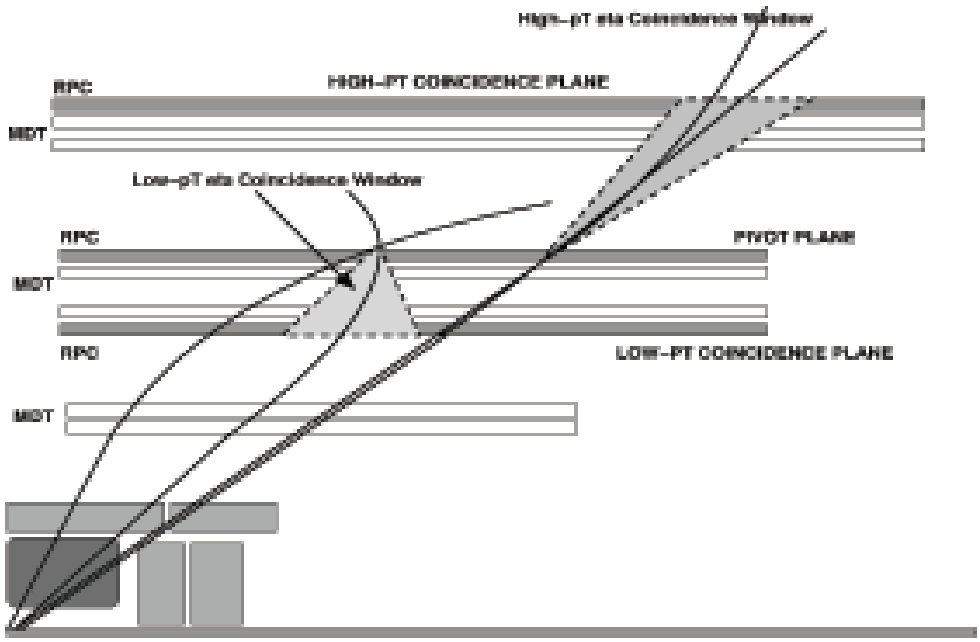

Figure 2.8: Muon trigger system in the barrel region.

Standalone A muon is found in the spectrometer. Standalone track reconstruction starts with a search for patterns among hits in the three stations

of the MS that yield *track segments*. Two families of reconstruction algorithms are present in Atlas, STACO and Muid. The STACO family is implemented by the *Muonboy* algorithm, that finds the spectrometer tracks and extrapolates them to the beam line. It assigns energy loss based on the material crossed in the calorimeter. On the Muid side, the *MOORE* algorithm finds the tracks and performs the inward extrapolation. Additionally, it makes use of the calorimeter energy measurements if they are significantly larger than the most likely value and the muon appears to be isolated [47]. Standalone algorithms have a slightly broader η coverage ($|\eta| < 2.7$) than the inner detector ($|\eta| < 2.5$), but there are holes around $\eta = 0$ and 1.2. Muons produced in the calorimeter, *e.g.* from the decay of B hadrons, are likely to be found in the standalone reconstruction and represent a background for most physics analyses.

Combined A muon found in the spectrometer is matched to one track in the inner detector. The match χ^2 is defined as the difference between outer and inner track vectors weighted by their combined covariance matrix:

$$\chi^2 = (\vec{T}_{MS} - \vec{T}_{ID})^T (C_{ID} - C_{MS})^{-1} (\vec{T}_{MS} - \vec{T}_{ID}) \tag{2.5}$$

Where $\vec{T}$ is a vector of five track parameters expressed at the point of closest approach to the beam line, and C is its covariance matrix.

STACO algorithms performs a statistical combination of track vectors and covariance matrices from the Muonboy tracks extrapolated at vertex and inner detector tracks. The combined track vector is given by:

$$\vec{T} = (C_{ID}^{-1} - C_{MS}^{-1})^{-1} (C_{ID}^{-1} T_{ID} + C_{MS}^{-1} T_{MS}) \tag{2.6}$$

MuID standalone tracks require a global re-fit, using hits from both the ID and the MS. It starts from the inner track vector T_{ID} and covariance matrix C_{ID} and adds the measurements from the outer track. The fit accounts for the material (multiple scattering and energy loss) and magnetic field in the calorimeter and muon spectrometer.

Tagging Inner detector muon track candidates are matched to calorimetric and/or MS informations. This technique proved to be less sensitive to

Coulomb scattering and energy loss: it is very useful to recover low-energy muons in areas with poor muon spectrometer coverage, especially around $|\eta| \sim 0$. *CaloMuonTag* and *CaloMuonLH* are the algorithms that look into the calorimetric layers for energy deposits compatible with minimum-ionizing patterns of muons to tag ID tracks. The MS tagging algorithms, MuTag [24] (STACO family) and MuGirl [55] (Muid family), propagate all inner detector tracks with sufficient momentum out to the first station of the muon spectrometer and search for nearby segments.

MuTag defines a tag χ^2 using the difference between any nearby segment and its prediction from the extrapolated track. It only makes use of inner-detector tracks and muon-spectrometer segments not used by STACO algorithm.

MuGirl uses an artificial neural network to define a discriminant. In either case, if a segment is sufficiently close to the predicted track position, then the inner detector track is tagged as corresponding to a muon. It considers all inner-detector tracks and redoes segment finding in the region around the track and attempts to find all muons, while MuTag is a complement to STACO.

Some other definitions are commonly used to refer to a muon:

- A muon is *best-match* if its combined track is the best match to a muon spectrometer track. Indeed, because of high track multiplicity in Inner Detector, there may be many combined tracks for one given muon spectrometer track. In those cases where a standalone muon is combined with more than one inner-detector track, exactly one of the muons is flagged as *best match*. In the STACO collection, the tagged and combined muons do not overlap by construction. In the Muid collection, overlaps between MuGirl and Muid muons are removed by creating a single muon when both have the same inner detector track.

- Muons are called *low-p_T* if their transverse momentum is less than $20\,GeV/c$. It must have been reconstructed by at least one of these algorithms: MuTag, MuTagIMO, MuGirl, MuGirlLowBeta. High-p_T muon triggers operates only in presence of a low-p_T muon trigger, too;

- Muons are called *high-p_T* if their transverse momentum exceeds $20\,GeV/c$. It must have been reconstructed by at least one algorithm among Muonboy, STACO, MOORE, or other algorithms of the Muid family.
- A best-match high-p_T muon with an associated track in the ID is called *combined*;
- A low-p_T muon with a matched track in the ID which is *not* the best match is called *low-p_T reconstructed* muon

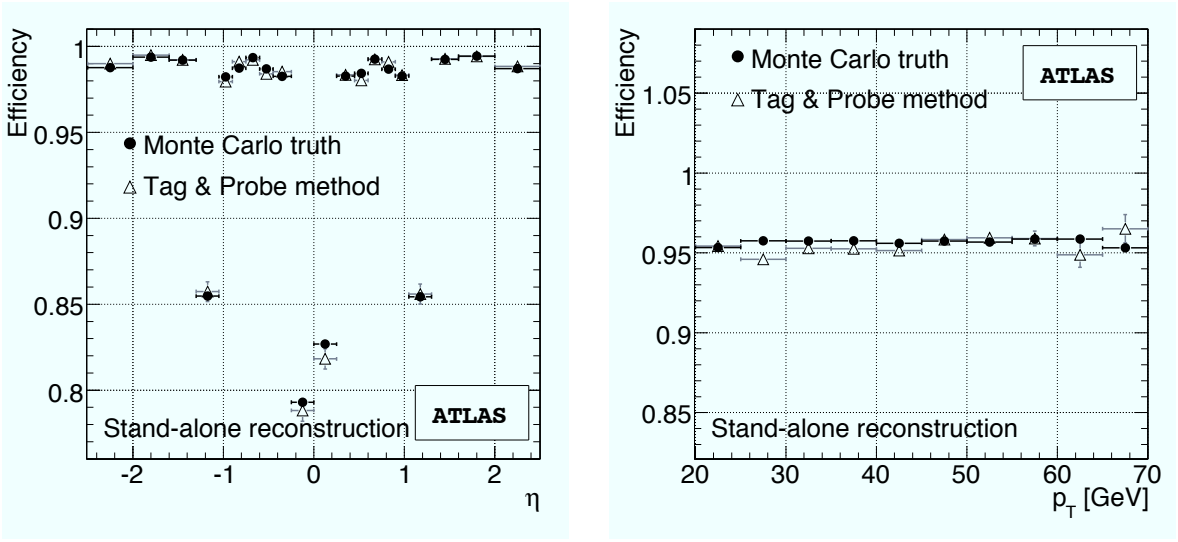

Figure 2.9: Reconstruction efficiency for muons *w.r.t.* MC as a function of η and p_T.

The performance of the muon spectrometer is characterized in terms of efficiency and momentum resolution. Figure 2.9 shows reconstruction efficiency as a function η (left) and p_T. In order to estimate these quantities, the "true" Monte Carlo generated muon and the reconstructed one are matched using their distance in the (η, ϕ) plane:

$$\Delta R = \sqrt{(\phi_{rec} - \phi_{MC})^2 + (\eta_{rec} - \eta_{MC})^2} \tag{2.7}$$

More that 99.7% of muons with $p_T > 50\ GeV/c$ are reconstructed within $\Delta R < 0.05$ (figure 2.10). The muon reconstruction efficiency is thus the fraction of generated muons that can be matched to a reconstructed muon within $\Delta R < 0.05$.

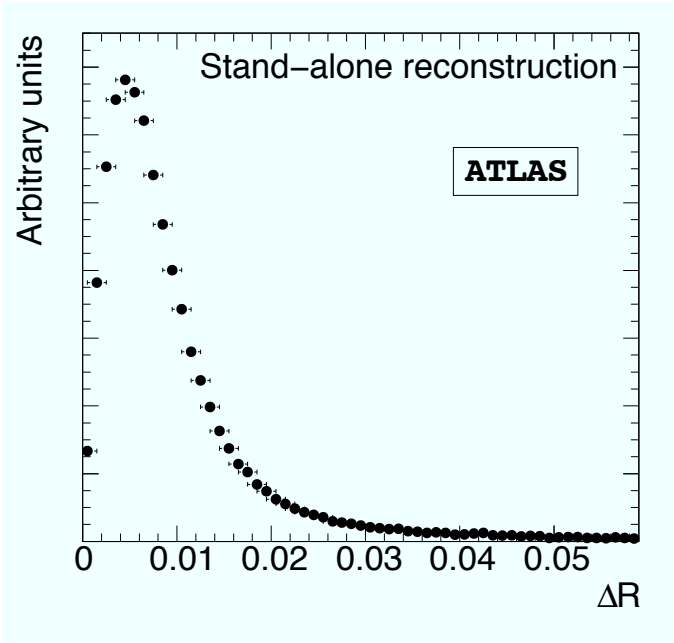

Figure 2.10: Distribution of distance ΔR between the generated and the reconstructed muons in a 50 GeV single muon Monte Carlo sample.

The momentum resolution is measured by comparing the deviation of the reconstructed inverse transverse momentum from the generated inverse transverse momentum:

$$\rho = \frac{1/p_T^{(MC)} - 1/p_T^{(reco)}}{1/p_T^{(MC)}} \tag{2.8}$$

The muon momentum resolution will be affected by the non uniformity of the magnetic field, the uncertainty in the energy loss of the muons, and the alignment of the muon spectrometer. This leads to non-Gaussian tails in the ρ distribution when integrated over η and ϕ, as illustrated for example in Figure 2.11 for a sample of muons of $p_T = 50\, GeV/c$. In order to minimize the effect of tails, the momentum resolution is determined in the following way: in the first step, a Gaussian g_0 is fitted to the distribution. In the next step i a Gaussian g_i is fitted to the data between the $\langle\rho\rangle_{i-1} \pm 2\sigma_{i-1}$, where σ_{i-1} is the fitted width of the gaussian g_{i-1} and $\langle\rho\rangle_{i-1}$ is the fitted mean. The process is iterated until the fit relative change of the fit parameters from one to the next iteration is less than 0.1%. The standard deviation of the final fit curve is taken as a measure for the momentum resolution. The mean of final fit is referred to as the momentum scale, which is a measure for systematic shifts of measured muon momenta

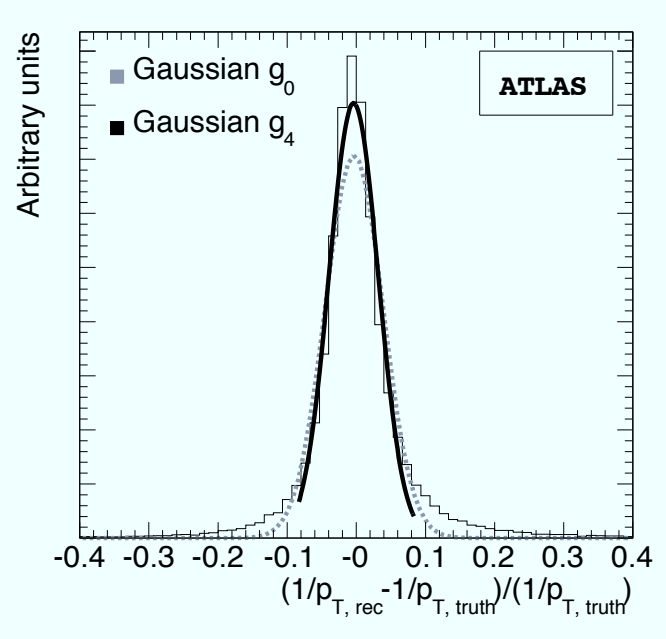

Figure 2.11: Muon momentum resolution.

with respect to the correct values.

Muons with energies below 100 GeV lose on average about 3 GeV of their energy on their passage through the calorimeters almost independently of their energy. A 5% uncertainty in the amount of the material traversed by the muons would reflect in a 5% uncertainty of the energy loss, that is an uncertainty of the average energy loss of $\pm 150\ MeV$.

The stand-alone momentum resolution varies with their transverse momentum. The momentum resolution in the barrel is dominated by fluctuations of the energy loss in the calorimeters for $p_T < 10\ GeV$ where it is about 5% at $p_T \sim 6\ GeV$. It is best, 2.6% (4%) in the barrel (endcap), for $p_T \sim 50\ GeV$ where it is dominated by multiple scattering in the muon spectrometer. The momentum resolution at high momenta is limited by the spatial resolution and the alignment of the precision chambers and approaches 10% at $p_T \sim 1\ TeV$.

2.5 Jet finder algoritms in Atlas

Jet reconstruction hinges on the performances of the calorimeter system, which has been described in section 2.1. It is worth mentioning here that the read-

out is highly granular for the electromagnetic calorimeter, with a cell size of $\Delta\eta \times \Delta\phi = 0.025 \times 0.025$. The hadronic calorimeter is coarser, with typical granularity of $\Delta\eta \times \Delta\phi = 0.1 \times 0.1$.

Calorimeter cells, once suitably grouped (see section 2.5.1 for a description of *Towers* or in *TopoClusters*), provide input for the jet reconstruction algorithm. Jet finding algorithms expects four momenta on input. Thus, the group of cells are given in a massless pseudo-particle representation $(E, \vec{p})$, where E is the measured energy and the momentum $\vec{p}$ points along the axis of the cluster. Obviously, every combination of grouping criteria and jet algorithm gives rise to different efficiencies. In order to measure these effects, several jet finders are under test in Atlas, which belong to the two main families of *cones* and *clustering* algorithms, already described in section 1.3.2.

2.5.1 Calorimeter signals for jet reconstruction

The ATLAS calorimeter has about 200,000 cells of different size and geometry. It is therefore necessary to combine all these information in a coherent way in order to provide a practical input to jet finder algorithm. At present, there are two possibilities called *signal towers* and *topological cell clusters*. Figure 2.12 shows the effect of the same reconstruction algorithm (cone .7) applied to the two classes of input objects.

Signal towers The cells are projected onto a fixed grid in (η, ϕ) space. The tower bin size is $\Delta\eta \times \Delta\phi = 0.1 \times 0.1$ for a grand total of 6,400 towers. Cells whose projection does not fit into a single cell or those whose projection does not fill completely a cell are weighted depending on the overlap fraction with the cell area. Towers are always calibrated at electromagnetic scale only and include *all* calorimeter cells.

Topoclusters are clusters that try to follow the development of showers inside the calorimeter in the three dimensional space. Cells with a signal-to-noise ratio (Γ) greater than 4 are taken as seeds. All neighbours with $\Gamma > 2$ are added to the cluster, as well as neighbours of neighbours, but this time with $\Gamma > 0$. This sequence is often referred to as $4/2/0$. Clusters are always calibrated at electromagnetic scale, and can be calibrated locally

at hadronic scale, too. Differently from signal towers, topological clusters make use only of those cells that pass noise suppression.

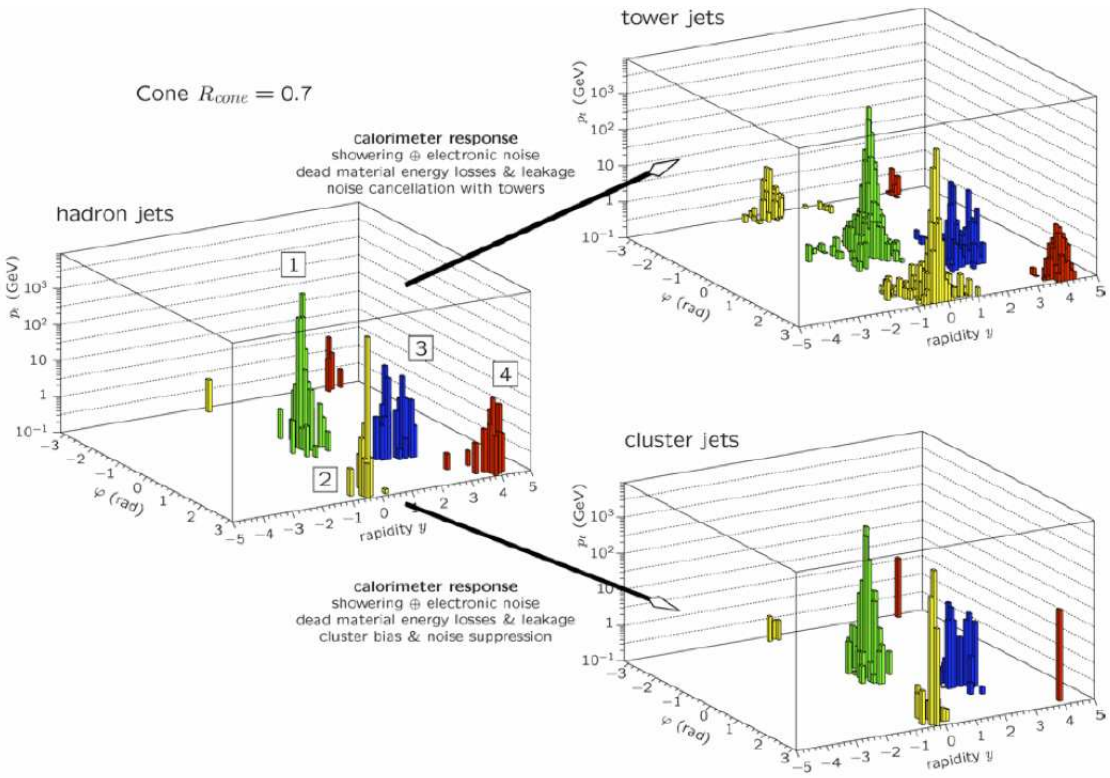

Figure 2.12: Effect of the cone .7 reconstruction algorithm applied to tower jets (up) and topoclusters (down).

The quality of the reconstruction of jets *w.r.t.* E_T and η is shown in figure 2.13. The matching between the reconstructed jets and the truth jets is done considering their separation in (η, ϕ) space, and a jet is matched to a truth jet if $\Delta R < 0.2$. For each bin in energy and pseudorapidity, a histogram is filled with the ratio between the reconstructed energy and the truth energy.

The linearity $(E_T^{truth} - E_T^{reco})/E_T^{truth}$ is observed over a wide energy range, both in the central ($|\eta| < 0.5$) and in the intermediate ($1.5 < |\eta| < 2$) regions. We can observe that for the lowest considered transverse energy bin, the ratio increases with the pseudorapidity. This is a consequence of the fact that energy increases with η at fixed E_T and that the linearity improves with increasing energy [24].

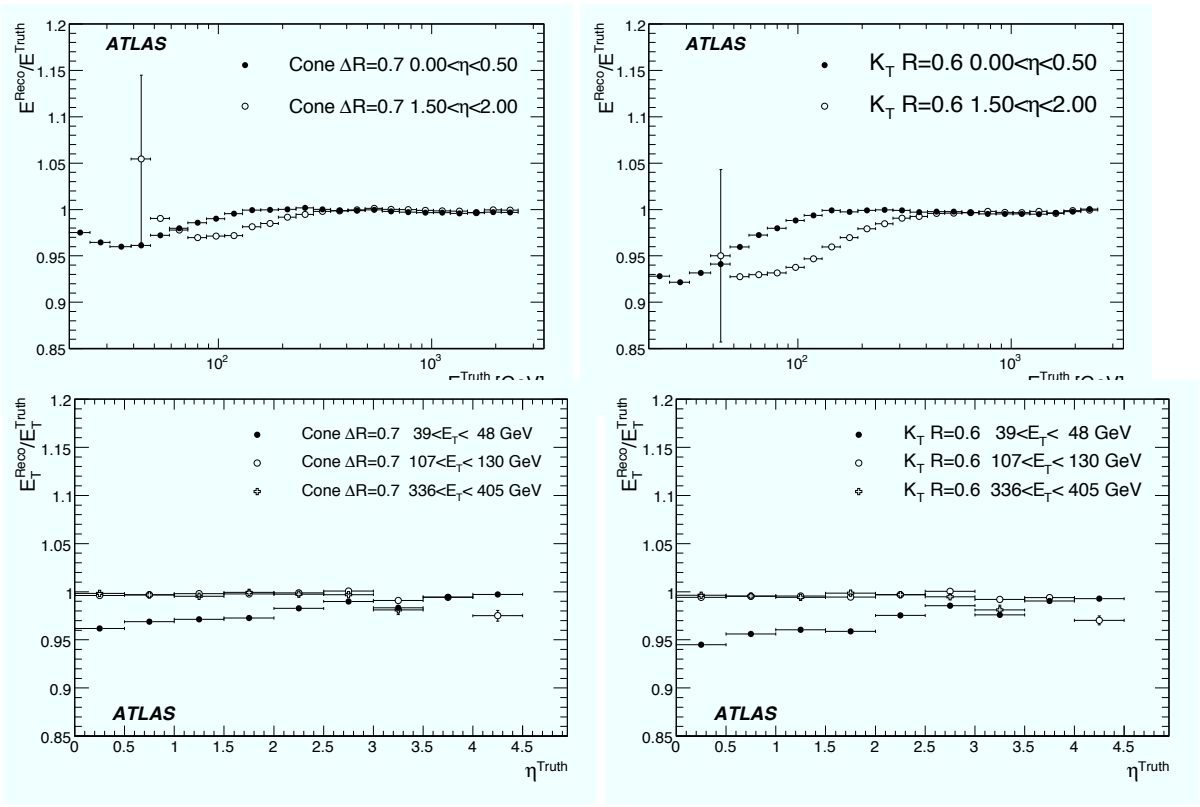

Figure 2.13: Dependence of the ratio E_{rec}/E_{truth} for jets reconstructed with a cone .7 (left) and a k_T .6 algorithm *w.r.t.* E_T and η.

2.5.2 Calibration of Jet Energy

The measured jet energies have to be corrected to take into account detector and physics effects [24].

Instrumental Effects Jet energy determination suffers from effects due to the detector:

- Regions with cracks, dead material and effects on the response uniformity due to the use of different technologies in different regions of pseudorapidity;
- Different response to hadrons and electrons as the ATLAS calorimeter is non-compensating: a jet is a composition of different particles; about 40% of the total energy is carried by charged pions, 20% by kaons, $\sim$10% by protons and neutrons and 25% by photons (mainly from the π_0 decay); about 25% of the energy deposited comes from pure electromagnetic showers; about 2/3 of the reconstructed energy is measured by the electromagnetic calorimeter, and the rest by the hadronic calorimeter - while the calorimeter has been calibrated at the electromagnetic scale;
- Bending out of the jet of low momentum charged particle from the solenoidal magnetic field;
- Multiple pp interactions, important at high luminosities, will add extra energy to the jets;

Physics Effects Initial uncertainty about physical processes must be also taken into account:

- The hadronization of the parent parton and initial and final state radiation will spoil the correlation between the energy of the parton and that of the jet. Depending on the parameter that sets the jet "radius", part of the energy will be lost out of the reconstructed jet;
- Fluctuations on the energy from the spectator partons (*underlying event*) will as well contribute to spoil the correlation. Some jet clustering alogorithm such as AntiKt are less sensitive to this effect than others.

The sum of the energy deposits in the ATLAS calorimeter cells will give the correct response for electrons and photons, as the calibration constants are correct for the electromagnetic scale. There are several levels of "true" jet energies:

- at the **particle** level, where corrections are applied for the non-compensation, non uniformity, crack etc.; position and energy-dependent corrections are then applied to restore the energy of the particles produced by the fragmentation and hadronization processes originating form the parent parton; the corrections are found by matching a reconstructed jet with a corresponding particle jet (the *truth* jet) - found by applying exactly the same jet alghorithm to the stable final state particles (lifetime $\tau \geq 10\,ps$) provided by a Monte Carlo generator;

- at the **parton** level; the corrections going from the particle to the parton level are those mostly sensitive to the uncertainties in the modelization of the hadronization and fragmentation processes.

The calibration scheme to pass from detector to particle jet energies is based on cell energy deposit weighting, that can be applied to both tower and cluster jets. The procedure, known as H1-weighting [30], is based on the fact that low energy densities in cells in a non-compensating calorimeter point to a hadronic signal, therefore needing a weight of the order of the electron/hadron (e/h) ratio. On the other hand, high signal densities are more frequently generated by electromagnetic showers, so that do not need any additional weighting. There is also a jet reconstruction sequence where the input objects to the jet finder are topoclusters already calibrated at the local hadronic scale, so that also the output jets are calibrated at the hadronic scale.

The *in-situ* calibration, based on the p_T balance in events like Z+jet or Z+γ will be used to evaluate the energy that falls out of the jet, and expecially to study the systematic uncertainty on the jet energy scale, based on the Data/Monte Carlo differences.

2.5.3 Overlap removal between electrons, muons and jets

As said in the previous section (2.5.1), jet reconstruction algorithms provide a list of clustered calorimeter cells, thus including both particle jet originated from electrons and the decay of hadrons. Therefore, a procedure must be introduced to remove from this list the clusters that are indeed electrons. This can be done quite easily provided that the efficiency of the electron reconstruction algorithm is high enough. The simplest overlap removal is made cutting on the distance $\Delta R = \sqrt{\Delta\eta^2 + \Delta\phi^2}$. The ΔR of every the electron-jet pair is calculated. If this distance is less than 0.2, the jet candidate is rejected.

A similar procedure is applied to all muon-jet pairs in order to find isolated muons. This time, the rejection affects the muons, assuming that muons with a ΔR less equal than the aperture of the jets (in this case 0.4) are not isolated, but come from the semi-leptonic decay of a meson. By the way, it is assumed that the energy released by the muons in the calorimeter does not give rise to reconstructed jets, so that no overlap removal between jets and muons rejecting the jet is applied.

2.6 Missing Transverse Energy

A very good measurement of missing transverse energy will play an extremely important role in many physics studies in Atlas. In fact, large E_T^{miss} is expected in many BSM theories which predict the existence of neutral massive particles that escape the detector. In $t\bar{t}$ events true E_T^{miss} only comes from neutrinos. Unfortunately, neutral weakly-interacting particles are not the only source of E_T^{miss} : inefficiencies such as limited geometric acceptance of the detector, presence of dead regions, electronic noise in calorimeters and muon system gives rise to missing transverse energy as well. Overall, these sources contribute to what is known as *fake* E_T^{miss} .

The missing transverse energy (E_T^{miss}) is computed from all the calorimeter cells after noise suppression. The noise suppression is applied following two different routes. In the former, all cells with energy $|E| > 2\sigma_{\text{noise}}$ are retained for the calculation. In the latter cluster of cells are formed following this scheme:

- all cells with $|E| > 4\sigma_{\text{noise}}$ are identified as seeds for the clustering;

- all the neighbouring cells of each seed, with $|E| > 2\sigma_{\text{noise}}$ are added to the cluster;

- all the neighbouring cells of the neighbours found in the previous step, with $E > 0$, are added to the cluster.

The clusters found with this algorithm (also known as $4/2/0$ from the thresholds applied for the noise suppression) are called *topoclusters*. The E_T^{miss} computed from the topoclusters performs better than the one computed directly from all the cells [24].

Figure 2.14 shows the distributions of the x- and y-component of the missing transverse energy vector as measured in 2009 LHC run 141755 [15].. Only cells in topological clusters are used (noise suppression using $4/2/0$). No calibration is applied (EM-scale).

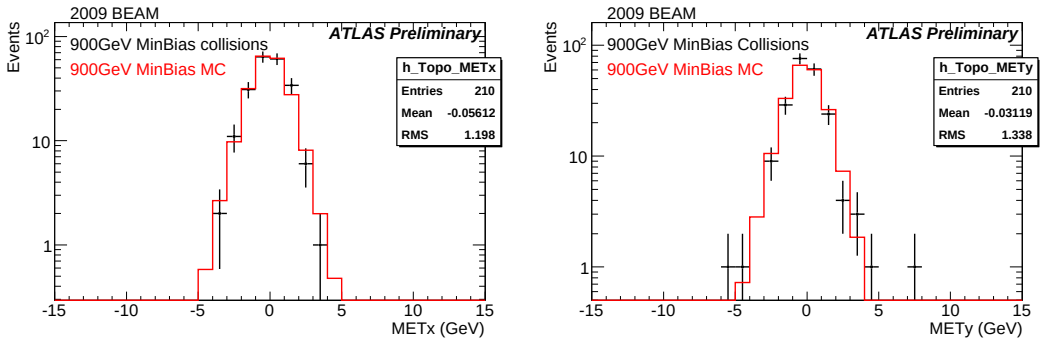

Figure 2.14: Distributions of the x- and y-component of the missing transverse energy vector as measured in 2009 LHC run 141755. Only cells in topological clusters are used (noise suppression using $4/2/0$). No calibration is applied (EM-scale).

Once the topoclusters are found, the missing transverse energy is com-

puted as:

$$\begin{aligned} E_x^{miss} &= -\sum_{i=1}^{N_{cell}} E_i \sin\theta_i cos\phi_i \\ E_y^{miss} &= -\sum_{i=1}^{N_{cell}} E_i \sin\theta_i sin\phi_i \\ E_T^{miss} &= \sqrt{(E_x^{miss})^2 + (E_y^{miss})^2} \end{aligned} \tag{2.9}$$

where the sum runs over all the cells in the topoclusters, and θ_i and ϕ_i are the polar angles of the i_{th} cell.

At this level the calculations are done for energies calibrated (from test beam data) at the electromagnetic scale. To pass to the final E_T^{miss} the calibrations are applied, as well as the corrections for the energy lost in the material of the calorimeter cryostat. Finally, the energy lost by the reconstructed muons is taken into account.

Measurements are collected from transverse energy deposits in the calorimeter, and corrections are applied for energy losses in the cryostat and measured muons:

$$E_{x,y}^{miss\ (final)} = E_{x,y}^{miss\ (Calo)} + E_{x,y}^{miss\ (Cryo)} + E_{x,y}^{miss\ (Muon)} \tag{2.10}$$

Calorimeter E_T^{miss} must be calibrated in order to reduce the systematic shift of its scale and optimize its resolution. Two common calibration schemes are *H1-like* and *Local-hadronic* (LH). In H1 scheme, cells energy is weighted depending on cell energy density E/V (16 bins), pseudorapidity and calorimeter region. Since EM showers are much denser than hadronic ones, high-E cells are weighted according to their EM scale, while low-E cells are weighted with hadronic scale. The weights are calculated from from di-jet samples. In LH scheme, TopoClusters are classified as EM or hadronic. Then, hadronic TopoClusters are scaled using MC Truth information, while EM TopoClusters are left as they are. Out-of-cluster corrections are applied and clusters can be weighted to account for known dead materials. These are local (hence the name of the scheme), and determined using MC Truth info.

The final step of calibration takes into account final-state high-p_T identified objects. Cells are associated to such objects in a chosen order: electrons, photons, muons, hadronically decayed τ-leptons, b-jets and light-jets. The cal-

ibration of each class of object is known to a far better degree of accuracy than the global calibration, so that the E_T^{miss} reconstruction is highly enhanced. The cryostat correction is non-negligible for high-p_T jets, and contributes at the level of 5% for jets with $p_T > 500\,GeV$.

As for the muon term, only good-quality reconstructed muons are taken into account: The matching requirement reduces the contribution from fake muons that arise, for instance, in events with very high energetic jets. Unfortunately, the coverage of the muon spectrometer is limited, but muons reconstructed from tracks in the inner detector and energy deposits in the calorimeter can be used to recover these events. The muon term affects only slightly the E_T^{miss} measurement, but fake or badly reconstructed muons are anyway a large source of fake E_T^{miss} .

A refinement of E_T^{miss} is then computed based on the physics objects that are reconstructed in the event and the topoclusters that are not used. Each reconstructed object (μ,e,τ,γ,jet,b-jet, etc.) is mapped on the calorimeter cells that belong to it. The overlap removal is done at the cell level and the different contributions are added with cell-calibration weights which depend on the object. The contribution of cells not associated to any topocluster is also added to compute the final E_T^{miss}. This E_T^{miss} is the one that we will use from now on.

Some analyses, such as $h \to \tau\tau$, are very sensitive to low-p_T deposits coming for instance from pions, soft jets, underlying event and pile-up. Object-based method classifies objects into $high-$ and $low-p_T$ objects. Object-based reconstruction hinges on calorimeter performances, and makes use of the tracker for the determination of low-p_T deposits. All topo-cells not belonging to high-p_T identified objects are associated to low-p_T final state particles, and a jet reconstruction algorithm with small radius ($R_{cone} = 0.2$) is applied to reconstruct so-called *mini-jets*, which are basically pions.

The resolution of E_T^{miss} is evaluated from the width of the $E_T^{miss}\ {}^{(truth)}_{(x,y)} - E_T^{miss}\ (x,y)^{(reco)}$ distributions in bins of the total transverse energy deposited in the calorimeters ($\sum E_T$). The resulting resolution, shown in figure 2.15, is fitted with a function $\sigma = a\sqrt{\sum E_T}$. The solid curve corresponds to a combined fit in the low- and high-$\sum E_T$ regions, and the best-fit gives a value for the parameter $a = 0.55$ [24]. There is a degradation in the performance for the

high p_T jet samples (J6 and J7), where the constant term in the calorimeter resolution dominates. Figure 2.16 shows the resolution of the two components of the missing transverse energy as a function of the total sum of the transverse energy at centre-of-mass energy of $\sqrt(s) = 2.36\ TeV$. Overlayed earlier approved data at $\sqrt(s) = 900\ GeV$ and a fit to the Monte Carlo simulation [15]. Only cells in topological clusters are used (noise suppression using $4/2/0$). ATLAS 2009 collision data: Minimum bias triggers. Run 142308, LB 296-389 no calibration is applied (uncorrected electromagnetic scale = EM scale).

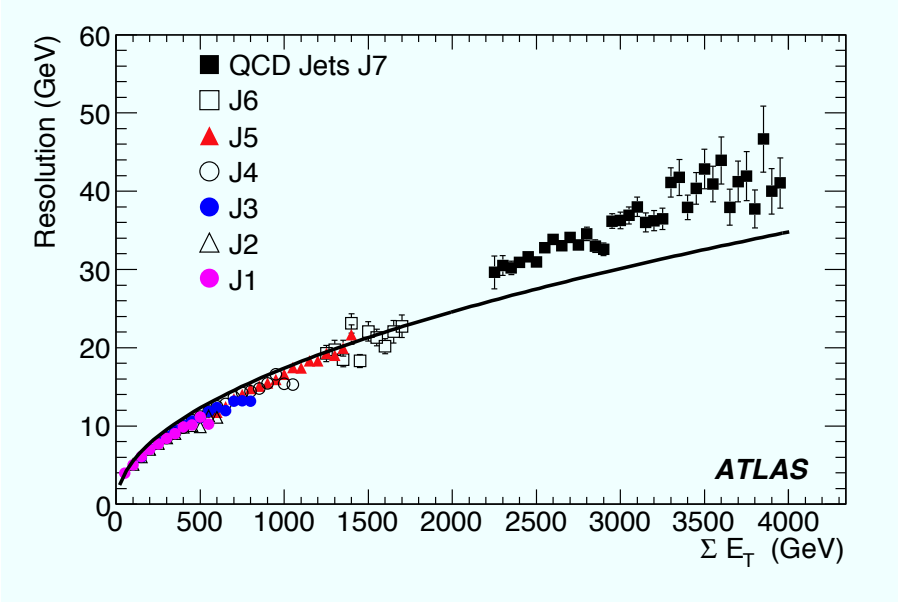

Figure 2.15: Resolution of E_T^{miss} as a function of $\sum E_T$ for QCD di-jet samples, overimposed with the best-fit function $\sigma = 0.55\sqrt{\sum E_T}$. The whole QCD di-jet sample is split into six sub-samples (J1-J6) divided in disjoint ranges of the PYTHIA parameter $\hat{p}_T$ [54] in order to enhance the Monte Carlo event generation efficiency.

2.6.0.1 Fake Missing Transverse Energy

Fake missing transverse energy has two main sources: muon and calorimetric mis-measurements. E_T^{miss} from muons can be caused either by inefficiencies in reconstructing a high p_T muon or by reconstructing a fake high p_T muon. For reasonable muon reconstruction efficiencies, E_T^{miss} from missed muons represents only a small fraction of the True E_T^{miss} from neutrinos. However, fake E_T^{miss} from muons is dominated by missed muons rather than fake muon. Figure 2.17 shows the η distribution of the true muons that were missed at the re-

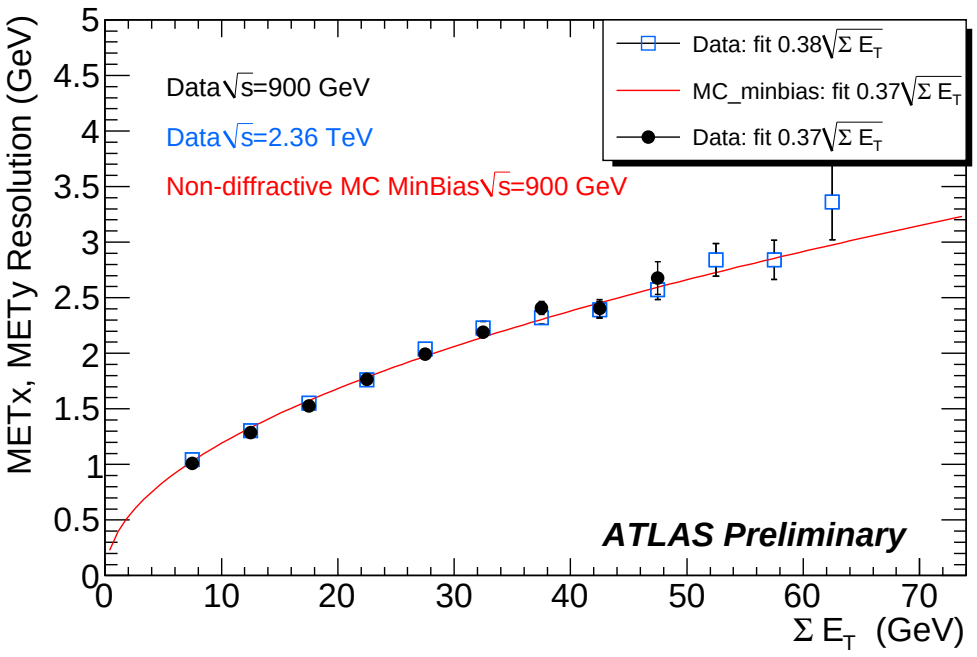

Figure 2.16: Resolution of the two components of the missing transverse energy as a function of the total sum of the transverse energy at centre-of-mass energy of $\sqrt{(s)} = 2.36\ TeV$. Overlayed earlier approved data at $\sqrt{(s)} = 900\ GeV$ and a fit to the Monte Carlo simulation.

construction level in a $Z^0 \rightarrow \mu\mu$ sample with $p_T > 100\,GeV$. Missed muons are present in η ranges for which there is no coverage of the spectrometer (around $\eta = 0$, where the service hole is located, and for $|\eta| > 2.7$).

The calorimeter has cracks and gaps in the transition regions, which are also used for service outlets. These regions have poorer resolution and are expected to have larger contributions to fake E_T^{miss} compared to the rest of the calorimeter. There are two gap regions defined in the following η ranges: $(1.3 < |\eta| < 1.6)$ and $(3.1 < |\eta| < 3.3)$. A large number of the worst measured jets have η in $1.3 - 1.6$. The pseudorapidity of the second worst measured jet is more flat and peaks around $0.6 - 0.9$, the transition region of the barrel tile calorimeter to the extended barrel tile calorimeter. However, events with a high-p_T jet in the crack do not show a higher level of fake E_T^{miss} than events with no jet in the crack: this can be explained considering that an event has usually several particle jets, and not all the worst measured jets are indeed in the crack. Overall, this effect is smoothed out and the pseudorapidity of jets is not an important discriminant to reduce fake E_T^{miss} .

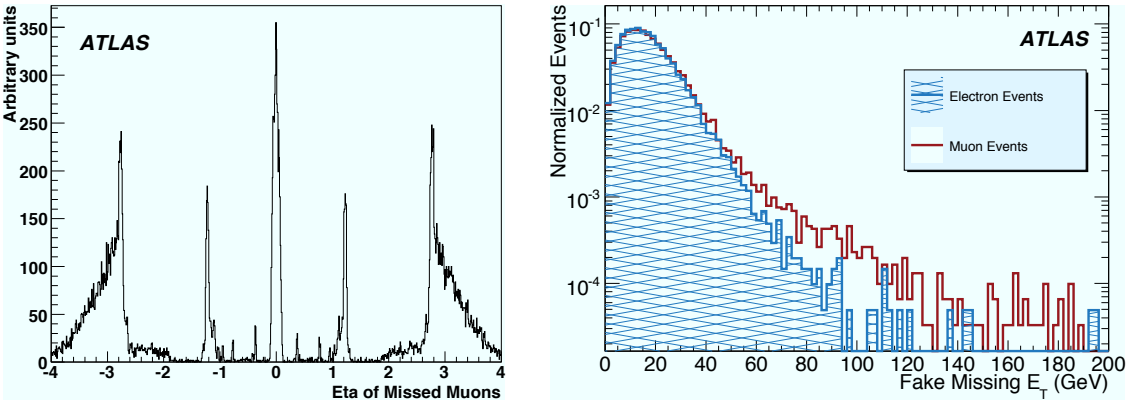

Figure 2.17: The η distribution of true muons that were missed during reconstruction in a $Z^0 \rightarrow \mu\mu$ high $p_T > 100\,GeV$ sample (right). On the right, fake E_T^{miss} in $t\bar{t}$ events in the electron (hatched) and muon channel.

2.7 Tag and Probe for Muons

Top quark decays can provide an interesting environment for the evaluation of leptonic triggers the *tag-and-probe* method. Usually, one can measure the trigger efficiency with respect to offline reconstruction *e.g.* in $Z^0 \to \mu\mu$ events (see figure 2.18), doing as follows on an event-per-event basis:

1. Process the event only if the trigger chain under study has fired;
2. Decide whether there are at least two "good" offline muons whose invariant mass is close to the Z boson mass (within a window of $10\ GeV$);
3. "Tag" one muon if it fired the trigger, store informations about the other one ("probe" muon), like its transverse momentum, pseudorapidity and azimuthal angle.

At the end of the process, one would like to study the trigger efficiency *w.r.t.* offline muons for each measured quantity. The method can be applied to each reconstruction algorithm and can be used estimate their single efficiency, and perform a comparison among each other. In the following, the method will be applied only to STACO muons, reconstructed with the Muonboy algorithm (see sec. 2.4). Standard $Z^0 \to \mu\mu$ event selection is highly efficient, yielding a small number of background events:

- Two muons with $p_T > 6\ GeV/c$ and $|\eta| < 2.7$
- $|m(\mu_1 + \mu_2) - m_Z| \leq 10\ GeV$

As can be seen in figure 2.19, $Z^0 \to \mu\mu$ events generated with Pythia and selected with such requests are almost background-free, so one can collect a very pure sample of isolated leptons.

The same is not true for the $t\bar{t}$ dileptonic decay, where the background can be tamed but not eliminated completely. In order to apply the tag-and-probe to $t\bar{t}$ di-leptonic events, some selection criteria must be determined. Di-leptonic events have in their final state two charged leptons, two neutrinos giving rise to missing transverse energy, and at least two particle jets, of which two are certainly originated from b quarks. The following cuts have been applied, based on standard di-leptonic search [24]:

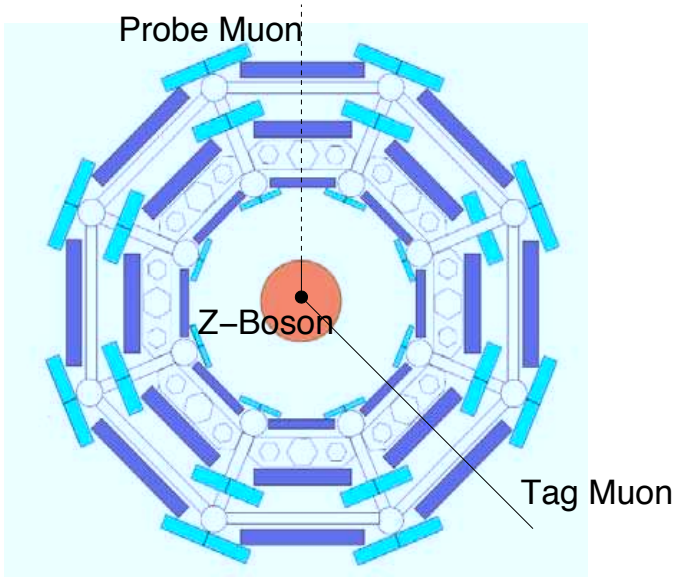

Figure 2.18: Pictorial view of the tag and probe method applied to $Z^0 \rightarrow \mu\mu$ decays.

- Two muons with $p_T > 6\ GeV/c$ and $|\eta| < 2.7$
- $|m(\mu_1 + \mu_2) - m_Z| \geq 10\ GeV$
- $E_T^{miss} \geq 30\ GeV$
- At least two jets with $p_T > 20\ GeV/c$ and $|\eta| < 2.5$

The request on the invariant mass of the two muons is deployed in order to avoid $Z^0 \rightarrow \mu\mu$ events with many radiated particle jets and large missing transverse energy originated from a badly reconstructed event (*e.g.* when a hard jet hits the crack).

It must be stressed that in a real-life situation, one would like to shift the threshold on muon p_T to a safer level on the plateau region, *e.g.* above $20\ GeV/c$ for mu20 trigger. However, this tighter request is dropped at this level in order to measure the efficiency and contamination *w.r.t.* offline muons. Two muon trigger chains have been tested: mu10 and mu20, the former having a larger acceptance for low-p_T muons (see again fig. **??**), while the latter is expected to yield a neater signal. In fact, mu10 chain has a rate of $21.8\ Hz$ with no prescale at low luminosity, and will be very important for studies on B physics, W/Z and τ decays as well. mu20 will have a rate of $1.5\ Hz$ and, at least at the

beginning, is considered a back-up for mu10 and will not be prescaled event at higher luminosity.

Taking a look at the transverse momentum distribution of muons coming from Z^0 boson decays (Fig **??**, on the left), one can see that those events are very useful to study triggers for muons with p_T in range $30 - 50\ GeV/c$. In order to increase the statistics for low-p_T muons, one can exploit J/ψ and Υ mesons decaying to muon pairs. However, Z^0 events are easy to select and, thanks to the almost hard-jets-free environment, most of the muon are reconstructed extremely well. Anyway, it is still interesting to know whether leptonic trigger efficiencies are really the same for much more complex events such as $t\bar{t}$ decays.

2.7.1 Classification of probe muons

The higher particle jet multiplicity could worsen lepton isolation. As a consequence, the lowering of the number of clearly reconstructed final state leptons can lead to a lower trigger efficiency. It must be taken into account that not all the muons are perfectly reconstructed anyway.

We classifiy *Probe* muons according to the goodness of their reconstruction, as follows:

Golden A *combined* muon that fired the trigger (*tag*);

Silver A *combined* muon that did non fire the trigger (*combined*);

Bronze A muon whose extrapolated track matches an ID track compatible with a muon (*ID trk*);

Copper An standalone (MS-only) muon (*standalone*);

Wooden A muon identified in the ID+Calorimeter but not in the MS (*ID+Calo*).

Reconstructed muons are associated to trigger muons using the ATLAS standard tool `trigMatchTool`. Using this tool, one can find the closest object within $\Delta R < 0.1$ that matches the trigger muon.

In an ideal setup, one would like to use *golden* muons only, or at worst *golden* and *silver* muons. It is possible to estimate how many low-quality muons

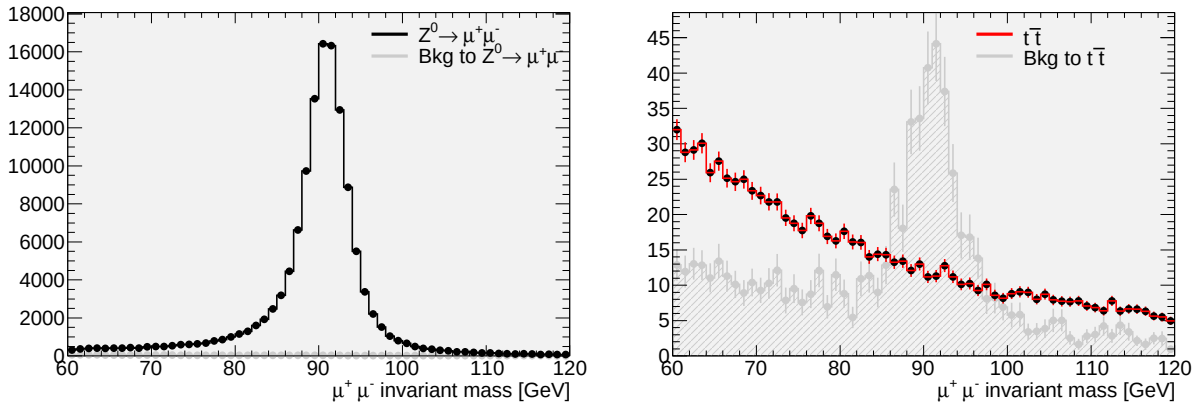

Figure 2.19: $\mu^+\mu^-$ invariant masses for $Z^0 \to \mu\mu$ (left) and di-leptonic $t\bar{t}$ (right) events after event selection, except Z mass window cut.

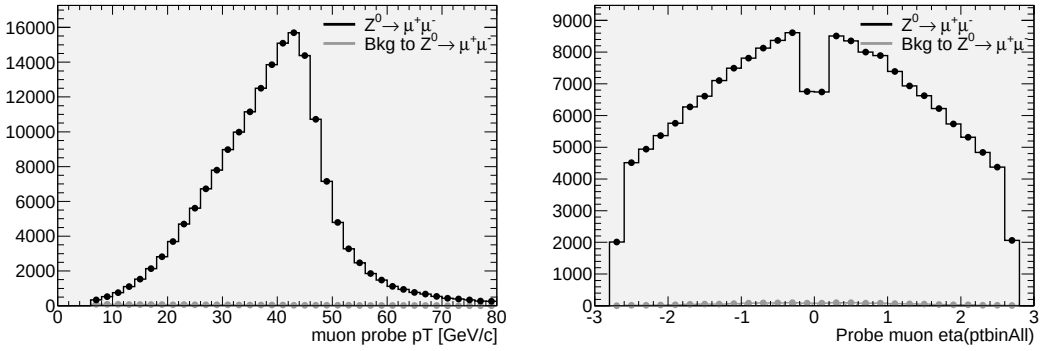

(a) $Z^0 \to \mu\mu$ events

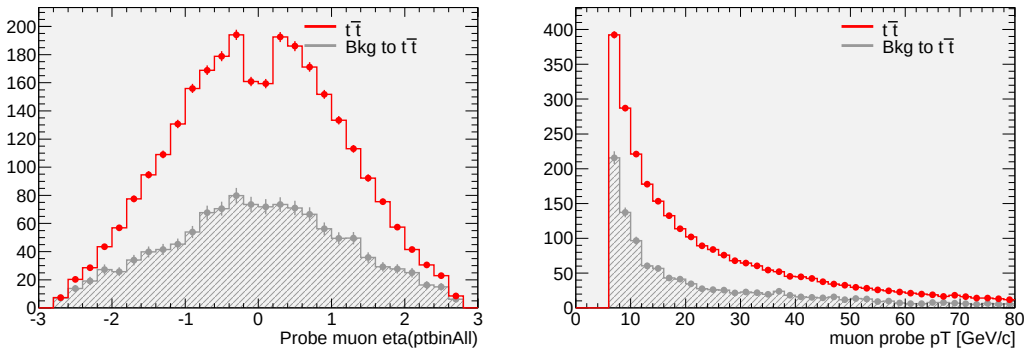

(b) $t\bar{t}$ events

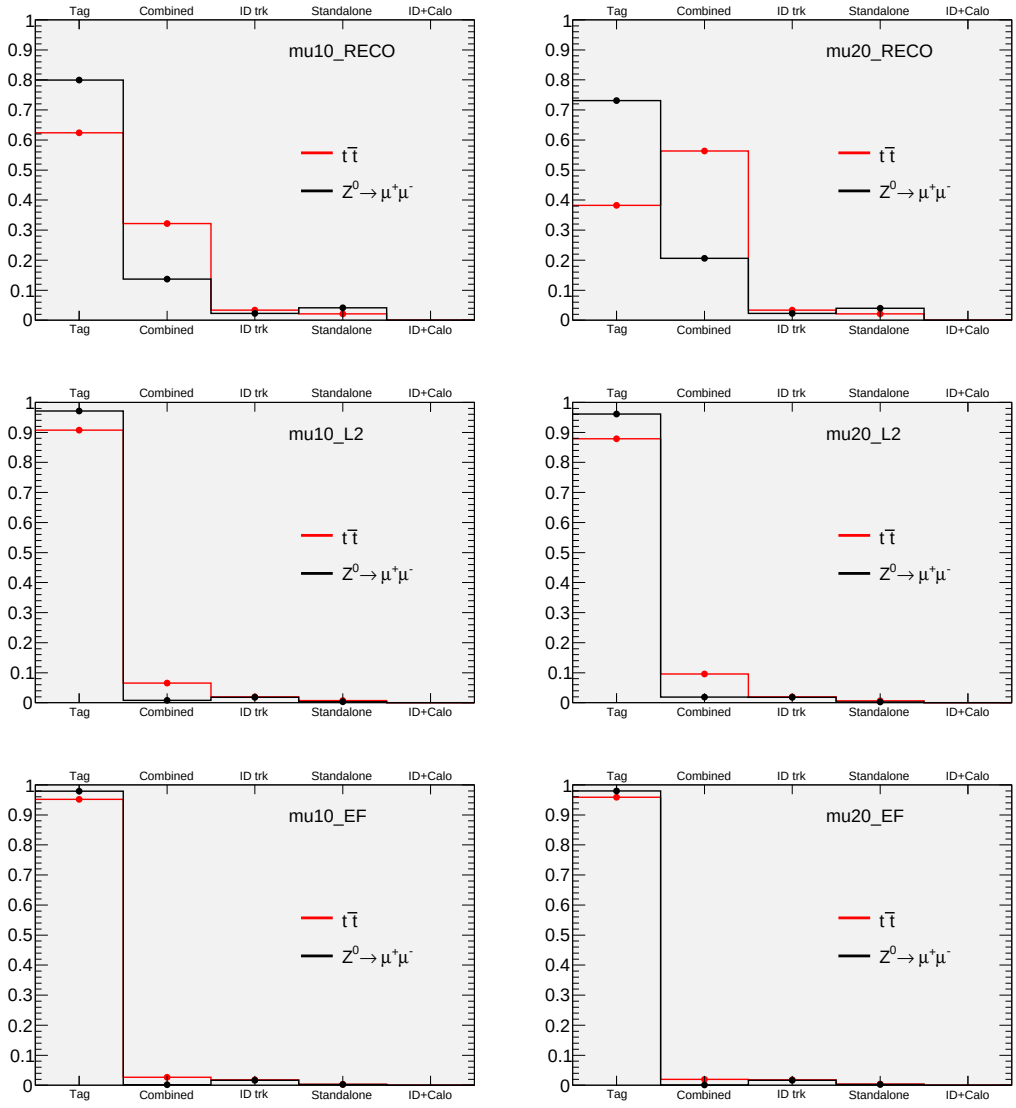

Figure 2.20: Probe muon classification after event selection: mu10 (left) and mu20 (right) trigger chains at offline (top), L2 (middle) and EF (bottom) level.

are present in $t\bar{t}$ events and how their rejection affects the measurement of physically interesting quantities using Monte Carlo simulations.

As shown in figure 2.20, in $Z^0 \rightarrow \mu\mu$ events most of probe muons are good enough to be tag muons, too. Basically, this means that 75% of the events are able to fire not only a single muon, but even a di-muon trigger. The situation is a bit different for $t\bar{t}$ events. In fact, almost 30% of the reconstructed muons are combined, but did not fire mu10 trigger. For mu20 trigger, it can be seen that *most* of the reconstructed muons ($\sim 55\%$) are combined but did not fire the trigger. Anyway, at L2 it is evident that the contamination is lower and it is eventually very small at the EF. This is due to the presence of a larger number of low-p_T muons in $t\bar{t}$ events than in $Z^0 \rightarrow \mu\mu$ events. Figure 2.21 shows the p_T distributions of combined (*silver*) probe muons. It is clear that setting the thresholds at $20\ GeV/c$ this type of muons practically vanishes for $t\bar{t}$ sample, *i.e.* moving the p_T threshold towards the plateau region the two distributions are much more similar for mu20 trigger chain.

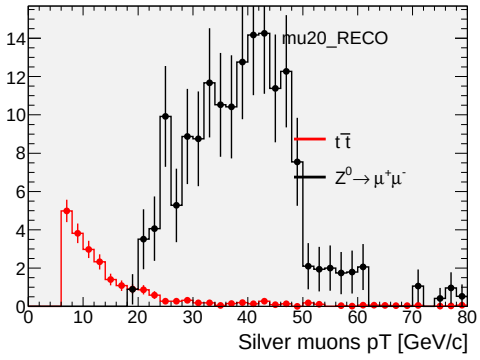

Figure 2.21: Silver probe muons transverse momentum.

2.7.2 Trigger efficiency as a function of p_T

Figures 2.22 and 2.23 show the evolution in efficiency for for the two samples from L1 to EF for mu10 (left) and mu20 (right) trigger chains. As can be seen, a sizeable variation is present for both in the low-p_T region, where some contamination is still present at L2 (green area) but is kept very low after the

event filter is applied. The plateau is reached for a muon p_T greater than about $30\ GeV/c$. A comparison of the two efficiencies at L2 (top) and EF (bottom) is shown in figure 2.24 for mu10 (left) and mu20 (right) trigger chains. The two samples behave quite in a similar fashion, but $t\bar{t}$ events present a slightly higher efficiency throughout the transverse momentum spectrum.

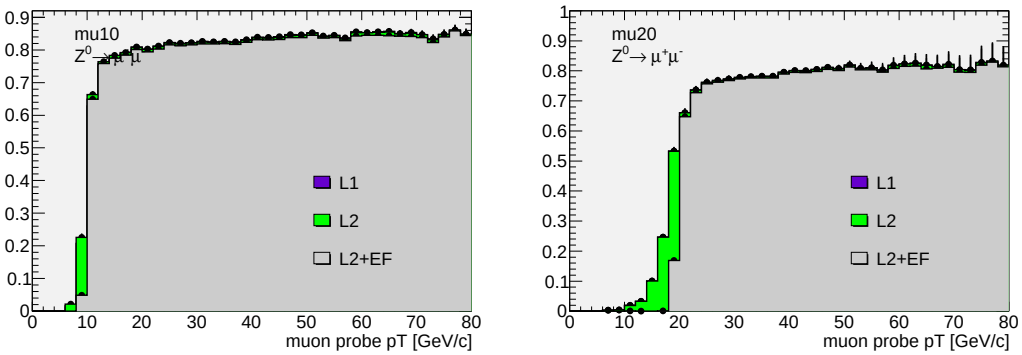

Figure 2.22: Trigger efficiency as a function of transverse momentum: changes from L1 to EF level for mu10 (top) and mu20 (bottom) for $Z^0 \rightarrow \mu\mu$ sample.

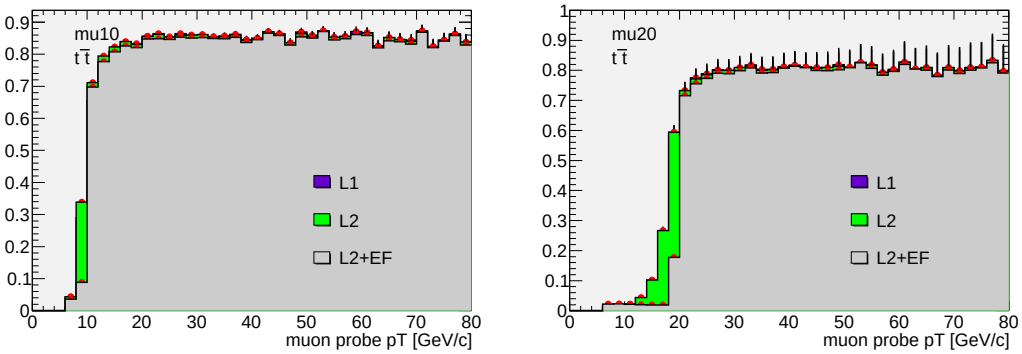

Figure 2.23: Trigger efficiency as a function of transverse momentum: changes from L1 to EF level for mu10 (top) and mu20 (bottom) for $t\bar{t}$ (right) sample.

2.7.3 Trigger efficiency as a function of η

Efficiency in pseudorapidity is shown in figure 2.25. The difference arises from the different average p_T of muons for the two samples.

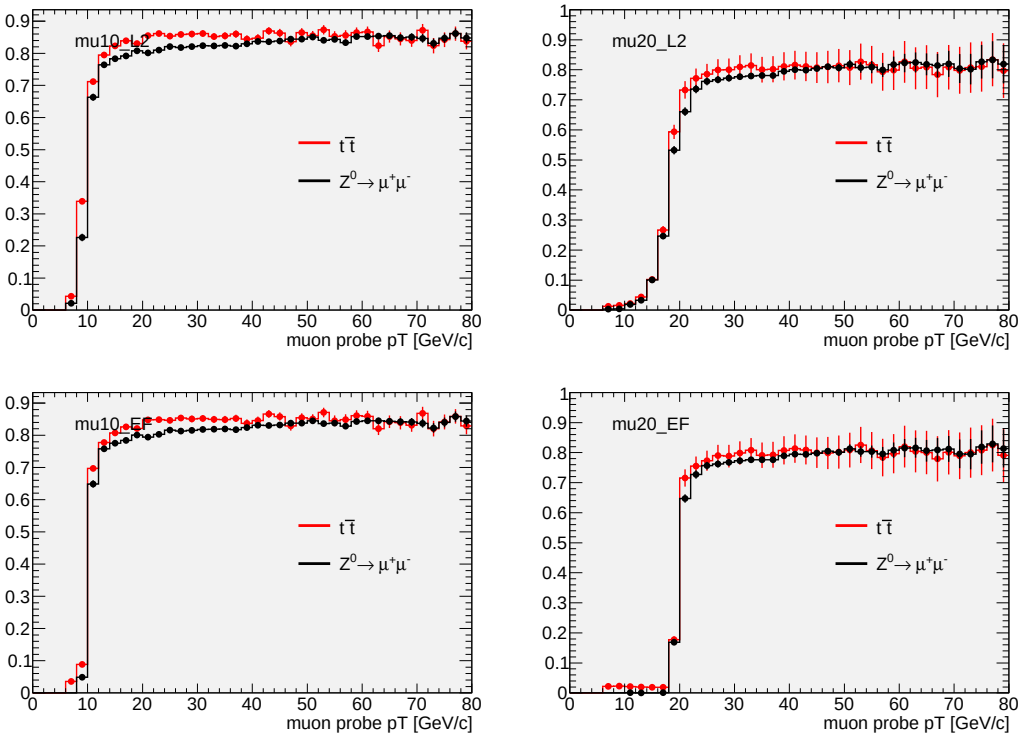

Figure 2.24: Trigger efficiency as a function of transverse momentum: comparison between $Z^0 \rightarrow \mu\mu$ and $t\bar{t}$ samples at L2 (top) and EF (bottom) for mu10 (left) and mu20 (right) chains.

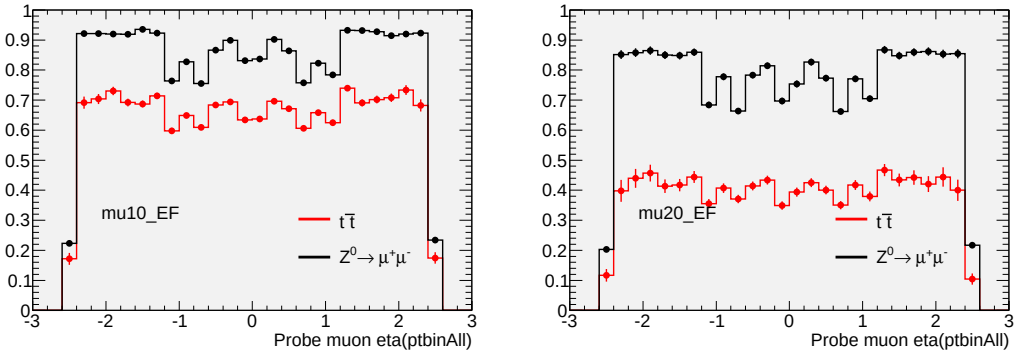

Figure 2.25: Trigger efficiency as a function of pseudorapidity: comparison between $Z^0 \rightarrow \mu\mu$ and $t\bar{t}$ samples at EF for mu10 (left) and mu20 (right) chains.

We separate muons' pseudorapidity distribution in three bin of p_T:

- low efficiency region ($p_T < 20\ GeV/c$)
- intermediate region ($20\ GeV/c < p_T < 30\ GeV/c$)
- plateau region ($p_T > 30\ GeV/c$)

The trigger efficiency as a function of η for the three p_T regions is shown in figure 2.26 at EF level. The efficiencies match almost perfectly, except for the low-p_T region for mu10.

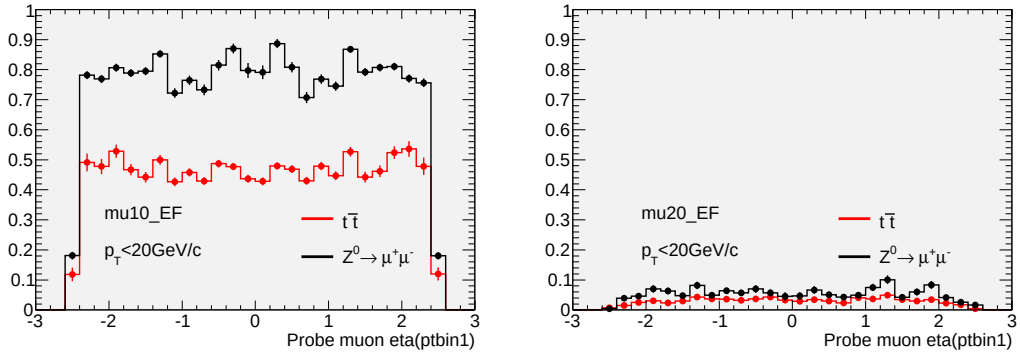

(a) η efficiency for muons with $p_T < 20\ GeV/c$

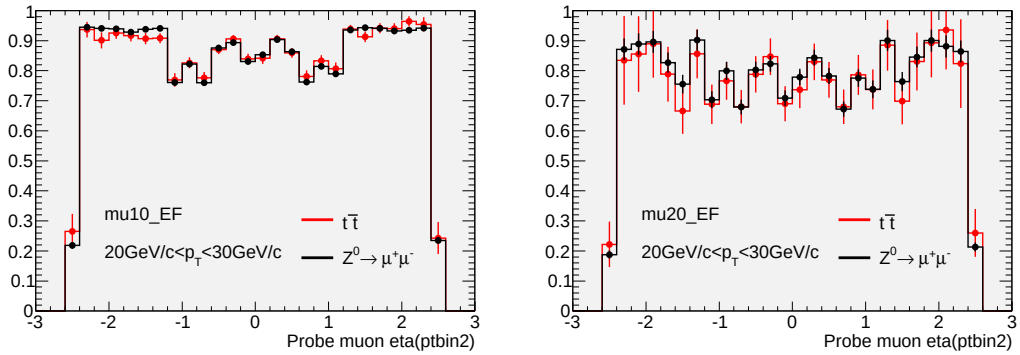

(b) η efficiency for muons with $20 < p_T < 30\ GeV/c$

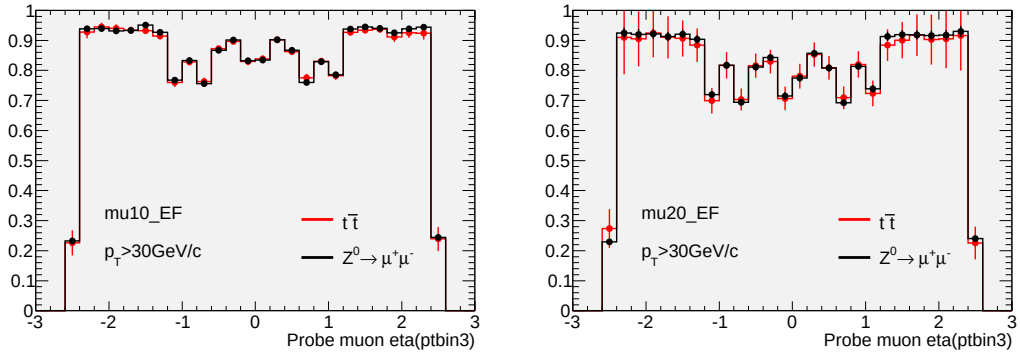

(c) η efficiency for muons with $p_T > 30\ GeV/c$

Figure 2.26: Trigger efficiency as a function of pseudorapidity: comparison between $Z^0 \to \mu\mu$ and $t\bar{t}$ samples at EF for mu10 (left) and mu20 (right) chains.

2.8 Calibration studies using $Z^0 \rightarrow e^+e^-/\mu^+\mu^-$

Single Z^0 production is one of the most important processes for calibration studies. By exploiting the dilepton Z^0 decay, a calibration of the lepton jet energy scale can be performed by the study of the dilepton invariant mass distribution. The trigger efficiency can be measured as well using one lepton as "tag" and the other as "probe". Furthermore the jet energy scale can be estimated using Z^0+1 jet events, where the jet balances the Z^0 transverse momentum. The Z^0 p_T is reconstructed from the two leptons and the requirement of p_T balance allows transferring the lepton energy calibration to the jets. Such studies can be performed already in the very first period of the data taking. The following subsections illustrate some examples of calibrations based on the pseudo-data sample which is described in the following section.

2.8.1 The Pseudo-data Topmix sample

Before data taking, the ATLAS collaboration produced a sample of Monte Carlo generated events mixed in such a way to resemble real data for an integrated luminosity of $99\ pb^{-1}$ taken at $\sqrt{s} = 10\ TeV$ for typical $t\bar{t}$ and single top selections. The mixing has be done taking events from all the different signal and background samples, renumbering the events and removing the Monte Carlo truth. The resulting sample has then be written out to multiple streams (electron, muon etc) as for real data. This sample should then be as similar to real data as possible, and provide a good basis for exercising data-driven analysis in the last months before real data is available.

The mixed samples are:

- $t\bar{t}$: AcerMC [42] sample;
- Single top: Only Wt and t-channel events were available, generated with AcerMC;
- W+jets: Alpgen samples for W+0,1,2,3,4 and $\geq$5 partons;
- Wbb+jets: Alpgen Wbb+0,1,2 and $\geq$3 partons;
- Z+jets: Alpgen samples for Z+0,1,2,3,4 and $\geq$5 partons;

- Di-boson ($WW/WZ/ZZ$): HERWIG samples, containing all final states but with a filter requiring at least one lepton within the acceptance.

The QCD multi-jet background has not been included and thus it will not be considered in the following.

2.8.2 Lepton energy scale

The Z^0 signal was selected by requiring 2 good electrons or muons defined as follows:

- Electrons
  - Tight electrons (sec. 2.3)
  - $p_T > 20\ GeV/c$
  - $|\eta| < 2.5$ except the barrel/end-caps "crack" region $1.37 < |\eta| < 1.52$
  - $E_{T,cone}(0.2) < 6\ GeV$
- Muons
  - STACO combined (sec. 2.4) muons
  - $p_T > 20\ GeV/c$
  - $|\eta| < 2.7$
  - $E_{T,cone}(0.3) < 6\ GeV$

The same selection cuts of is applied to the $t\bar{t}$ cross section analysis (see Section 3 for details on the lepton selection requirements). Figure 2.27 shows, for the electron and muon channels, the comparison between pseudo-data (dots) and Z^0 MC (red histogram) for the p_T and η of the leptons. In order to have agreement between pseudo-data and MC an overall normalization factor of 0.92 have been applied to the MC

Figure 2.28 shows the comparison between pseudo-data (dots) and Z^0 MC (red histograms) for the dilepton invariant mass of the electron and muon channels, respectively. In both case an overall good agreement between simulated data and MC is found.

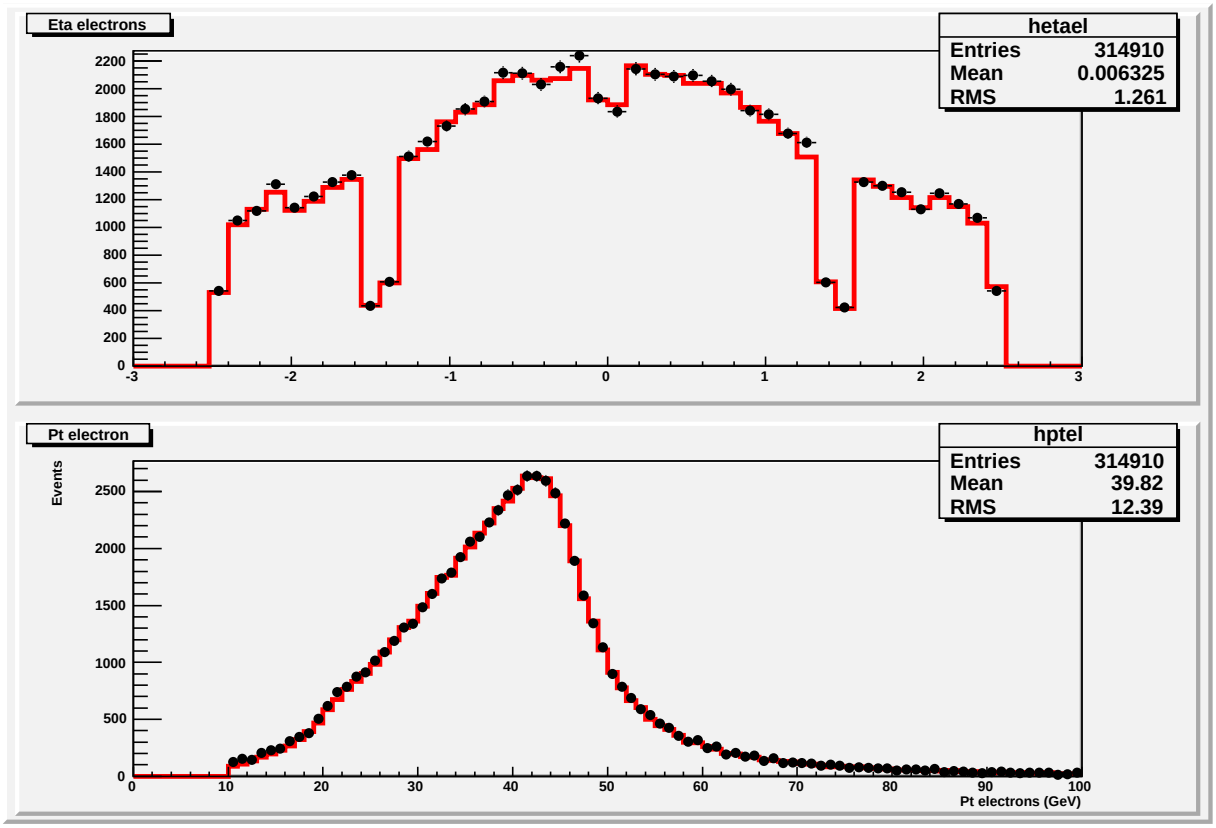

(a) Electrons

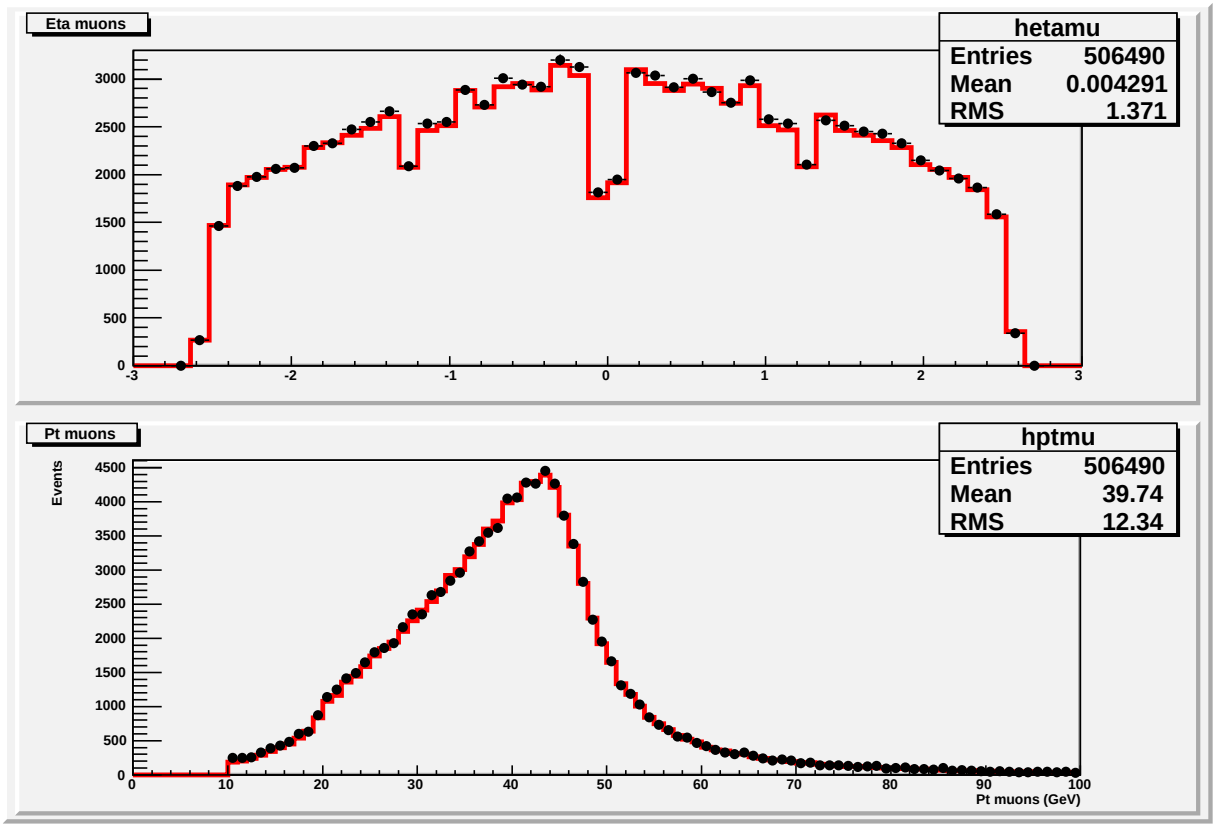

(b) Muons

Figure 2.27: Comparison between pseudo-data (dots) and Z^0 MC (red histogram) for the p_T and η of the leptons.

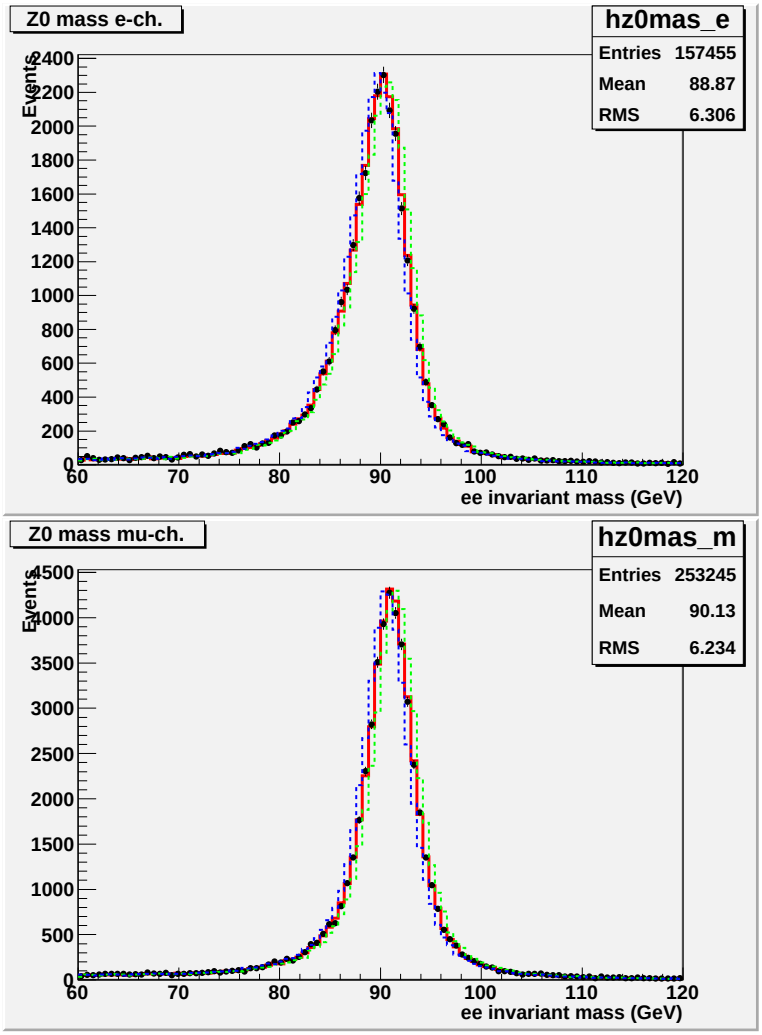

Figure 2.28: Comparison between pseudo-data (dots) and Z^0 MC (red histograms) for the dilepton invariant mass of the electron and muon channels.

In the same plots is also shown the effect of a miscalibration in the lepton energy scale of +0.5% (dashed green histogram) and -0.5% (dashed blue histogram) obtained rescaling the lepton energy scale in the MC. The effect is clearly visible, indicating that the sensitivity on the lepton energy scale with an integrated luminosity of $\sim 100\ pb^{-1}$ is $\leq$0.005. The following figure 2.29 shows the same invariant mass distributions in two bin of eta (region $|\eta| < 1.5$ and $|\eta| > 1.5$), the agreement is good in both regions.

2.8.3 Jet energy scale

The lepton energy calibration can be transferred to jet in events where the final state Z^0 is accompanied by one single jet which balances the Z^0 p_T. Such events can be selected requiring, in addition to the selection described above, a good jet with $p_T > 20$ GeV reconstructed with the same algorithm and the same selection used in the $t\bar{t}$ analysis. The jet p_T and η distributions after the selection are shown in figure 2.30 for the electron and muon selection; the MC simulation is in good agreement with the pseudo-data. Figure 2.30 shows the difference (again for the electron and muon channel) in the azimuthal angle ($\Delta\phi$) between the Z^0 (reconstructed from the leptonic decay products) and the jet (top plot), the η (middle plot) and p_T (low plot) of the selected jets.

As expected most of the selected events have a back to back topology in the transverse plane. In order to select a sample well balanced in p_T a cut $|\pi - \Delta\phi| < 0.2$ was applied. Figure 2.31 compares the jet and the Z^0 reconstructed p_T in different p_T bins using the variable $\frac{P_T(jet)-P_T(Z^0)}{P_T(Z^0)}$. This procedure can be used to calibrate *in-situ* the reconstructed jet energy scale to the absolute scale. In particular, it gives the energy lost out of the jet cone. The jet energy lost out of the cone decreases towards high p_T since the jet become narrower. In this analysis we are not interested in such a correction, but only in the study of the agreement between the pseudo-data and the Monte Carlo.

All these distribution show a good agreement between peudo-data and MC, hence no corrections seems to be necessary.

In order to improve the statistics the same $\frac{P_T(jet)-P_T(Z^0)}{P_T(Z^0)}$ distribution is shown in figure 2.32 for two p_T ranges (20-40 GeV and $>$ 40 GeV). A gaussian fit on the top of the distribution gives an error on the mean value $\sim$ 2%. This error is related to the sensitivity on the jet energy scale. Anyway such distributions

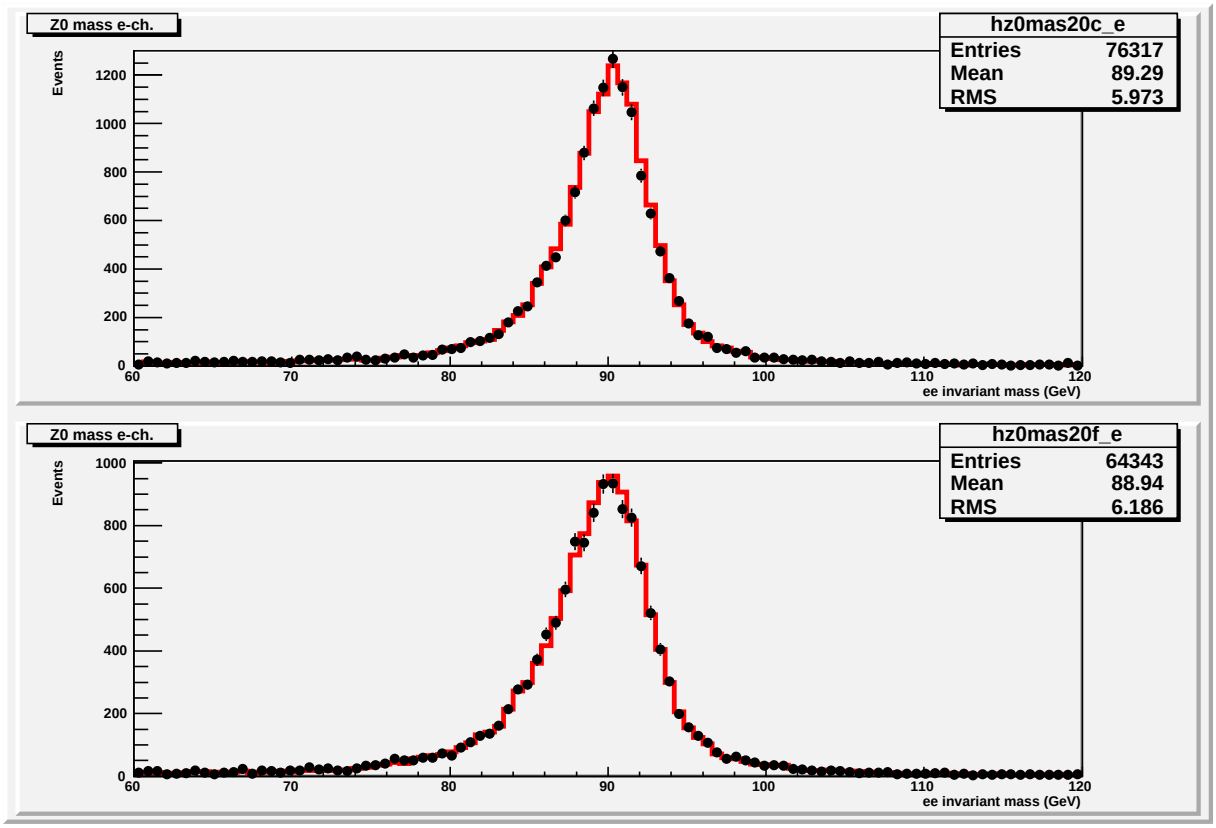

(a) Electrons

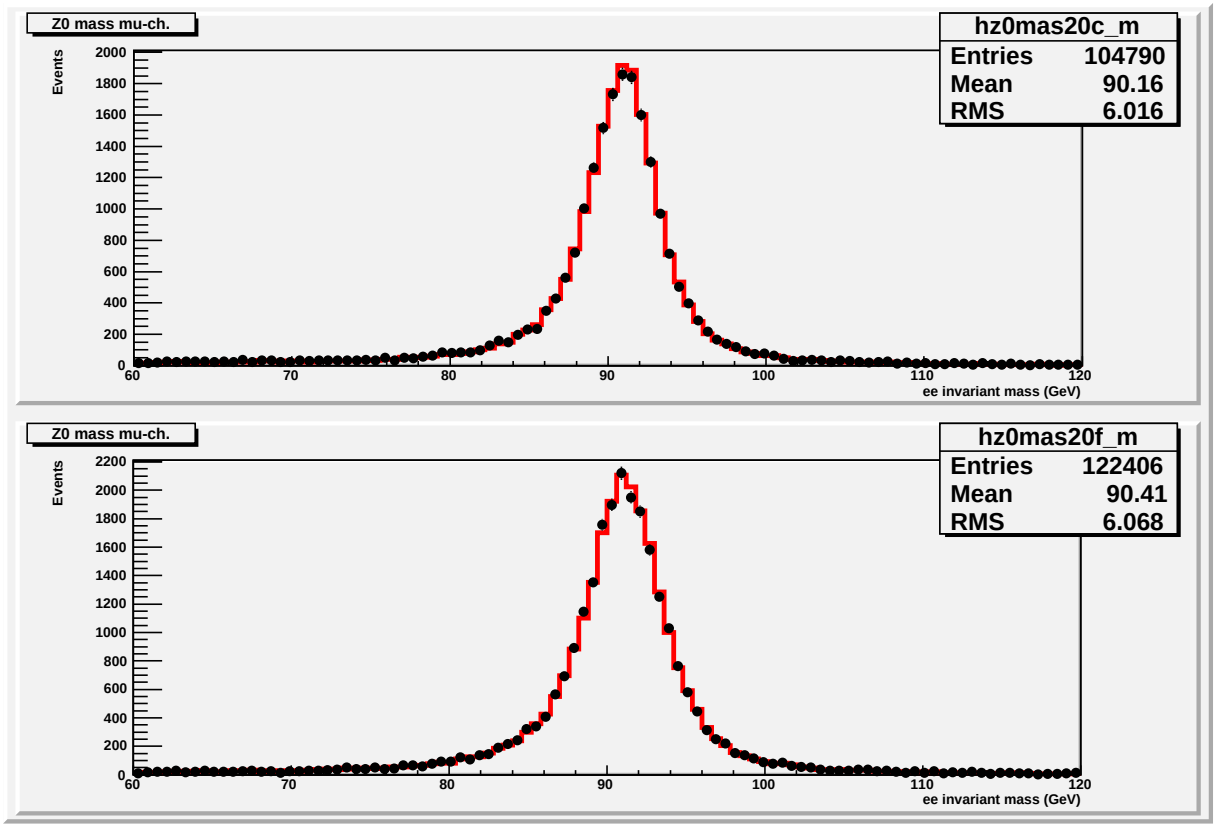

(b) Muons

Figure 2.29: Invariant mass distributions in two bin of eta (region $|\eta| < 1.5$ and $|\eta| > 1.5$).

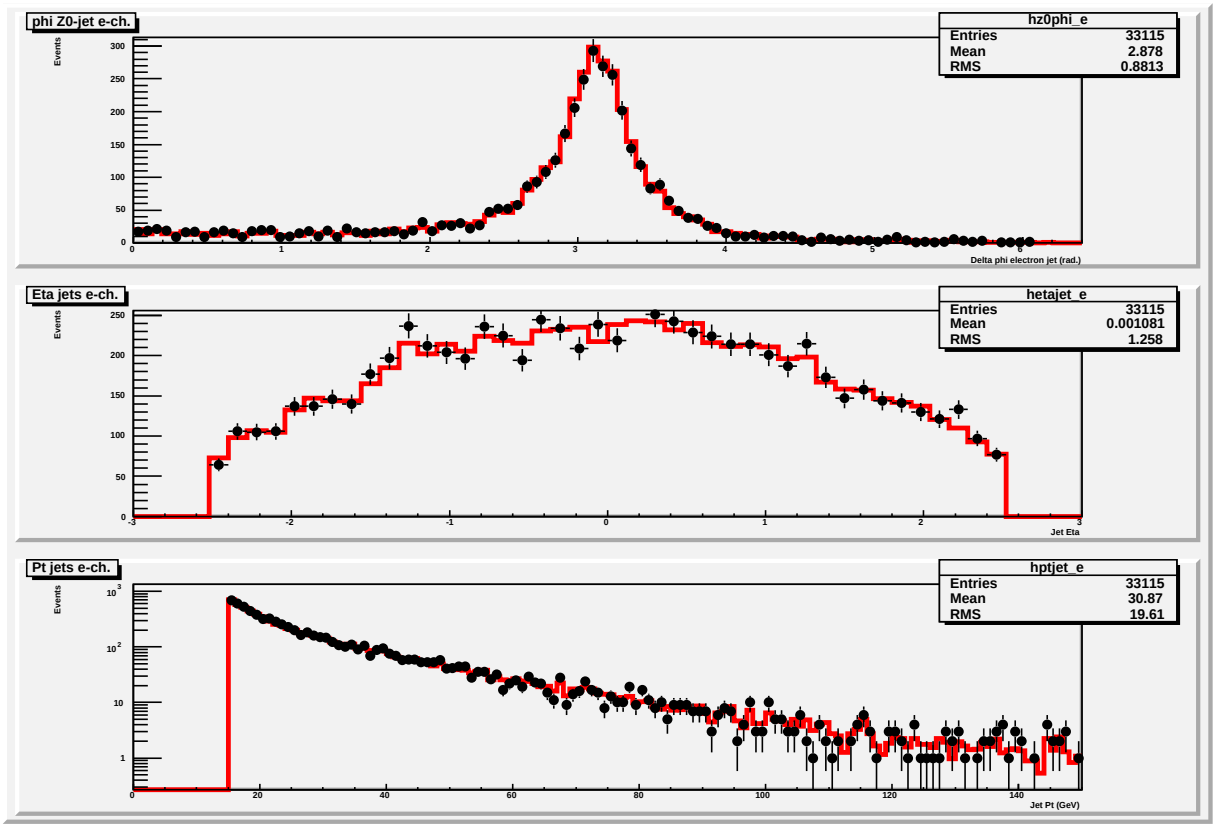

(a) Electrons

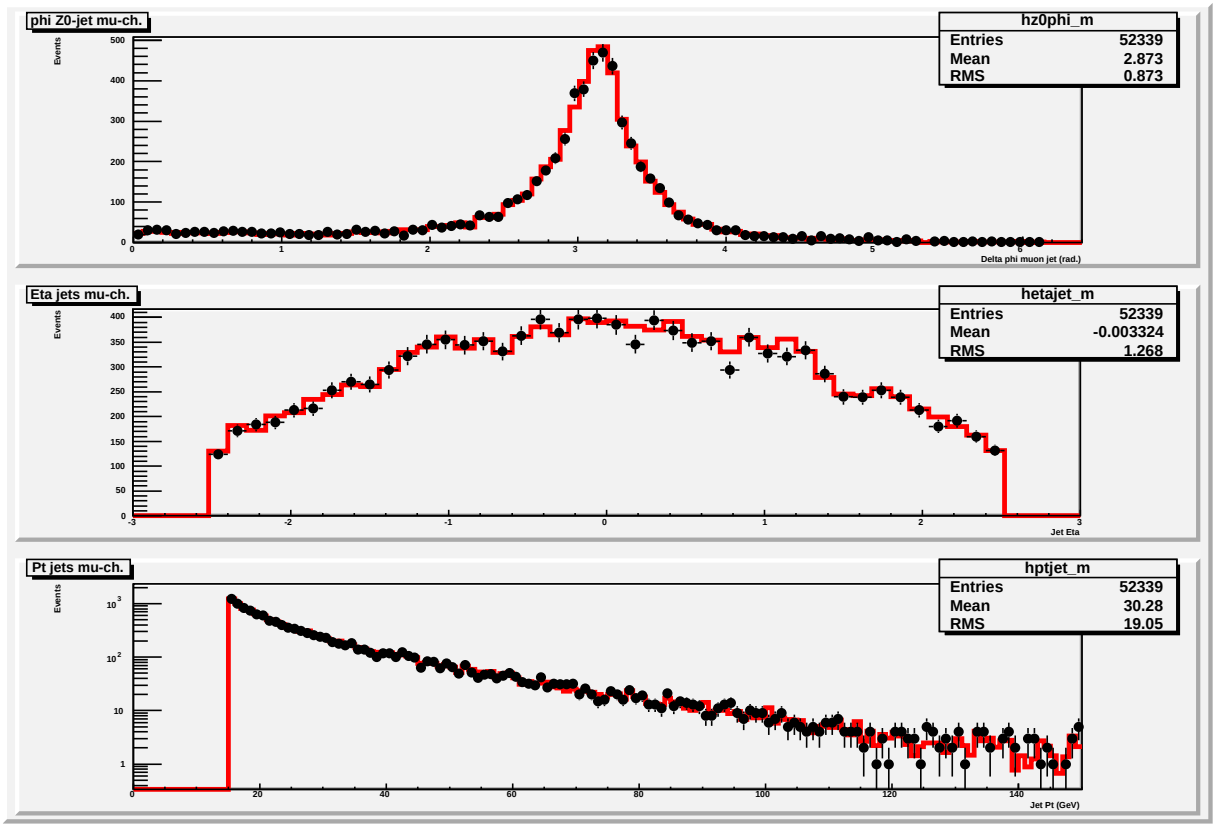

(b) Muons

Figure 2.30: Difference in the azimuthal angle ($\Delta\phi$) between the Z^0 (reconstructed from the leptonic decay products) and the jet (top plot), the η (middle plot) and p_T (low plot) of the selected jets. The full dots represent the pseudo-data and the red histograms the MC predictions.

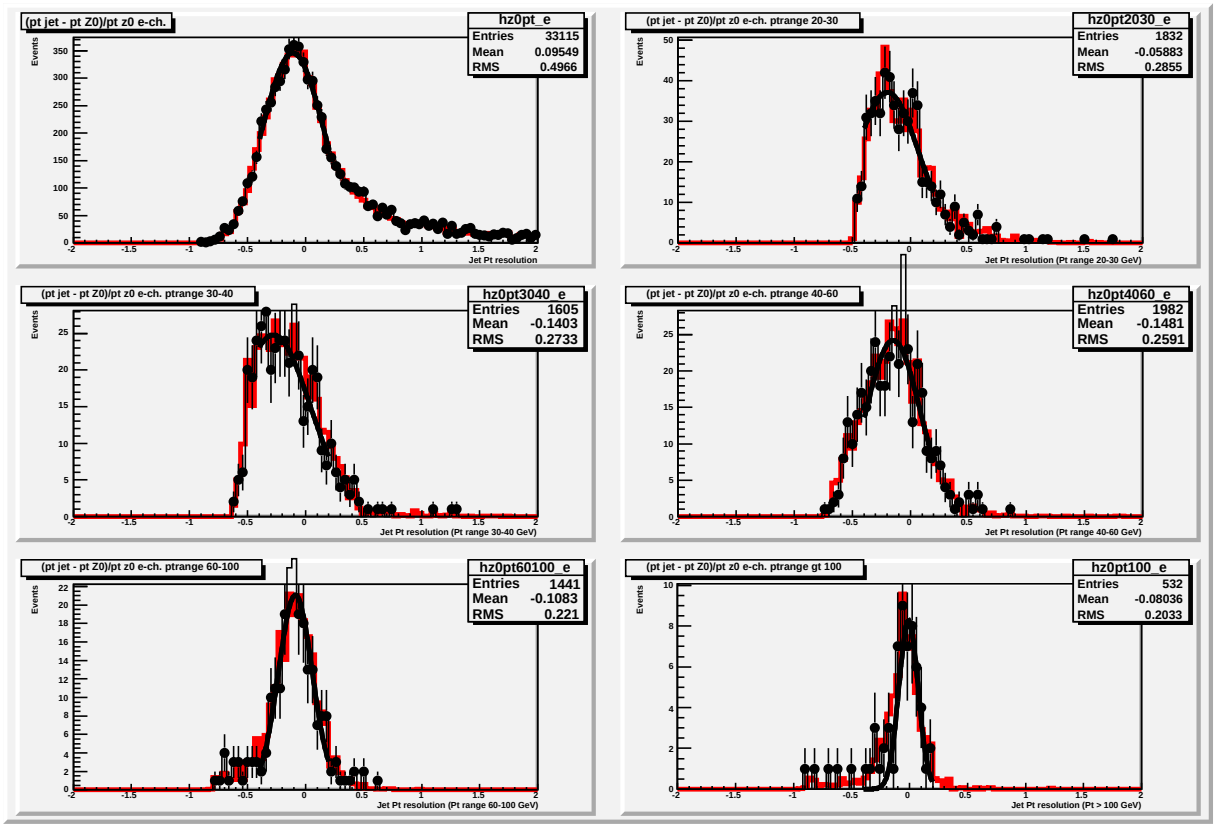

(a) Electrons

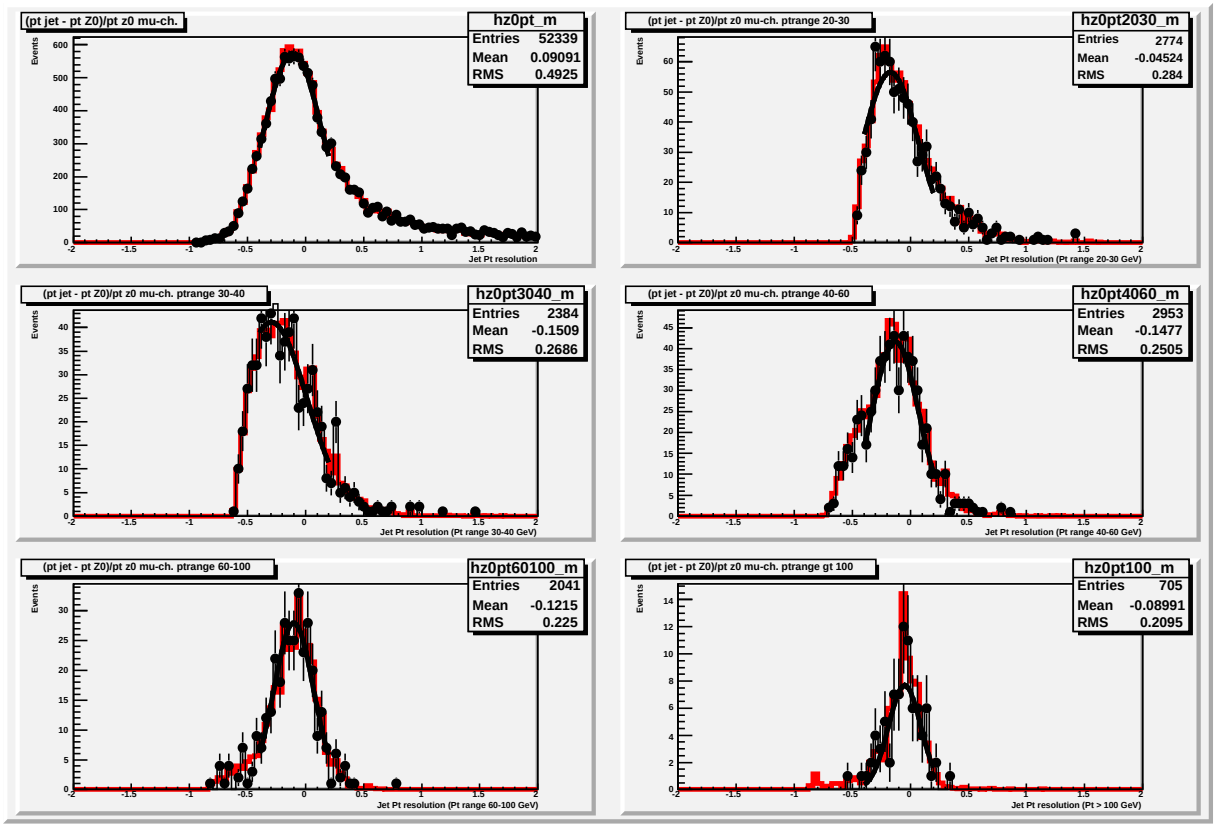

(b) Muons

Figure 2.31: Jet and the Z^0 reconstructed p_T in the decay channels $ee/\mu\mu$ in different p_T bins using the variable $\frac{P_T(jet)-P_T(Z^0)}{P_T(Z^0)}$.

exhibit a clear non gaussian behaviour. Taking into account this fact and also considering that these checks rely on MC simulations not including the QCD background, in the analysis we used a conservative value of 3% for the jet energy scale uncertainty.

2.8.4 Trigger efficiency (tag and probe)

The global lepton trigger efficiency in this sample of dilepton events can be measured by requiring a single lepton trigger and checking if the second lepton also satisfies the trigger conditions. For both the electron and the muon channel the triggers considered here are mu_20 and e20_loose (the same used in the $t\bar{t}$ analysis) and require a lepton with a $p_T > 20$ GeV. The dilepton samples used to this purpose was selected requiring two good leptons with a $p_T > 20$ GeV and an invariant mass in the range $84 - 94$ GeV for the electrons and $88 - 94$ GeV for the muons. The electron mass range is asymmetric due to the radiative tail which enhance the distibution for masses below the Z^0 mass. Figure 2.33 shows, for the electron and muon channel, respectively, the global trigger efficiency (AND between level 1, level 2 and event filter) using one lepton as "tag" and the other as "probe" for the pseudo-data (black dots) and the Z^0 MC (red squares). In both cases an overall good agreement is shown between the pseudo-data and the MC, in particular the critical turn on region is well described.

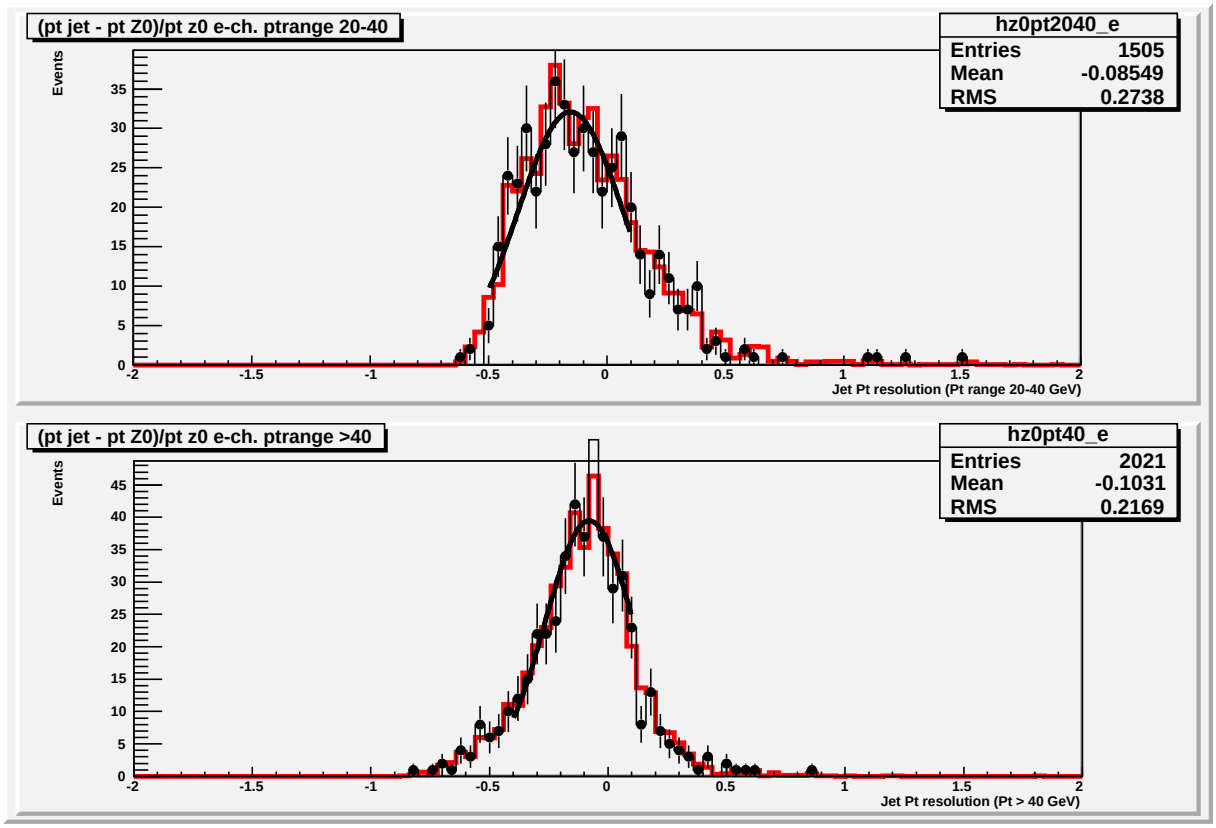

(a) Electrons

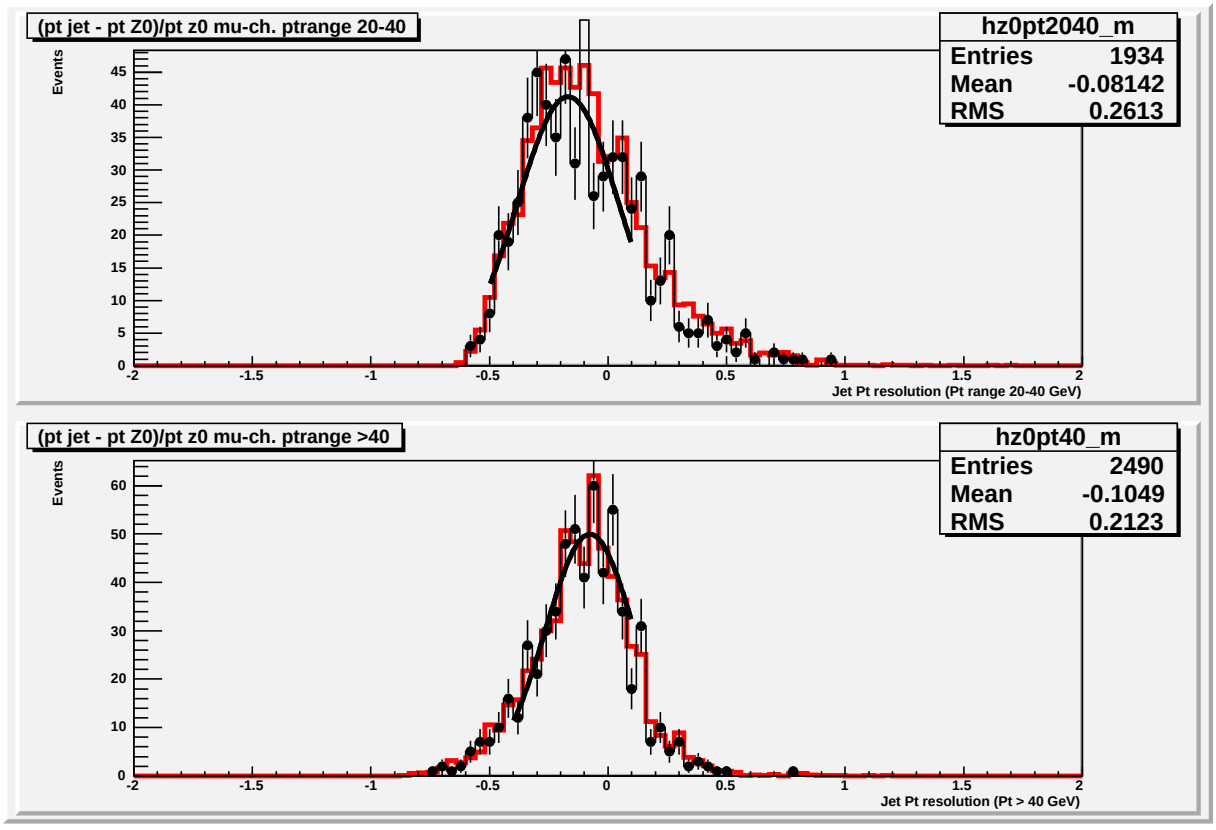

(b) Muons

Figure 2.32: Jet and the Z^0 reconstructed p_T in the decay channels $ee/\mu\mu$ in different p_T bins using the variable $\frac{P_T(jet)-P_T(Z^0)}{P_T(Z^0)}$.

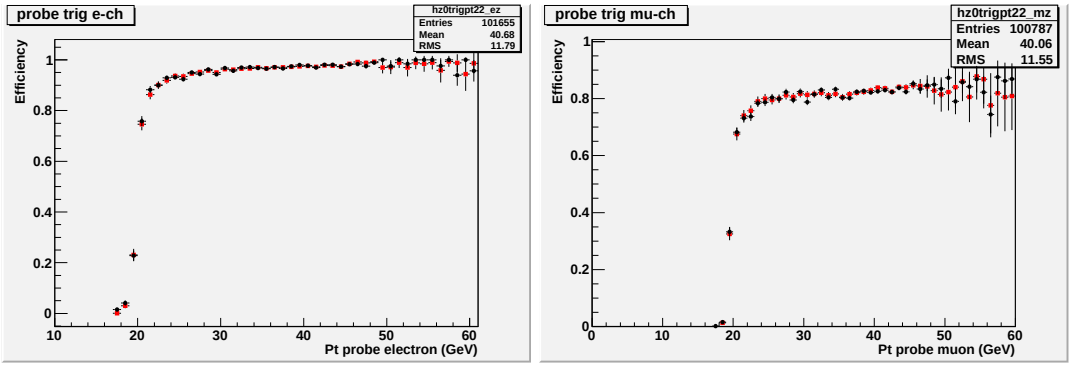

Figure 2.33: Global trigger efficiency (AND between level 1, level 2 and event filter) using one lepton as ”tag” and the other as ”probe” for the pseudo-data (black dots) and the Z^0 MC (red squares).

Chapter 3

The Cut-Based Analysis for $t\bar{t}$ Semi-leptonic Events

3.1 Input Datasets and Analysis Programs

In the following, only Monte Carlo samples produced at a center-of-mass energy $\sqrt{s} = 10\ TeV$ by the ATLAS collaboration in the "MC08" generation run have been used. All cross-sections and k-values for normalization at NNLO are taken shown in tables 3.1 and 3.1. Datasets are present on the Grid and have been analyzed using the tool `BoD3PDMaker` [51] developed by the author of this work.

The final step of this analysis has been carried out using custom-made C++/ROOT programs that run on the local cluster that belongs to the ATLAS group [4] of INFN and University of Bologna.

3.2 Benchmark Selection

In order to isolate $t\bar{t}$ events against the full background, a first study has been made using a selection based on simple kinematical cuts, studied previously with Monte Carlo events generated at $14\ TeV$ [24] and $10\ TeV$ [16]. First of all, only events with a lepton trigger are used. Triggers have been chosen from the Trigger Menu list for the luminosity of $10^{31} cm^{-2} s^{-1}$. In particular, the following non-prescaled trigger chains have been picked up:

Sample	ATLAS ID	No. of partons	$\sigma_{eff}\times$ BR [pb]	k_{NNLO}	Luminosity [pb^{-1}]
$W \to e\nu$	107680	0	10184.7	1.22	78.71
	107681	1	2112.4	1.22	101.25
	107682	2	676.0	1.22	943.05
	107683	3	203.3	1.22	905.45
	107684	4	56.1	1.22	860.17
	107685	$\geq$5	16.6	1.22	839.03
$W \to \mu\nu$	107690	0	10125.7	1.22	107.54
	107691	1	2155.5	1.22	102.20
	107692	2	682.3	1.22	937.43
	107693	3	202.0	1.22	857.59
	107694	4	55.5	1.22	855.53
	107695	$\geq$5	16.3	1.22	853.62
$W \to \tau\nu$	107700	0	10178.3	1.22	62.62
	107701	1	2106.9	1.22	68.02
	107702	2	672.8	1.22	672.45
	107703	3	202.7	1.22	898.37
	107704	4	55.3	1.22	871.03
	107705	$\geq$5	17.0	1.22	767.26
$W + bb$	106280	0	5.13	1.22	2476.59
	106281	1	5.01	1.22	2528.88
	106282	2	2.89	1.22	2539.28
	106283	3	1.61	1.22	2545.57
$Z \to ee$	107650	0	898.18	1.22	163.62
	107651	1	206.57	1.22	245.09
	107652	2	72.50	1.22	2452.74
	107653	3	21.08	1.22	2465.70
	107654	4	6.00	1.22	2523.22
	107655	$\geq$5	1.73	1.22	2605.89
$Z \to \mu\mu$	107660	0	900.21	1.22	245.93
	107661	1	205.21	1.22	247.39
	107662	2	69.35	1.22	2448.65
	107663	3	21.63	1.22	2461.52
	107664	4	6.08	1.22	2490.02
	107665	$\geq$5	1.70	1.22	2637.90
$Z \to \tau\tau$	107670	0	902.71	1.22	245.75
	107671	1	209.26	1.22	242.57
	107672	2	70.16	1.22	1762.53
	107673	3	21.07	1.22	2467.73
	107674	4	6.04	1.22	2510.59
	107675	$\geq$5	1.71	1.22	2626.31

Table 3.1: Background datasets generated at $\sqrt{s} = 10\ TeV$ - $W/Z + jets$. Effective cross-sections includes matrix-elements/partons-shower matching efficiency and other generator efficiencies. The k_f factor rescales LO cross-sections to NNLO.

Sample	**ATLAS ID**	$\sigma_{eff}\times$ BR $\times k_{NNLO}$ [pb]	Luminosity [pb^{-1}]
$t\bar{t}$ full-hadronic	105204	182.69	5461.46
Single top Wt No full-had	105500	14.27	1399.35
Single top t-channel	105502	43.18	693.93
Single top Wt di-leptonic	105503	2.76	14478.11
Single top t-channel	105507	43.18	2895.13
Single top Wt	105508	14.27	7730.60
$WW \rightarrow l\nu l\nu$	107100	3.91	8048.26
$WW + 1p \rightarrow l\nu l\nu$	107101	2.07	8457.78
$WW + 2p \rightarrow l\nu l\nu$	107102	1.05	8074.48
$WW + 3p \rightarrow l\nu l\nu$	107103	0.44	9180.44
WZ	107104	1.27	6690.28
$WZ + 1p$	107105	0.88	6748.56
$WZ + 2p$	107106	0.52	8648.86
$WZ + 3p$	107107	0.24	8264.46
ZZ	107108	0.97	8264.46
$ZZ + 1p$	107109	0.47	8476.37
$ZZ + 2p$	107110	0.22	9182.74
$ZZ + 3p$	107111	0.07	13774.10

Table 3.2: Background datasets generated at $\sqrt{s} = 10\ TeV$ - Single top, $t\bar{t}$ with full-hadronic decays, $WW/WZ/ZZ$. Effective cross-sections includes k-factor, matrix-elements/partons-shower matching efficiency and other generator efficiencies. The k_f factor rescales LO and NLO cross-sections to NNLO.

- e20_loose
- mu20

The trigger e_20_loose selects events that contain at least one loose electron (see section 2.3) with $p_T > 20GeV/c$, while mu_20 selects events with at least one muon $p_T > 20GeV/c$. No specific isolation cuts are applied at this stage, but the usage of "isolated" leptonic trigger such as e_20i and mu_20i is also possible. However, at the beginning of data taking isolation variables will not be fully understood yet, so a broader selection is safer. The possibility to use a missing transverse energy trigger combined to a lepton trigger is under study, too.

In order to enhance the purity of the sample, further cuts and selections are applied:

- Electrons
  - Tight electrons (sec. 2.3)
  - $p_T > 20\ GeV/c$
  - $|\eta| < 2.5$ except the barrel/end-caps "crack" region $1.37 < |\eta| < 1.52$
  - $E_{T,cone}(0.2) < 6\ GeV$
- Jets
  - AntikKt jets with $D = 0.4$
  - $p_T > 20\ GeV/c$
  - $|\eta| < 2.5$
  - Jets closer to a good electron than $\Delta R < 0.2$ are removed (overlap removal).
- Muons
  - STACO combined (sec. 2.4) muons
  - $p_T > 20\ GeV/c$
  - $|\eta| < 2.7$
  - $E_{T,cone}(0.3) < 6\ GeV$

  - Muons closer to a good jet than $\Delta R < 0.3$ are considered as decayed from a hadron in the jet, and are thus removed.

- Missing E_T The missing transverse energy is calibrated and refined (see 2.6).

A breakdown of the the selections used in [16] is provided here:

1. Leptonic trigger is considered to be more reliable than jet and/or missing E_T ones in the first phases of operation, so no trigger on E_T^{miss} is used;

2. Lepton multiplicity must be exactly one, matching the flavour of the trigger. This will enhance the purity of the signal;

3. The amount of missing transverse energy must be compatible with the presence of an escaped neutrino and high enough to avoid a low-energy region where mismeasurements can be large. The threshold is set to $20\ GeV$;

4. Only events with at least 4 jets with a transverse momentum greater that $20\ GeV/c$ are kept;

5. At least 3 jets must have a $p_T > 40\ GeV/c$ to fulfill the kinematic of a semi-leptonic decay. Moreover, this request helps to clean the sample from W/Z backgrounds.

3.2.1 Determination of the Cross-section

The simplest method to determine the measured cross-section is to count all the events that passed the final selection (N_{obs}) and subtract the number of expected background events (N_{bkg}) as predicted by the Monte Carlo simulation and data-driven methods. The master equation for the cross-section is:

$$\sigma_{t\bar{t}} = \frac{N_{sig}}{\mathcal{L} \times \epsilon} = \frac{N_{obs} - N_{bkg}}{\epsilon \times \mathcal{L} \times \mathcal{BR}} \tag{3.1}$$

Where $\mathcal{L}$ is the integrated luminosity of $200\ pb^{-1}$ and $\mathcal{BR}$ is the branching ratio of the selected semi-leptonic decays in e/μ, equal to:

$$\mathcal{BR} = 2 \times \left[\left(\left(\frac{1}{9}\right)_e + \left(\frac{1}{9}\right)_\mu \right) \times \left(\frac{2}{3}\right)_{qq'} \right] = \frac{8}{27} \sim 29.6\% \tag{3.2}$$

The efficiency ϵ includes the geometrical acceptance, the trigger efficiency and the event selection efficiency, and is slightly dependent on the top mass. In turn, the number of background events N_{bkg} can be expressed as the sum of the contributions of all the separate background processes:

$$N_{bkg} = \epsilon_{bkg}\sigma_{bkg}\mathcal{L} = \mathcal{L} \sum_{i}^{(all\ bkg)} \epsilon_i \frac{\sigma_i}{\mathcal{L}_i} \tag{3.3}$$

The precision on σ_{tt} depends on statistical and systematic errors of the various σ_i and on the error on the measurement of the luminosity. The statistical uncertainty on σ_{tt} is given by:

$$\Delta\sigma = \frac{1}{\mathcal{L}\mathcal{BR}\,\epsilon}\sqrt{N_{obs} + (\delta N_{bkg})^2 + \frac{1-\epsilon}{\epsilon N_{bkg}}(N_{obs} - N_{bkg})^2} \tag{3.4}$$

The statistical error has been evaluated to be 2.7% for the muon channel and 2.8% for the electron channel. The statistical error on N_{bkg} from Monte Carlo is negligible due to the very large number of simulated events that have been produced. Thus, the error on the cross-section is well approximated by:

$$\Delta\sigma_{tt}^{(stat)} = \sigma_{tt}\frac{\Delta N_{obs}}{N_{obs} - N_{bkg}} \tag{3.5}$$

3.2.2 Results of Benchmark Analysis Applied to Pseudo-data

A number of distributions have been controlled in order to check if Monte Carlo samples reproduce the pseudo-data correctly. Figures 3.1 and 3.2 show some of these variables for object properties and event-wise reconstructed quantities.

The benchmark selection has been applied to the two channels separately as follows:

- **Electron Channel**

  1. Trigger EF_e20_loose

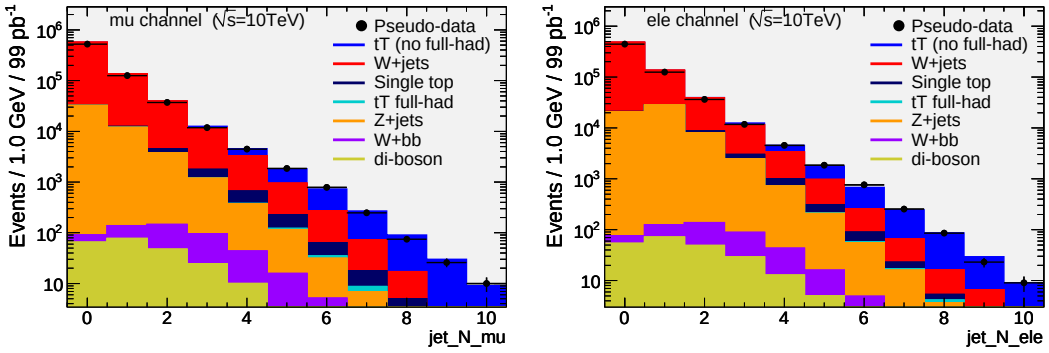

(a) Number of jets

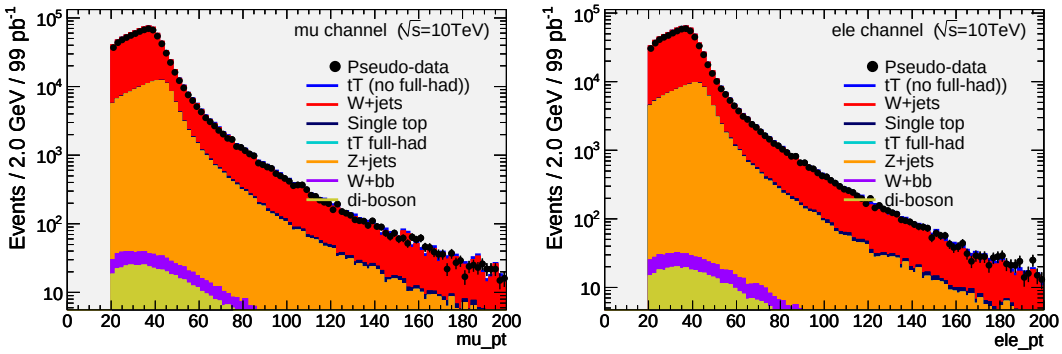

(b) Transverse momentum of leptons

Figure 3.1: Control plots for the comparison between pseudo-data and MC samples.

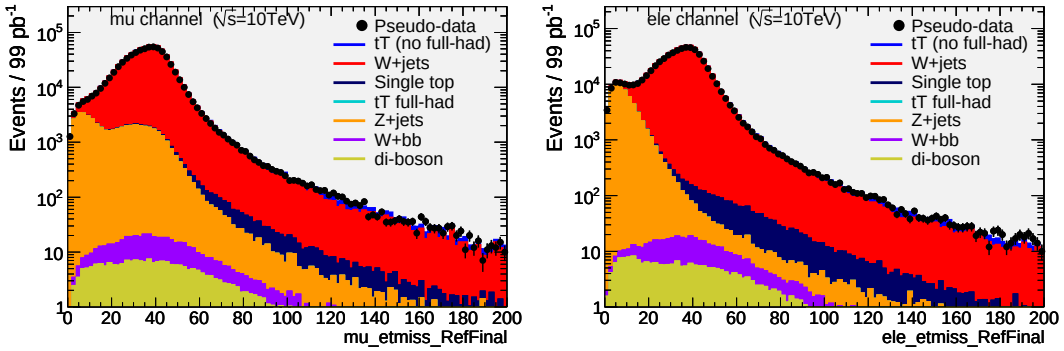

(a) Missing Transverse Energy

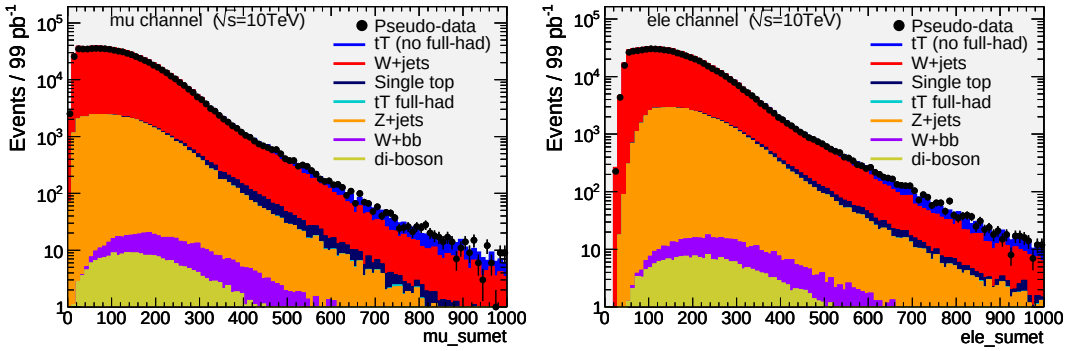

(b) Scalar Sum of Transverse Energy

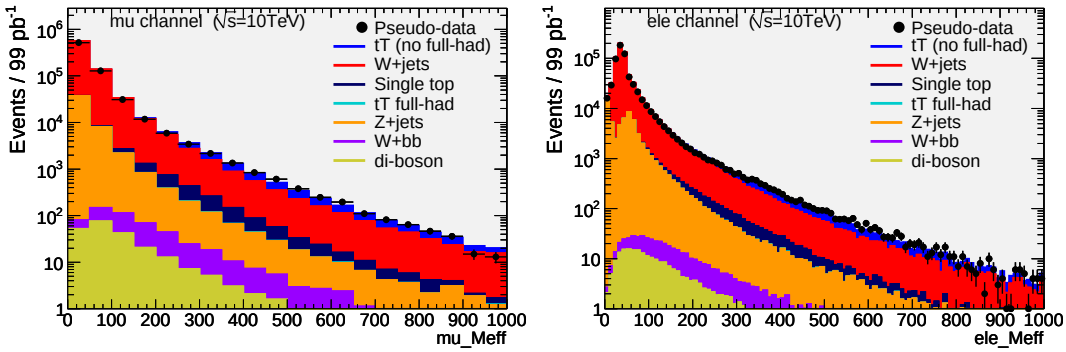

(c) Effective Mass

Figure 3.2: Control plots for the comparison between pseudo-data and MC samples.

2. Exactly one tight electron with $p_T > 20\ GeV/c$ and $|\eta| < 2.5$
3. $E_T^{miss} > 20\ GeV$
4. At least 4 jets with $p_T > 20\ GeV/c$ and $|\eta| < 2.5$
5. At least 3 of them must have $p_T > 40\ GeV/c$

- **Muon Channel**

1. Trigger EF_mu20
2. Exactly one STACO combined muon with $p_T > 20\ GeV/c$ and $|\eta| < 2.7$
3. $E_T^{miss} > 20\ GeV$
4. At least 4 jets with $p_T > 20\ GeV/c$ and $|\eta| < 2.5$
5. At least 3 of them must have $p_T > 40\ GeV/c$

Efficiency on the signal has been evaluated applying the same analysis on the POWHEG $t\bar{t}$ sample. Using the Monte Carlo truth, the efficiency in p_T and η of top quarks has been compared before and after the selection cuts, as shown in figure 3.3. The efficiency on signal $\epsilon_S = 7.92\%$ for the muon channel and $\epsilon_S = 7.28\%$ for the electron channel.

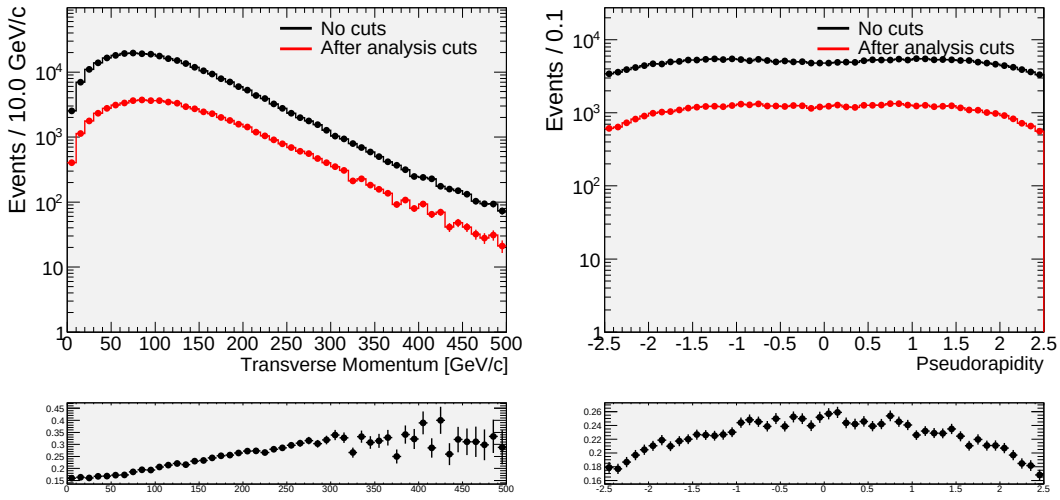

Figure 3.3: Efficiency in p_T (left) and η of top quarks as measured using Monte Carlo truth.

As result, tables 3.2.2 and 3.2.2 show the number of events surviving each cut of the analysis, for each group of backgrounds. The resulting cross section extracted from pseudo-data is $467.7 \pm 14.0(stat)\ pb$ for the electron channel and $438.3 \pm 13.0(stat)\ pb$ for the muon channel.

Dataset	Tot	Trig	S.L.	E_T^{miss}	4 jets	jet p_T cut	m_t	m_W
Pseudo-data	1165384	792420	706141	634595	5253	2905	2691	1831
tT no fullHad	21495	6122	4423	4020	2364	1633	1536	1137
W+jets	4788065	744840	710489	656397	2266	862	771	467
Single top	10413	2551	2092	1871	313	163	147	98
Z+jets	436541	105213	48666	25657	157	62	55	32
tT fullHad	13335	546	17	6	5	4	4	3
Di-boson	1198	422	228	182	7	3	2	1
Wbb	1768	356	308	267	37	18	16	10
All	5251320	853930	761801	684384	2788	1114	998	614

Table 3.3: Cut flow with benchmark selection cuts for an integrated luminosity of 99 pb^{-1} at 10 TeV. Muon Channel.

Dataset	Tot	Trig	S.L.	E_T^{miss}	4 jets	jet p_T cut	m_t	m_W
Pseudo-data	1569114	888719	622390	523277	4919	2794	2543	1757
tT no fullHad	21495	6688	4083	3704	2172	1501	1412	1039
W+jets	4788065	840786	608935	557810	2030	762	683	423
Single top	10413	2872	1946	1734	301	162	145	97
Z+jets	436541	113088	59856	4019	190	89	77	45
tT fullHad	13335	405	8	2	2	1	1	1
Di-boson	1198	473	221	159	6	3	3	2
Wbb	1768	393	269	235	33	17	15	9
All	5251320	958020	671238	563961	2566	1037	927	578

Table 3.4: Cut flow with benchmark selection cuts for an integrated luminosity of 99 pb^{-1} at 10 TeV. Electron Channel.

3.3 Estimation of QCD multi-jet background

In principle, QCD multi-jet events are strongly suppressed by a $t\bar{t}$ semileptonic selection, since all produced leptons come from the semileptonic decay of

mesons, and thus they are not actually isolated and the E_T^{miss} is low. However, detector effects and inefficiencies change this picture, especially for the electron channel.

3.3.1 Monte Carlo estimation based on filtered samples

A dataset with several thousands simulated QCD multi-jet events has been produced with the AlpGen generator and it has been fed into the Atlas detector full simulator. After full simulation, this sample has been filtered into two sub-samples, one containing only events with at least three cone .4 jets with $p_T > 20\ GeV/c$. Another set contains only events with at least one muon with $p_T > 20\ GeV/c$ .These sub-samples can be used for specific analyses. However, events with large fake missing transverse energy represent only a small fraction of the total. Figure 3.4 shows E_T^{miss} distributions for events that have been triggered and present only one isolated electron. Even if at this level the $t\bar{t}$ signal is still below the W+jets background (no cut on jet multiplicity has been applied yet), it can be seen that the signal overcomes the QCD background at $\sim 30\ GeV$. However, it is questionable whether the measurement of the missing transverse energy will be reliable in the first part of data taking. A conservative low value of E_T^{miss} cut set at $20\ GeV$ will be used in the following.

3.3.2 Review of Data-driven Estimation of the QCD Multi-jet Background

The backgrounds from QCD processes are events which have a large E_T^{miss} and an identified lepton which does not come from a real W decay. The lepton can be a real lepton coming from semi-leptonic B hadron (not resulting from a top quark decay) or light-flavour decays. It can also be a faked lepton for example when a pion passes through the calorimeter and it can be misidentified as a muon in the Muon Spectrometer, or a photon conversion is misidentified as an electron. Large E_T^{miss} occurs from jet mismeasurements or when a jet points in a crack between the calorimeter sections. Due to the huge cross section of QCD processes with respect to the $t\bar{t}$ production, the measurement of this background will be data-driven. There are several methods that can be used to do such a measurement, that we briefly review.

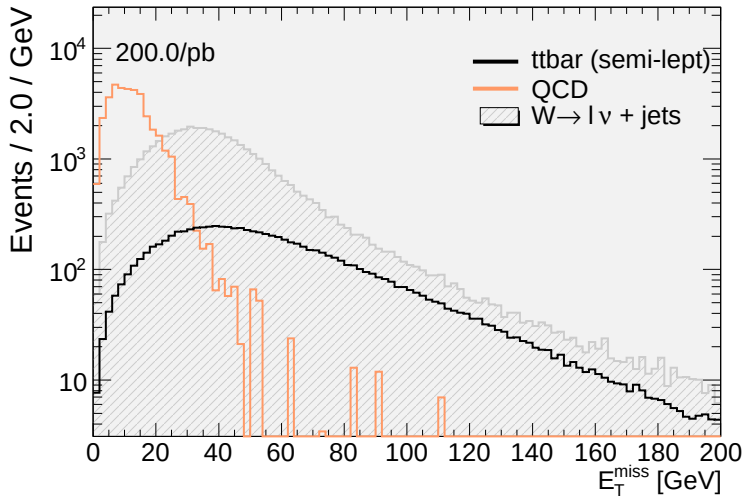

Figure 3.4: E_T^{miss} distributions for $t\bar{t}$ signal, QCD and W+jets backgrounds for events triggered and with a single electron

3.3.2.1 The E_T^{miss} vs Isolation method

The E_T^{miss} *vs Isolation* method [24] relies on the fact that in the QCD events the E_T^{miss} and the isolation of the tight lepton are uncorrelated, while they are higly correlated in $t\bar{t}$ events. As a consequence the E_T^{miss} spectrum is the same for QCD events with and without an isolated lepton. In QCD events the non-isolated events dominate over the isolated events, so that one can study the E_T^{miss} distribution in the non-isolated sample and extrapolate it in the isolated (signal) region.

The E_T^{miss} vs isolation plane is divided into four quadrants (fig. 3.5):

- **A**: isolated lepton, high E_T^{miss} (signal region)
- **B**: non-isolated lepton, high E_T^{miss}
- **C**: isolated lepton, low E_T^{miss} (control region)
- **D**: non-isolated lepton, low E_T^{miss}

The method assumes that the number of background events in region A

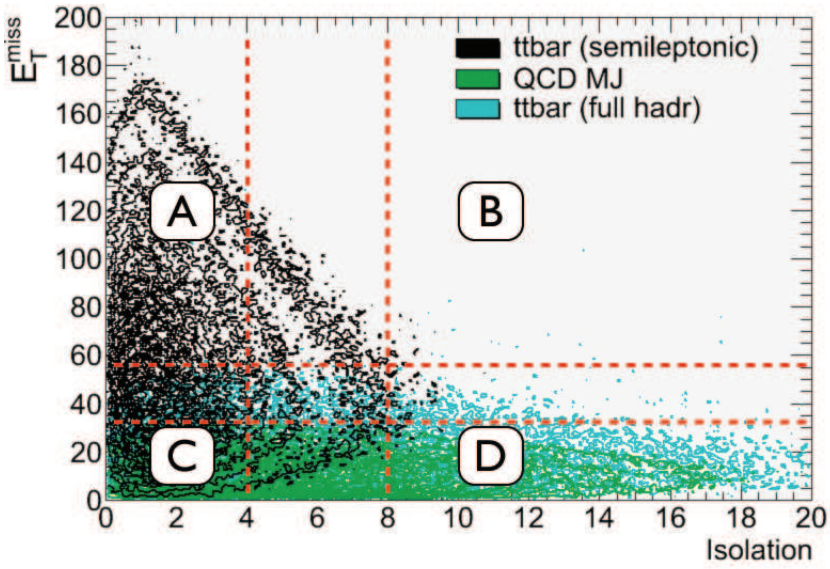

Figure 3.5: Separation of the E_T^{miss} vs isolation plane into signal region (A), control region (C) and background-dominated regions (B,D).

relative to region C is the same as the ratio of events in B and D:

$$\frac{N_A}{N_C} = \frac{N_B}{N_D} \tag{3.6}$$

Thus the number of QCD events in the signal region A and its error are:

$$N_A(QCD) = \frac{N_B}{N_D} N_C \tag{3.7}$$

$$\frac{\delta N_A}{N_A} = \sqrt{\left(\frac{N_C}{N_D}\delta N_B\right)^2 + \left(\frac{N_B}{N_D}\delta N_C\right)^2 + \left(\frac{N_B N_C}{N_D^2}\delta N_D\right)^2} \tag{3.8}$$

Of course, QCD multi-jet background is not the only background present and some corrections could be needed from other processes, mainly $t\bar{t}$ full-hadronic decays and W+jets events. These backgrounds can be estimated with Monte Carlo techniques.

3.3.2.2 Matrix Method

The matrix-method [29] [32] is another way to determine the QCD background through the estimate of the real and fake leptons in the data sample. It is based on the implementation of two quality criteria for the lepton, one tighter than the other (*tight* and *loose* leptons).

We indicate with ϵ_S the rate at which a real loose lepton passes the tight criteria, so that for the signal $N^S_{tight} = \epsilon_S N^S_{loose}$. It can be evaluated using Monte Carlo events o $Z \to ee$ and $Z \to \mu\mu$ data samples. In the same way, if ϵ_{QCD} is the rate for fake loose lepton to pass the tight criteria we have $N^{QCD}_{tight} = \epsilon_{QCD} N^{QCD}_{loose}$.

A method for the determination of ϵ_{QCD} consists in computing the ratio of the number of loose over tight leptons in a low E_T^{miss} range that is dominated by the background, based on the assumption that the loose-tight selection and the E_T^{miss} spectrum are independent.

$$N_{loose} = N^{QCD}_{loose} + N^S_{loose} \tag{3.9}$$

$$N_{tight} = \epsilon_{QCD} N^{QCD}_{loose} + \epsilon_S N^S_{loose} \tag{3.10}$$

Rearranging, after some algebra:

$$N^{QCD}_{loose} = \frac{\epsilon_S N_{loose} - N_{tight}}{\epsilon_S - \epsilon_{QCD}} \tag{3.11}$$

$$N^S_{loose} = \frac{N_{tight} - \epsilon_{QCD} N_{loose}}{\epsilon_S - \epsilon_{QCD}} \tag{3.12}$$

The error on $N^{QCD}_{tight} = \epsilon_{QCD} N^{QCD}_{loose}$ is given by:

$$\delta N^{QCD}_{tight} = \sqrt{\left(\frac{\epsilon_S \epsilon_{QCD}}{\epsilon_S - \epsilon_{QCD}}\right)^2 (N_{loose} - N_{tight}) + \left(\frac{\epsilon_{QCD}(1-\epsilon_S)}{\epsilon_S - \epsilon_{QCD}}\right)^2 N_{tight}} \tag{3.13}$$

3.4 Estimation of W+jets background from real data

The Monte Carlo models for the production of W+jet events have predictions that differ even more than 20%. On the other hand, the W to Z ratio is predicted with a much smaller uncertainty [7]. The jet multiplicity can be measured better in Z events with respect to W events, even at high jet multiplicities. One the other hand, W bosons can be selected with good purities at low jet multiplicities. Therefore, the idea is to extrapolate from a control region (CR) with zero or one jets into the top signal region (SR) with four or more jets and estimate the number of W+jets background events using [24]:

$$\left(\frac{N_W(CR)}{N_W(SR)}\right)_{data} = \epsilon_{MC}\left(\frac{N_Z(SR)}{N_Z(CR)}\right)_{data} \quad (3.14)$$

$$\epsilon_{MC} = \left(\frac{N_W(SR)/N_W(CR)}{N_Z(SR)/N_Z(CR)}\right)_{MC} \quad (3.15)$$

where $N_W(CR)$ and $N_Z(CR)$ represent the number of W and Z candidates reconstructed in the low jet multiplicity control region and ϵ_{MC} is a Monte Carlo based corrections of the order of unity. $N_Z(SR)$ is the number of Z events which pass the same selection criteria as those imposed in the default cut-based analysis before the optimization. Figure 3.6 shows the W/Z ratio taken after event selection cuts, normalized the ratio to the 1 jet bin.

In figure 3.6, Z candidate events are selected (after the trigger) by requiring two same-flavour leptons of opposite charge, with an invariant mass between 80 and $100\ GeV$. The signal-like Z sample is then selected by applying the default cut-based analysis, *i.e.* three jets with p_T above $40\ GeV$ and a fourth with p_T greater than $20\ GeV$. The W candidates are selected by requiring exactly one charged electron (resp. muon), zero muons (resp. electrons) and missing transverse energy greater than $20\ GeV$. The control region is defined to have *exactly* one jet with pT greater than $20\ GeV$. With data driven methods and about $1\ fb^{-1}$ of luminosity, a 20% uncertainty on the W+jets normalisation should be reachable [24].

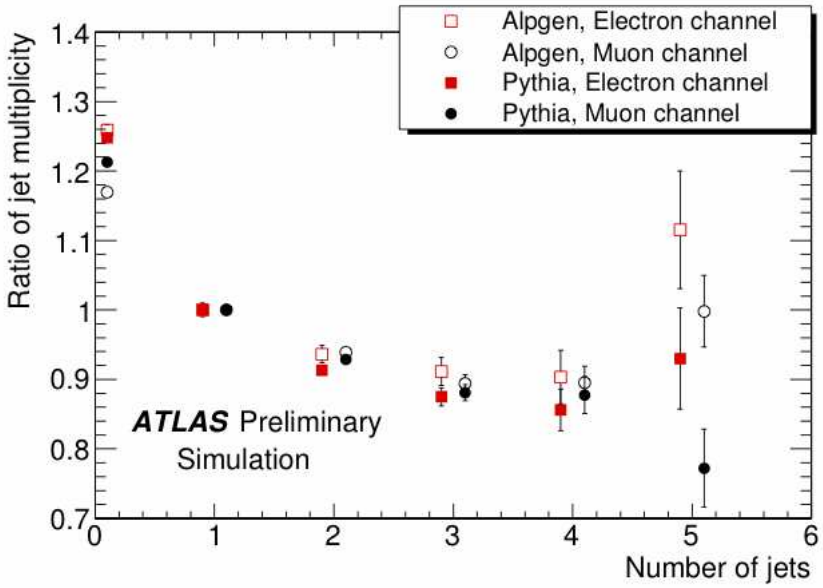

Figure 3.6: W/Z Ratio of reconstructed jet multiplicity for W and Z events as a function of jet multiplicity.

3.4.1 Determination of the W+jet background using the pseudo-data

In this section we will exercise the method introduced above in order to estimate the background in the $t\bar{t}$ selected sample using the pseudo-data themselves.

We define a *good muon* a reconstructed muon such that:

- is combined;
- has $p_T > 20\,GeV/c$;
- pseudorapidity in the range $|\eta| < 2.7$;
- is isolated: $E_{T,cone}(R = 0.3) < 6\,GeV$.

Similarly, a *good electron* is a reconstructed electron such that:

- is tight (see section 2.3);

- has $p_T > 20\,GeV/c$;
- pseudorapidity in the range $|\eta| < 2.5$, excluding the regions where $|\eta| \geq 1.37$ and $|\eta| \leq 1.52$;
- is isolated: $E_{T,cone}(R = 0.2) < 6\,GeV$.

The selections for the electron and muon channels require:

- the full trigger chain (mu20 for the muons and e20_loose for the electrons);
- for the Z selection: require exactly two good leptons (muon or electron) with invariant mass in a window around the Z_0 mass, $80 < |M_{ll}| < 100\,GeV$;
- for the W selection: require exactly one good lepton.

The Control Region (CR) of low jet multiplicity and the Signal Region (SR) then defined by the requirements:

- **CR**: exactly 1 reconstructed jet, with $p_T > 20\,GeV/c$;
- **SR**: at least 4 reconstructed jets, with p_T thresholds such that $p_{T,1} > 20\,GeV/c$, $p_{T,2} > 30\,GeV/c$, $p_{T,3} > 35\,GeV/c$ and $p_{T,4} > 45\,GeV/c$.

The jet finder used was AntiKt.4. The W+jet background in the SR is estimated through:

$$W_{SR} = \epsilon_{MC}\,(Z_{SR}/Z_{CR})_{\text{data}}$$

where the correction factor ϵ_{MC} is computed from Monte Carlo simulation:

$$\epsilon_{MC} = \frac{(W_{SR}/W_{CR})_{MC}}{(Z_{SR}/Z_{CR})_{MC}}$$

having indicated with $W_{CR,SR}$ and $Z_{CR,SR}$ the number of the W and Z candidates reconstructed in the control and signal region, respectively.

In figure 3.7 we report the result of the analysis for different sets of Monte Carlo samples (each set is a row of the table) and for the Z and W selections in the electron and muon analyses. The predictions are normalized to the

pseudo-data luminosity of $99\,pb^{-1}$. The last row of the table (QCDmu) represents a sample of QCD multi-jet events filtered by requiring the presence of a muon with $p_T > 10\,GeV/c$. This biased provides only a fraction of the QCD background; it is only reported here to show that the QCD background in the W selection in high.

The resulting correction factors are $\epsilon_{MC} = 1.01 \pm 0.03\,(stat)$ in the electron channel and $\epsilon_{MC} = 0.95 \pm 0.02\,(stat)$ in the muon channel, the average between the two $\epsilon_{MC} = 0.97 \pm 0.02\,(stat)$. Studies performed with other generators of W/Z+jet processes (not shown here) point to a systematic uncertainty on ϵ_{MC} of $\sim 12\%$. Other systematics due to the lepton and especially jet energy scales and the purity of control samples will bring the total systematic uncertainty to $\sim 20\%$.

The selections on the pseudo-data give:

- for the electron analysis: $W_{CR} = 86025$, $Z_{CR} = 4756$ and $Z_{SR} = 95$;
- for the muon analysis: $W_{CR} = 105114$, $Z_{CR} = 8160$ and $Z_{SR} = 149$.

Using these results and the average correction factor of 0.97 ± 0.02 we compute a background of 1665 ± 175 W+jet events in the electron sample (1731 ± 182 using the correction factor determined in the electron channel) and 1860 ± 157 in the muon sample (1821 ± 154).

The W+jet background determined from the pseudo-data is about 3.5% higer than the MC prediction in the electron channel and about 3% less in the muon channel. Using the ϵ_{MC} correction factors separately per each channel, instead of the average value, the estimate is about 8% higher than MC in the electron channel and about 5% less in the muon channel.

The statistical error (10.1% in the electron channel and 8.4% in the muon channel) and the systematic errors that we briefly discussed will allow the determination of the W+jet background at the $\sim 20\%$ level.

3.5 Cut optimization at $10\ TeV$

We performed a cut optimization by maximizing the statistical significance $\hat{S} \equiv S/\sqrt{S+B}$

	Electron Analysis				Muon Analysis			
	z->ee		w->enu		z->mumu		w->munu	
	CR	SR	CR	SR	CR	SR	CR	SR
Zee	5184	90	795	119	0	0	0	0
Zmumu	0	0	3	0	9033	167	3443	83
tautau	0	0	471	48	0	0	559	48
Wenu	1	0	88900	1498	0	0	4	0
Wmunu	0	0	10	1	0	0	106094	1785
Wtaunu	0	0	2887	110	0	0	3480	131
ttbar	3	3	128	2174	4	8	127	2442
sngltop	0	0	266	27	0	0	294	32
Wbb	0	0	47	30	0	0	53	35
WW	1	0	61	3	2	0	65	3
ZZ	5	1	4	1	7	2	3	1
WZ	7	2	9	3	11	4	9	3
QCDmu					0	0	6743	867

Figure 3.7: Result of the analysis for different sets of Monte Carlo samples (each set is a row of the table) and for the Z and W selections in the electron and muon analyses. The predictions are normalized to the pseudo-data luminosity of $99\,pb^{-1}$.

The statistical significance $\hat{S}$ varies with the integrated luminosity. Figure 3.8 shows the evolution of $\hat{S}$ with the integrated luminosity for a center of mass energy of $10\ TeV$. Systematic error linked to the uncertainty on W+jets Monte Carlo simulation is evaluated rising its luminosity by 20% and 50%.

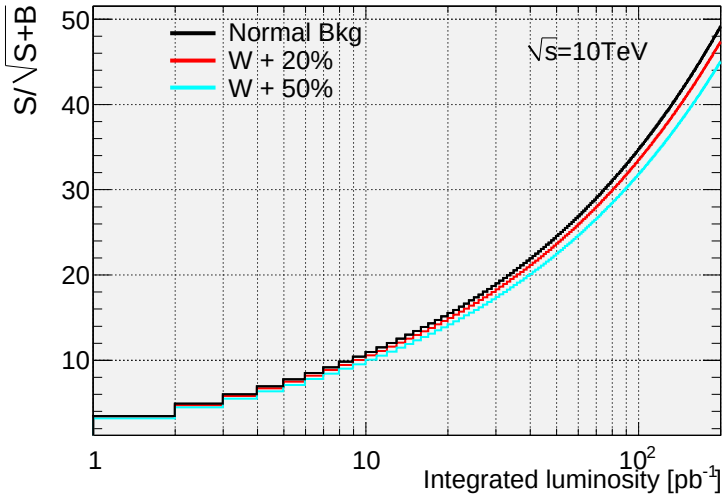

Figure 3.8: Statistical significance $S/\sqrt{S+B}$ as a function of integrated luminosity for $\sqrt{s} = 10\ TeV$.

In order to maximize statistical significance, a new scan in the parameters have been performed. The trigger and the one-lepton request, that define the channels, have been kept constant. Three separate scan in the parameters have been performed:

- E_T^{miss} from 0 to $100\ GeV$;
- Jet p_T threshold from 20(minimum) to $50\ GeV/c$
- e/μ isolation cut from 1 up to $10\ GeV$

We assume a reference integrated luminosity of 200 pb^{-1} .

3.5.1 Scan in E_T^{miss}

Scan in E_T^{miss} has been performed varying the threshold from 0 to $100\ GeV$. Figure 3.9 shows the number of events for signal and the background from

W+jets events (on the left) for the electron (upper row) and muon (lower row) channels. On the right it is plotted the evolution of statistical significance $S/\sqrt{S+B}$ with respect to the value of the threshold on transverse missing energy. The cut on E_T^{miss} , effective to reject the QCD multi-jet background, corresponds to a significance $\hat{S} \sim 34$ for an integrated luminosity of $200\ pb^{-1}$. The systematic error due to the threshold set on minimum E_T^{miss} will be shown in section 3.9.6.

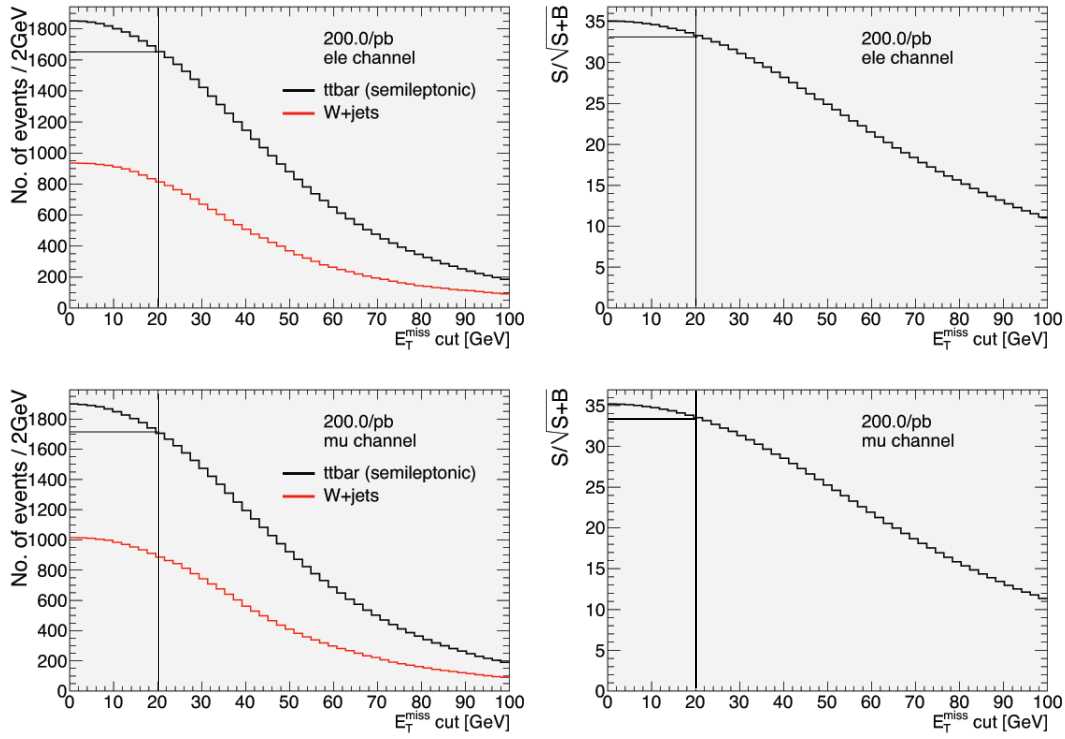

Figure 3.9: Scan in E_T^{miss} cut for electron (top) and muon (bottom) channels. Signal and background events (left) and significance $S/\sqrt{S+B}$ (right).

3.5.2 Scan in jet minimum transverse momentum

In benchmark analysis, events are required to have at least 3 AntiKt D=0.4 jets with p_T greater than $40\ GeV/c$ plus an additional jet with $p_T > 20\ GeV/c$. In fact, in the candidate events, three of the reconstructed jets are expected to have originated from a top quark which has decayed hadronically. Using

events generated at $10\ TeV$, we plotted the number of jets in a given event with a p_T greater than a certain threshold. Sliding this threshold from 0 to $100\ GeV/c$, one can obtain informations on how many jets are expected with a certain minimum p_T. Most of $t\bar{t}$ events with exactly one isolated lepton (figure 3.10, on the left) have 4 jets with $p_T \geq 20\ GeV/c$, 3 jets with $20 \leq p_T \leq 40\ GeV/c$ and 2 jets with $40 \leq p_T \leq 70\ GeV/c$. Instead, most of W+jets events (figure 3.10, on the right) have 2 jets with $p_T \leq 40\ GeV/c$ or just one jet with $p_T \geq 30\ GeV/c$. Very few background events have 4 jets.

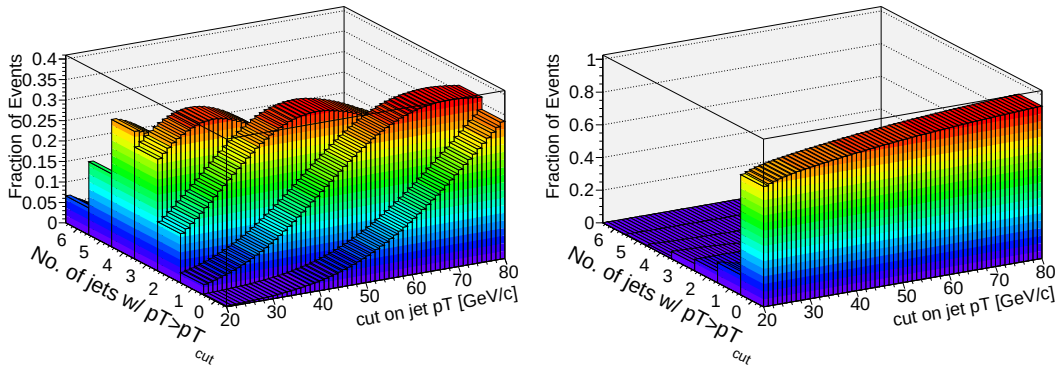

Figure 3.10: Integral of number of jets with $p_T \geq p_T^{min}$ for $t\bar{t}$ events (left) and W+jets background (right).

In order to optimize the cut on jet transverse momentum, a scan in minimum jet p_T has been performed as follows:

- Fourth leading jet p_T threshold $p_{T\ cut}^{(}4)$: $20 \leq p_{T\ cut}^{(}4) \leq 50\ GeV/c$;
- Third leading jet p_T threshold $p_{T\ cut}^{(}3)$: $p_{T\ cut}^{(}4) \leq p_{T\ cut}^{(}3) \leq 50\ GeV/c$;
- Second leading jet p_T threshold $p_{T\ cut}^{(}2)$: $p_{T\ cut}^{(}3) \leq p_{T\ cut}^{(}2) \leq 50\ GeV/c$;
- Leading jet p_T threshold $p_{T\ cut}^{(}1)$: $p_{T\ cut}^{(}2) \leq p_{T\ cut}^{(}1) \leq 50\ GeV/c$;

All these itereations has been done in steps of $5\ GeV/c$.

The best combination that maximizes the statistical significance is:

- Fourth leading jet $p_T > 20\ GeV/c$;
- Third leading jet $p_T > 30\ GeV/c$;

- Second leading jet $p_T > 35\ GeV/c$;
- Leading jet $p_T > 45\ GeV/c$.

Which yields $S/\sqrt{S+B} = 49$ for the muon channel and 46.5 for the electron channel, for $200\ pb^{-1}$ of data taken at $\sqrt{s} = 10\ TeV$.

3.5.3 Scan in lepton isolation

In this $t\bar{t}$ analysis, most of the leptons from background are isolated leptons, coming from the decay of vector bosons. If these leptons are correctly reconstructed, one expects that the statistical significance depends only very loosely on the cut applied on isolation. In order to check this assumption, a scan the transverse energy in a cone $\Delta R < 0.2$ around the lepton axis has been performed, ranging from a tight isolation of $1\ GeV$ to a loose isolation of $\leq 10\ GeV$. Figure 3.11 shows that the isolation of most of the electrons (left) and muons (right) reconstructed in $t\bar{t}$ semi-leptonic events lies below this value.

The same cannot be said for electrons coming from QCD and $t\bar{t}$ full-hadronic decays: in fact most of the leptons appearing in such events are *not* isolated and these requirements are effective in rejecting these backgrounds.

Figure 3.12 shows how statistical significance changes for different values of leptons isolation. As can be seen, for both channels the significance rises steeply and saturates for an isolation of $6\ GeV$ for electrons and $3\ GeV$ for muons.

3.6 The Cut-based Analysis with Optimized Cuts

Analysis with optimized jet p_T thresholds has been applied to the same samples of the benchmark analysis. The selections are:

- **Electron Channel**
  1. Trigger EF_e20_loose
  2. Exactly one tight electron with $p_T > 20\ GeV/c$ and $|\eta| < 2.5$
  3. $E_T^{miss} > 20\ GeV$

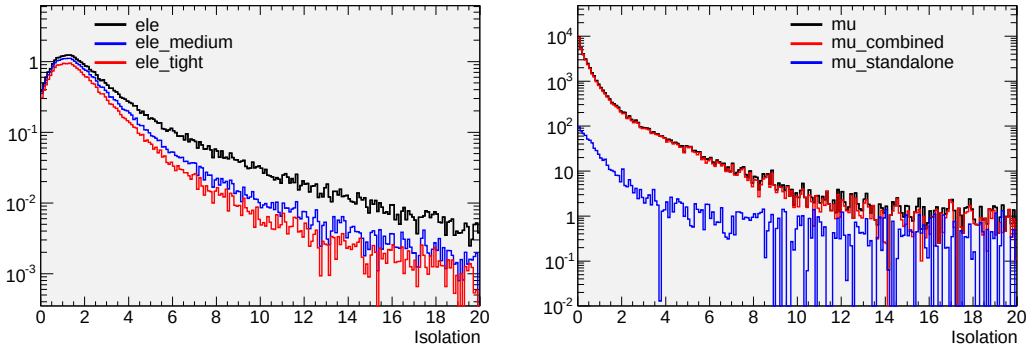

Figure 3.11: Isolation for electrons (left) and muon (right) in $t\bar{t}$ semi-leptonic events.

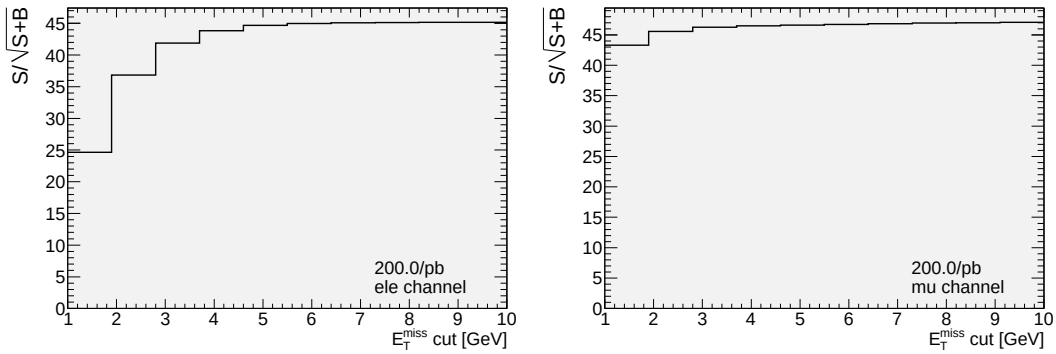

Figure 3.12: Variation of the statistical significance $S/\sqrt{S+B}$ with isolation cut on electrons (left) and muons (right).

4. At least 4 jets with $p_T > 20\ GeV/c$ and $|\eta| < 2.5$
5. $p_T^{(4)} > 20\ GeV/c$, $p_T^{(3)} > 30\ GeV/c$, $p_T^{(2)} > 35\ GeV/c$ and $p_T^{(1)} > 45\ GeV/c$

- **Muon Channel**

1. Trigger EF_mu20
2. Exactly one STACO combined muon with $p_T > 20\ GeV/c$ and $|\eta| < 2.7$
3. $E_T^{miss} > 20\ GeV$
4. At least 4 jets with $p_T > 20\ GeV/c$ and $|\eta| < 2.5$
5. $p_T^{(4)} > 20\ GeV/c$, $p_T^{(3)} > 30\ GeV/c$, $p_T^{(2)} > 35\ GeV/c$ and $p_T^{(1)} > 45\ GeV/c$

Events passing each level of the selection are shown in tables 3.6 and 3.6 for the muon and electron channels respectively. The measured cross-sections are $424.0 \pm 12(stat)\ pb$ for the muon channel and $453.0 \pm 12(stat)\ pb$ for the electron channel.

Dataset	Tot	Trig	S.L.	E_T^{miss}	4 jets	jet p_T cut	m_t	m_W
Pseudo-data	1165384	792420	704672	633009	6448	4744	4509	3137
tT no fullHad	21430	6110	4379	3980	2626	2343	2253	1698
W+jets	4788045	744892	708862	654882	3164	1802	1691	1052
Single top	10380	2548	2082	1863	355	274	255	174
Z+jets	436563	105215	48901	25638	215	128	120	73
tT fullHad	13309	545	13	5	4	4	4	3
Di-boson	1195	421	227	181	9	6	5	3
Wbb	1759	355	306	266	46	33	31	19
All	5251251	853979	760393	682837	3795	2249	2109	1326

Table 3.5: Cut flow with optimized selection cuts for an integrated luminosity of 99 pb^{-1} at 10 TeV. Muon Channel.

3.7 The Cut-Based Analysis for $\sqrt{s} = 7\ TeV$

The LHC will start its operations at the center-of-mass energy $\sqrt{s} = 7\ TeV$. The kinematic properties of $t\bar{t}$ and background events should not differ too much

Dataset	Tot	Trig	S.L.	E_T^{miss}	4 jets	jet p_T cut	m_t	m_W
Pseudo-data	1569114	888719	622398	523284	6107	4531	4276	2974
tT no fullHad	21430	6675	4078	3700	2430	2166	2080	1561
W+jets	4788045	840842	608845	557723	2806	1598	1499	948
Single top	10380	2867	1944	1732	344	267	248	171
Z+jets	436563	113069	59796	4005	247	164	152	94
tT fullHad	13309	405	8	2	2	2	2	1
Di-boson	1195	473	221	159	8	6	5	3
Wbb	1759	392	268	234	41	29	27	16
All	5251251	958050	671085	563858	3451	2067	1935	1236

Table 3.6: Cut flow with optimized selection cuts for an integrated luminosity of 99 pb^{-1} at 10 TeV. Electron Channel.

going from 10 to 7 TeV. However, we repeated the optimization procedure to check this hypothesis. We used the same Monte Carlo datasets generated at $\sqrt{s} = 10\ TeV$ reweighting the parton kinematics to the target energy of $\sqrt{s} = 7\ TeV$. This is an approximation, but we cross-checked with some samples generated at $\sqrt{s} = 7\ TeV$ that the distributions are in good agreement.

3.7.1 PDF Reweighting Method from $10\ TeV$ to $7\ TeV$

All the dataset used in this work have been produced for a center of mass energy $\sqrt{s} = 10\ TeV$, according to LHC's schedule at the beginning of 2009. Unfortunately, due to technical reason, this important parameter suffered a shift from $10\ TeV$ to 7 TeV. The Monte Carlo group of the Atlas collaboration decided not to reproduce all the datasets, but to keep them as-is and provide a tool to adapt generated events to a target $\sqrt{s}$ by re-weighting the parton distribution functions (PDF).

3.7.1.1 Reweighting procedure

The hadronic cross-section is given by:

$$\sigma = \sum_{flav,i} \int_0^1 dx_1 dx_2 f_{PDF}(x_1, q_1, Q^2) f_{PDF}(x_2, q_2, Q^2) \times \hat{\sigma}_{hard}(p_1, p_2, \alpha_s(Q^2), Q^2) \tag{3.16}$$

Where the sum runs over all flavours i, x_i is the momentum fraction carried by the parton q_i, Q^2 is the energy scale of the interaction, $\hat{\sigma}_{hard}$ is the cross-section of the hard process.

In order to re-weight the event to a new $\sqrt{s}$, one has to change the probability that such a kinematic configuration can occour at the reference $\sqrt{s}$, *i.e.* to "re-weight" the parton density function. Thus, a new weight is calculated on an event-by-event basis:

$$w = \frac{f_{PDF}(x_1', q_1, Q^2) \times f_{PDF}(x_2', q_1, Q^2)}{f_{PDF}(x_1, q_1, Q^2) \times f_{PDF}(x_2, q_2, Q^2)} \tag{3.17}$$

Where x_i' is the momentum fraction carried by the parton q_i at $7\ TeV$. Equations 1.4 describe how x_1 and x_2 vary *w.r.t.* the center-of-mass energy $\sqrt{s}$.

3.7.2 Cut optimization

The same scan in jet p_T as shown in section 3.5.2 has been performed using this time the same events, reweighted for a center of mass energy $\sqrt{s} = 7\ TeV$. As a result, the same set of cuts maximizes statistical significance yielding $S/\sqrt{S+B} = 29.5$ for the muon channel and $S/\sqrt{S+B} = 28$ for the electron channel, for $200\ pb^{-1}$ of data. Figure 3.13 shows the evolution of $\hat{S}$ with the integrated luminosity.

3.8 Reconstruction of the Top Quark in the Hadronic Decay Branch

Top quark invariant masses can be reconstructed from jets in selected events. There is not a unique way to pick up the three jets that come from the hadronically-decayed top quark for a commissioning analysis which won't make use of b-tagging. The top quark is reconstructed assuming that it originates from the three-jet combination whose four-momentums' sum has the highest-p_T. Implicitly, it is assumed that two out of three jets come from the W boson, and the third is actually a b jet. The jet-jet combination used to reconstruct the W boson is the one with minimal $\Delta R = \sqrt{\Delta\eta^2 + \Delta\phi^2}$. It has been proved [16] that this selection picks up the correct combination 35% of the times. This

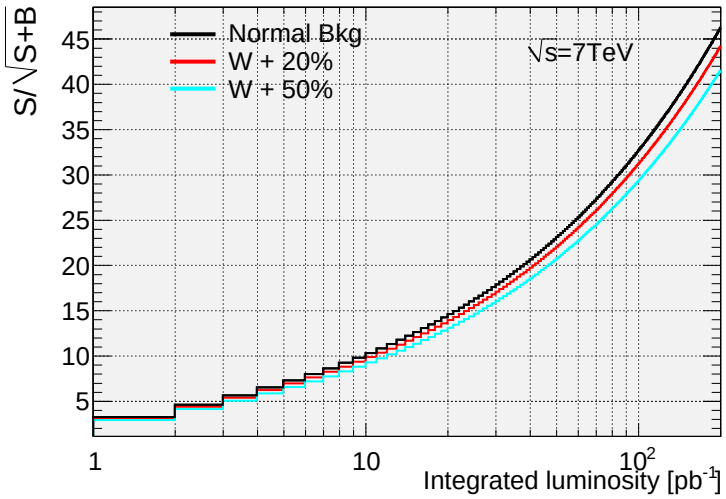

Figure 3.13: Statistical significance .

feature can be thus exploited to apply the so-called "W mass window cut": one asks that the reconstructed hadronic W mass is within a certain window ($\sim 10\ GeV$) around the PDG value, $80.403 \pm 0.029\ GeV$ [33]. As can be seen in figures 3.14, the overall effect is to reduce the background in the high-mass tail of the top mass distribution.

Figure 3.14 shows the reconstructed hadronic top invariant masses, transverse momentum and pseudorapidity distributions for the electron and muon channels at optimal cut points. Comparison is made against pseudo-data samples for an integrated luminosity of 99 pb^{-1} . A slight excess of data over MC is observed and can be accounted to a normalization of the MC samples composing the pseudo-data scaled by a factor not equal to unity.

3.9 Systematic Uncertainties on the Cross-Section

3.9.1 Systematic Uncertainty due to Jet Energy Scale

The uncertainty with which the jet energy is measured affects the accuracy of the cross-section measurement. This jet energy scale (JES) uncertainty is evaluated considering a shift of $\pm 10\%$ (pessimistic scenario) and $\pm 3\%$ (optimistic

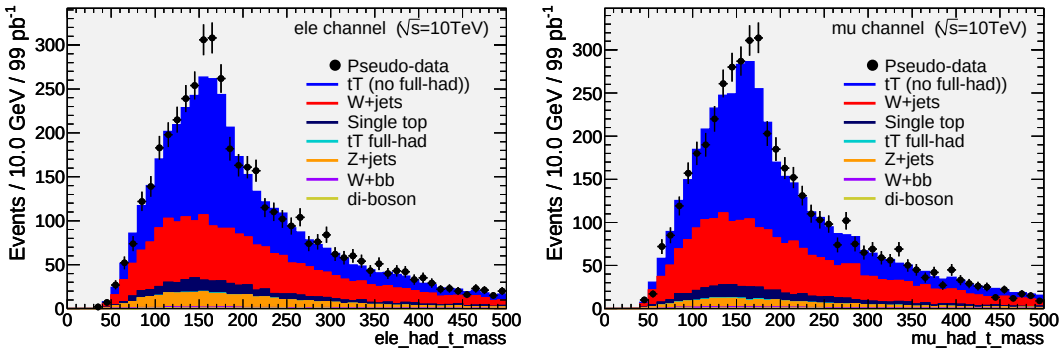

(a) Hadronic top mass

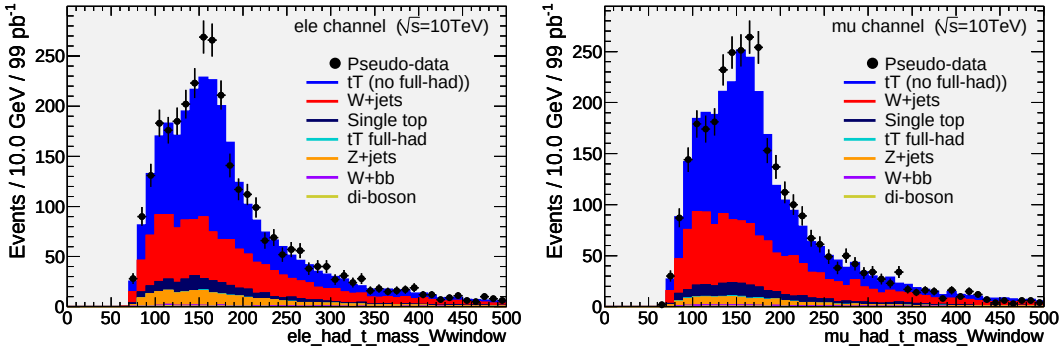

(b) Hadronic top mass with m_W window cut

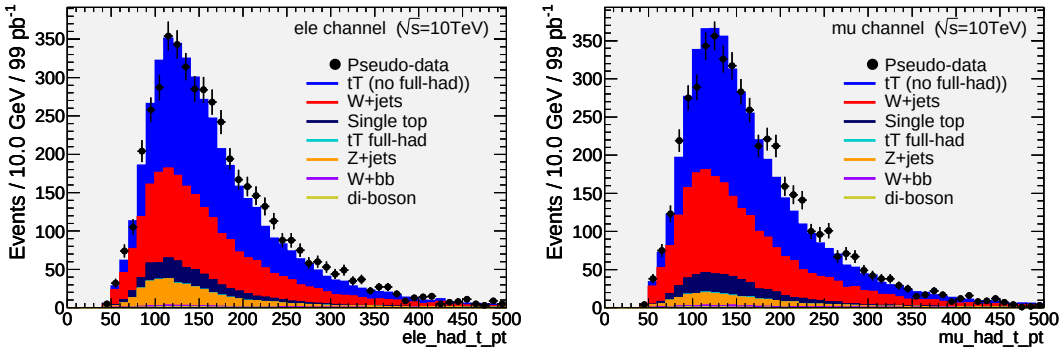

(c) Hadronic top p_T

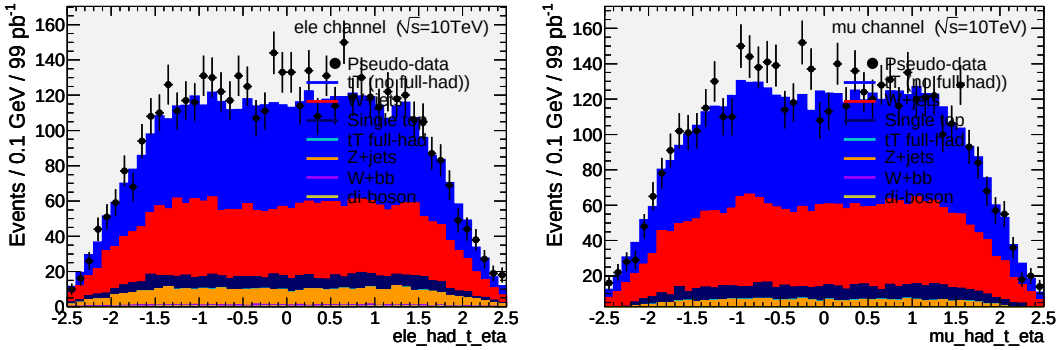

(d) Hadronic top pseudorapidity

Figure 3.14: Reconstructed hadronic $t\bar{t}$ in the electron (left) and muon (right) channels.

scenario). The error associated to the cross-section is:

$$\frac{\Delta\sigma_{t\bar{t}}}{\sigma_{t\bar{t}}} = \frac{N'_{sig} + N'_{bkg} - (N_{sig} + N_{bkg})}{N_{sig} - N_{bkg}} \tag{3.18}$$

Where N'_{sig} and N'_{bkg} are the number of signal and background events respectively after JES rescaling. Tables 3.9.1 and 3.9.1 show this effect for muon and electron channel respectively.

The agreement between pseudo-data and MC is actually less than 3%. We expect an uncertainty of 5-10% with first real data.

JES (%)	$N_{obs} - N_{bkg}$	N_{bkg}	$\epsilon_{sig}^{(MC)}$ (%)	$S/\sqrt{S+B}$	$\sigma_{t\bar{t}}$ [pb]	$\Delta\sigma_{t\bar{t}}\ /\sigma_{t\bar{t}}$
-10	3010	1520	8.8	44.73	633.1	+39.7
-5	2751	1779	9.5	40.88	538.2	+18.7
-4	2695	1835	9.6	40.05	520.2	+14.8
-3	2642	1888	9.8	39.26	503.5	+11.1
-2	2583	1947	9.9	38.38	486.2	+7.2
-1	2518	2012	10.0	37.42	468.2	+3.3
0	2463	2067	10.1	36.59	453.2	
+1	2400	2130	10.2	35.67	436.7	-3.7
+2	2339	2191	10.3	34.75	420.6	-7.2
+3	2277	2253	10.5	33.84	405.2	-10.6
+4	2210	2320	10.6	32.84	389.4	-14.1
+5	2143	2387	10.7	31.85	373.7	-17.5
+10	1787	2743	11.2	26.55	297.5	- 34.6

Table 3.7: Variation of cross-section measured from pseudo-data with jet energy scale. Electron channel.

3.9.2 Systematic Uncertainty due to Jet Reconstruction Algorithm

Two algorithms have been compared: AntiKt4 used in the reference analysis and Cone4, both applied to tower jets. The effect is not negligible and evaluated to be 9% for the muon channel and 7% for the electron channel. This is shown in tables 3.9.2 and 3.9.2.

JES (%)	$N_{obs} - N_{bkg}$	N_{bkg}	$\epsilon_{sig}^{(MC)}$ (%)	$S/\sqrt{S+B}$	$\sigma_{t\bar{t}}$ [pb]	$\Delta\sigma_{t\bar{t}}/\sigma_{t\bar{t}}$
-10	3105	1638	9.6	45.08	599.2	+41.2
-5	2810	1933	10.3	40.80	506.1	+19.3
-4	2749	1994	10.4	39.92	489.5	+15.3
-3	2684	2059	10.6	38.98	472.0	+11.2
-2	2624	2119	10.7	38.10	456.5	+7.7
-1	2562	2181	10.8	37.20	440.8	+3.9
0	2494	2249	10.9	36.22	424.4	
+1	2423	2320	11.0	35.18	408.0	-3.8
+2	2355	2388	11.2	34.20	393.0	-7.4
+3	2291	2452	11.2	33.27	379.1	-10.6
+4	2221	2522	11.3	33.25	364.2	-14.2
+5	2152	2591	11.4	31.25	349.8	-17.6
+10	1776	2967	11.9	25.80	277.5	-34.6

Table 3.8: Variation of cross-section measured from pseudo-data with jet energy scale. Muon channel.

Algorithm	N_{obs}	N_{bkg}	$\epsilon_{sig}^{(MC)}$	$\epsilon_{bkg}^{(MC)}$ (%)	σ [pb]
AntiKt4	4744	2249	10.94%	0.04%	424.4
Cone4	4036	1601	9.79%	0.04%	462.5

Table 3.9: Systematic uncertainty due to chosen jet reconstruction algorithm for the muon channel.

Algorithm	N_{obs}	N_{bkg}	$\epsilon_{sig}^{(MC)}$	$\epsilon_{bkg}^{(MC)}$ (%)	σ [pb]
AntiKt4	4531	2067	10.11%	0.04%	453.2
Cone4@NLO	3804	1459	8.99%	0.04%	485.2

Table 3.10: Systematic uncertainty due to chosen jet reconstruction algorithm for the electron channel.

3.9.3 Systematic Uncertainty due to Monte Carlo Generator for Signal and Background

Another source of uncertainty from Monte Carlo comes from the possibility to use different event generators. In order to evaluate this systematic uncertainty, the same cut flow has been applied to a sample generated with MC@NLO, processed by the Atlas full-simulator as well. This systematic uncertainty has been evaluated to be ∼3% for both channels.

3.9.4 Systematic Uncertainty due to Luminosity Measurement

An uncertainty of 15% on the integrated luminosity is assumed for the early data-taking period. We make the simplification that the uncertainty in the luminosity is multiplicative on the cross-section. Once data-driven methods will be used for the evaluation of the background (which do not depend on the luminosity) this assumption will not be longer true. Data-driven methods are not affected by this kind of uncertainty. The error due to the integrated luminosity is:

$$\Delta\sigma_{t\bar{t}}^{(lumi)} = \frac{\partial\sigma}{\partial\mathcal{L}}\Delta\mathcal{L} = \frac{N_{obs} - N_{bkg}}{\epsilon \times \mathcal{L}^2 \times \mathcal{BR}}\Delta\mathcal{L} \tag{3.19}$$

For $99\ pb^{-1}$ taken at $10\ TeV$, the cross section calculated from pseudo-data is this $424.0 \pm 64.0\ pb$ for the muon channel and $453.0 \pm 68.0\ pb$ for the electron channel.

Figure 3.15 shows the instantaneous luminosity determined by three independent methods for run 142193, taken by ATLAS on Dec 12, 2009. This run offered an extended stable-beam period of 4.5 hours, thus allowing ATLAS to measure the instantaneous luminosity for varying beam intensities. The blue dots show the result from the dedicated forward luminosity detector LUCID [14]. The small black dots (shaded band) give the results obtained from the Minimum Bias Trigger Scintillator [3] (MBTS) Level-1 trigger rates (see upper plot for details), using as inputs to the luminosity calculation the expected minimum bias cross section at 900 GeV (Pythia numbers: $34.4\ mb$, $11.7\ mb$, $6.4\ mb$ for non-diffractive, single-diffractive and double-diffractive collisions, respectively), and the MBTS efficiency determined from data and MC to be ap-

proximately 85%. Backgrounds between 1% and 20%, depending on the run conditions, have been subtracted. Finally, the red dots show the results obtained from counting events that have deposited energy in both Liquid-Argon calorimeter endcaps, with arrival times consistent with particles originating from the interaction point. Background from unpaired bunches is negligible. The selection efficiency is estimated from MC to be 55%. The overall systematic uncertainty in the absolute scale of these three determinations is estimated to be up to 30%. The short drop of luminosity at around 14:15 is due to a trigger inhibit issued when ramping up the Silicon detectors after reception of the stable-beams signal.

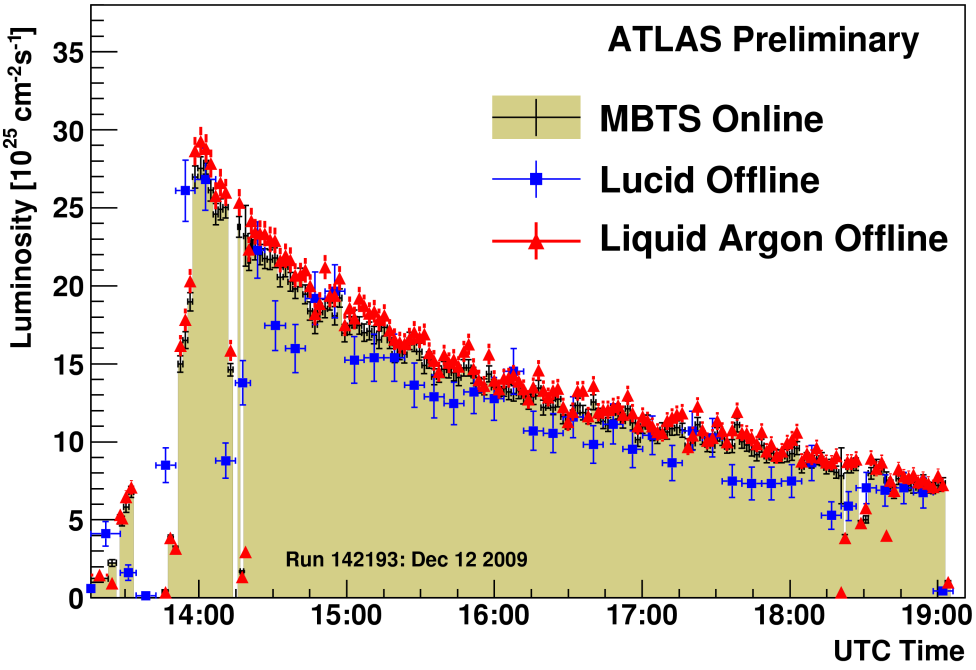

Figure 3.15: Instantaneous luminosity determined by three independent methods for run 142193, taken by ATLAS on Dec 12, 2009. The blue dots show the result from the dedicated forward luminosity detector LUCID. The small black dots (shaded band) give the results obtained from the Minimum Bias Trigger Scintillator (MBTS) Level-1 trigger rates (see upper plot for details), using as inputs to the luminosity calculation the expected minimum bias cross section at 900 GeV.

3.9.5 Stability of the analysis with respect to m_W window cut

In order to reduce combinatorial background on the tail of the hadronic top mass distribution, it is possible to require that at least two jets out of the three assigned to form the reconstructed hadronic top must have an invariant mass within a certain value from the nominal mass of the W boson. Reconstructed hadronic W boson mass and transverse momentum are shown in figure 3.16 for the electron and muon channels, for the pseudo-data and Monte Carlo.

This "window" is usually set to $20\ GeV$. We varied the $|m_W - m_{jj}|$ window from 10 to $30\ GeV$. Table 3.9.5 shows that once this cut is applied, the variation on the cross-section is about -2% for the electron channel and negligible for the muon channel. The overall effect is smaller than -3% for the electron channel and smaller than -1% for the muon channel. this uncertainty is about 1% for the electron channel and less than 1% for the muon channel.

$\|m_W - m_{jj}\|$	$\sigma(e)$		$\sigma(\mu)$	
Not applied	453.2		424.4	
10 GeV	438.3	-3.3%	423.9	-0.12%
20 GeV	443.5	-2.14%	424.8	+0.09%
30 GeV	447.4	-1.28%	419.6	-1.13%

Table 3.11: Uncertainty due to $|m_W - m_{jj}|$ cut.

3.9.6 Stability of the analysis with respect to Cut on E_T^{miss}

In order to study the sensitivity of the measurement associated with the cut on E_T^{miss} , we raised this value to $30\ GeV$. Even if the QCD background if not included in the pseudo-data, it is known that the large majority of QCD multi-jet background events do not survive such a tight cut (see figure 3.4 for a MC-based estimate). Tables 3.9.6 and 3.9.6 show the variation for the electron and muon channel respectively. The difference has been evaluated to be 2.0% for the electron channel and 1.2% for the muon channel.

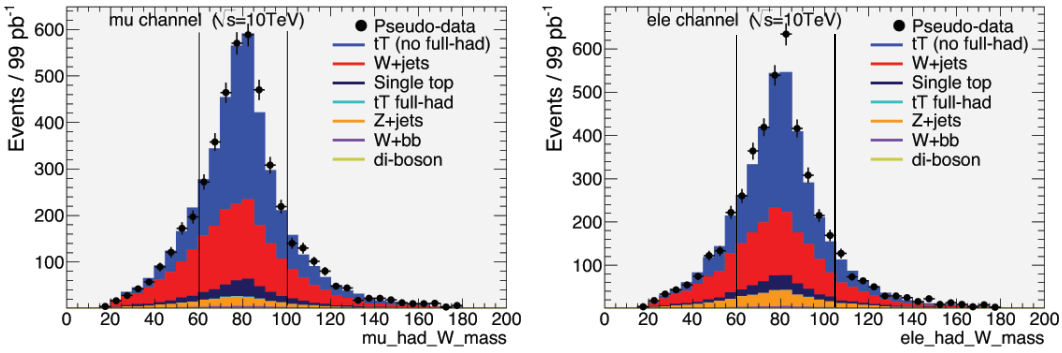

(a) Mass

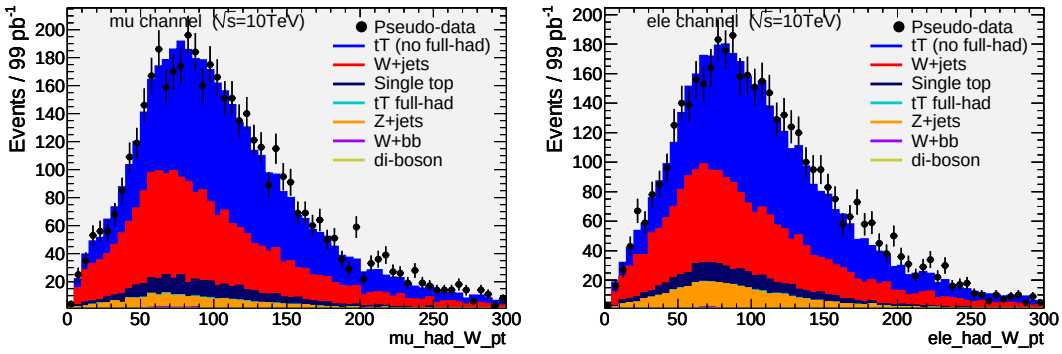

(b) Transverse momentum

Figure 3.16: Mass (upper row) and transverse momentum (lower row) distribution of the reconstructed hadronic W boson in the electron (left) and muon (right) channels.

Threshold on E_T^{miss} [GeV]	N_{obs}	N_{bkg}	$\epsilon_{sig}^{(MC)}$	$\epsilon_{bkg}^{(MC)}$ (%)	σ [pb]
20.	4531	2067	10.11%	0.04%	453.2
30.	3854	1658	8.84%	0.03%	462.3

Table 3.12: Systematic uncertainty due to chosen jet reconstruction algorithm for the muon channel.

Threshold on E_T^{miss} [GeV]	N_{obs}	N_{bkg}	$\epsilon_{sig}^{(MC)}$	$\epsilon_{bkg}^{(MC)}$ (%)	σ [pb]
20.	4744	2249	10.94%	0.04%	424.4
30.	4093	1871	9.62%	0.04%	429.6

Table 3.13: Systematic uncertainty due to chosen jet reconstruction algorithm for the electron channel.

3.10 Combination of Electron and Muon Channels Using a Bayesian Approach

Imagine that x is a variable that we believe is distributed according to a model defined by a set of parameters $\theta = (\theta_1, \theta_2, ..., \theta_M)$. Suppose we have a prior belief about the *true* values of θ described by a prior distribution $p(\theta)$. Then, according to the Bayes' theorem, the updated distribution of θ, given a set of observations $x = (x_1, x_2, ..., x_N)$ is given by:

$$p(\theta|x) = \frac{p(x|\theta)p(\theta)}{p(x)}\,, \tag{3.20}$$

where $p(A|B)$ indicates the conditional probability of A given the occurrence of B. The term $L(\theta) \equiv p(x|\theta)$ is known as the *likelihood* function of θ. The normalization term $p(x)$ comes from the *marginalization* over θ:

$$p(x) = \int dx p(x|\theta)p(\theta)\,. \tag{3.21}$$

The important point is that the Bayesian analysis provides the entire *posterior distribution* of θ rather than a single value estimate as in the classical approach. As our knowledge improves with more data, the posterior distribution becomes more and more peaked around a set of values of the model parameters. If there is no prior knowledge (for example the prior is flat over a physically admittable region of the parameters) the Bayesian analysis is equivalent to the classical *maximum likelihood* approach.

This approach can also be used for the combination of measurements that come from different experiments, of form different channels in the same experiment. The output of the procedure is a probability distribution for the measured values that improves the single measurements and takes into account the uncorrelated and correlated errors. From this probability distributions one can make *"inferences"* about the combined values, in terms of means, medians, standard deviations ect.

3.10.1 Combination of measurements

We can consider the likelihood as a function of the true values x and the systematic parameters s (also known as nuisance parameters):

$$L = p(y|x, s).$$

Using the Bayes theorem the joint probability density of x and s given the measurements y is:

$$f(x, s|y) \propto p(y|x, s)g_0(x)f_0(s),$$

where f_0 and g_0 are the prior densities. The probability density for a given x_i is obtained through the marginalization over the other variables.

The measurements are estimates of the true values x_i with an associated error: $y_i \pm \epsilon_i$. The dependence of the likelihood on the systematic s can be viewed as a dependence of the best estimates on s: $y_i(s)$. Let us introduce the parameter $\delta_i \equiv (s_i - s_i^0)/\sigma_i$, where σ_i is the standard deviation of $s_i - s_i^0$, so that linearising around the nominal s_i^0:

$$y_i(s_i) = y_i(s_i^0) + \sum_k \left.\frac{\partial y_i}{\partial s_k}\right|_{s_k^0} (s_k - s_k^0) = y_i + \sum_k \frac{\partial y_i}{\partial \delta_k}\,\delta_k \equiv \hat{x}_i\,.$$

As an example, in case of gaussian uncertainties ($-\log L = \sum_i \frac{1}{2}(\frac{\hat{y}_i - y_i}{\sigma_i})^2$) with gaussian systematics ($-\log f_0(s) = \sum_i \frac{1}{2}\delta_i^2$) and a flat prior for the true values x_i ($g_0(x_i)$ =const.) the posterior is given by:

$$-\log f(x, \delta) = \left[\sum_i \frac{1}{2}\left(\frac{y_i + \sum_k \frac{\partial y_i}{\partial \delta_k}\delta_k - x_i}{\sigma_i}\right)^2 + \sum_k \frac{1}{2}\delta_k^2\right].$$

The priors for the sytematics are however not forced to be gaussian, and there can also be non-linear dependences of the measurements y on the systematics. In case of asymmetric errors one can use different approximations, like two lines with different slopes for $\delta > 0$ and $\delta < 0$, or a quadratic approximation with a parabola passing through zero and through the positive and

negative variations.

In summary, in the bayesian approach one gets the full pdf of the true x-values, via the marginalization over the δ parameters.

3.10.2 Combination of the electron and muon channels

We followed the approach described in the previous section to combine the $t\bar{t}$ cross sections measured in the semileptonic electron and muon channels. The marginalization over the nuisance parameters was performed using a Markov Monte Carlo Chain (MCMC) approach [50] as implemented in the package `Combine` [26] integrated in the *Bayesian Analysis Toolkit* (BAT) [21].

This program offers a broad set of options, the most important being:

- definition of the parameters to be inferred, specifying a starting value and a range of variability; in our case the inference is on one parameter only, e.g. the cross section.

- Definition of the nuisance parameters (the systematics), specifying their range of variability and the shape of the corresponding prior (three options are implemented: uniform, gaussian and triangular).

- Specification of the dependence of the data points on the systematic (symmetric, asymmetric with a quadratic approximation; asymmetric with linear dependece on the right and left sides; symmetrized with or without the shift of the data points).

The systematics that we are going to consider are the ones discussed in the previous sections. They are summarized in table 3.10.2.

Other systematics are not considered in this preliminary analysis. The uncertainties linked to the lepton identification and trigger efficiencies are expected to be small ($\sim 1-2\%$), while other, like the effects of the parton distribution functions and the modelling of the ISR and FSR, known to be more important, have not yet been completely evaluated. The effect of the luminosity variation was assumed to be symmetric, even if the use of data-driven methods to evaluate the W+jet background, independent on the luminosity, breaks the symmetry.

Source	Electron Channel $\Delta\sigma/\sigma$	Muon Channel $\Delta\sigma/\sigma$
Statistics	2.8%	2.7%
JES +3%	-10.6%	-10.6%
JES -3%	+11.1%	+11.2%
$t\bar{t}$ MC Generator	+2.3%	+2.7%
Jet Algorithm	+7%	+9%
W+jets -20%	+10.4%	+10.4%
W+jets +20%	-17.1%	-16.1%
Luminosity $\pm$15%	$\pm$ 15%	$\pm$ 15%

Table 3.14: Summary of all systematic uncertainty studied in this work for an integrated luminosity of 99 pb^{-1} taken at $\sqrt{s} = 10\ TeV$. Statistical uncertainty is quoted for reference.

We combined the cross sections measured in the electron and muon channels using a parabolic approximation for the asymmetric systematics. In fig. 3.17 we show the probability density of the "true" cross section after the marginalization over the systematics, with three different treatments of the variations due to the change of the Monte Carlo signal generator and the jet algorithm. The diamond represents the most probable value and the red triangle represents the median of the distribution. In the first case (Fig. 3.17 (a)) the systematics were considered to be half-gaussian in the positive direction; in the second case (Fig. 3.17 (b)) they were considered gaussians and were symmetrized with a shift of the input cross sections. Finally, in Fig. 3.17 (c), a uniform distribution between the two models or methods was implemented. The results are perfectly compatible. Quoting the median values with the "error" corresponding to a variation from the median to the 16% and 84% quantiles, one gets in the three cases $\sigma^{med} = 431^{+97}_{-79}\,pb$, $\sigma^{med} = 452^{+98}_{-84}\,pb$ and $\sigma^{med} = 447^{+86}_{-69}\,pb$, respectively.

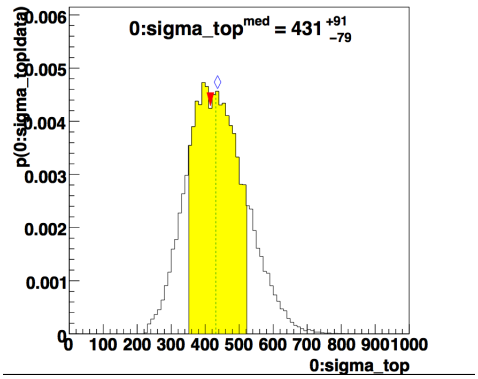

(a) Half-gaussian errors in the positive direction

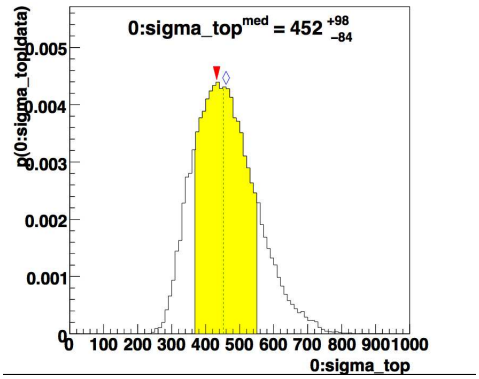

(b) Symmetric gaussian errors with shift in the input cross-sections

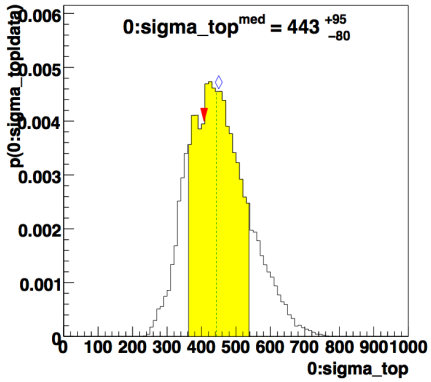

(c) Uniformly distributed errors

Figure 3.17: Results of combination of the two channels with `Combine`. PDF of the "true" cross section after the marginalization over the systematics, with three different treatments of the variations due to the change of the Monte Carlo signal generator and the jet algorithm. The diamond represents the most probable value and the red triangle represents the median of the distribution.

Conclusions

The ATLAS detector is ready to observe proton-proton interactions, and this thesis is about the observation of top quark pairs that decay into a charged lepton, a neutrino and four jets. This "golden" channel has been deployed successfully for years at the Tevatron, yielding very precise measurements of their properties at an energy range well below the capabilities of the Large Hadron Collider. When the center-of-mass energy will reach $\sqrt{s} = 14\,TeV$, top quark pairs will be produced copiously at the LHC thanks to their production cross-section of $\sim 850\,pb$, making it almost the first top factory in history.

Within few months $\sim 100\,pb^{-1}$ of data can be collected and analyzed. They will provide enough statistics to overcome statistical errors and keep under control the main background given by W+jets events. Uncertainty linked to W+jets and QCD multi-jet background have to be evaluated directly from data themselves, being MC generators not suitable for this purposes. For this reason in this thesis several data-driven methods have been discussed in order to measure the background-related uncertainties using data from experiment.

As shown in chapter 3, the main systematic errors will be due to the jet energy scale (JES) and background normalization. In chapter 2 we showed that using "topmix" pseudo-data the uncertainty on the jet energy scale has been estimated to be $\sim$3% deployed the p_T-balance technique on Z+1 jet events, which reflects in an uncertainty on the $t\bar{t}$ cross-section of about 11%. With real data, it is expected an uncertainty between 5 and 10% at the beginning.

As shown in Chapter 1, latest versions of main Monte Carlo generators are routinely incorporating evaluations at the next-to-leading order and have now reached a large degree of precision with agreements usually well better than 10% in most cases. An example is the $t\bar{t}$ measurements: we evaluated uncertainties due to the different assumptions in the generators to be around

2-3%. What still remains to be done in this respect is the tuning of the MC predictions to data taken at an energy range never reached before. This phase has started in december 2009 with the first pp collisions at $2.3\,TeV$.

The study of the $t\bar{t}$ channel performed in this thesis allowed to develop analysis methods and tools that can be immediately applied on the LHC data that will be collected during 2010 and 2011. The measurement of the $t\bar{t}$ cross section and of its associated systematic uncertainty will be one of the first and most important results that will pave the way for the next discoveries ahead of LHC.

Bibliography

[1] http://hepwww.rl.ac.uk/theory/seymour/herwig/hw65_manual.htm.

[2] http://mcfm.fnal.gov/.

[3] https://twiki.cern.ch/twiki/bin/view/atlas/minimumbiastriggerscintillatorinfo.

[4] http://www.bo.infn.it/atlas_lumi/index.html.

[5] http://www.montecarlonet.org.

[6] https://twiki.cern.ch/twiki/bin/view/atlasprotected/topreferences10tev. 2009.

[7] E. Abouzaid and H. Frisch. Ratio of w+n jets to $z^0/\gamma*$+n jets versus n as a precision test of the standard model. *Physical Review*, D(68 0330014), 2003.

[8] B. S. Acharya, F. Cavallari, C. Corcella, R. Di Sipio, and G. Petrucciani. *Rediscovery of the top quark at the LHC and first measurements*. Nuovo Cimento B, 2008.

[9] B. S. Acharya, F. Cavallari, G. Corcella, R. Di Sipio, and G. Petrucciani. Commissioning atlas and cms with top quarks. *NuovoCim.*, B(123):409–414, 2008.

[10] B. S. Acharya, F. Cavallari, G. Corcella, R. Di Sipio, and G. Petrucciani. Monte carlo generators for top quark physics at the lhc. *NuovoCim.*, B(123):415–220, 2008.

[11] Simone Alioli, Paolo Nason, and Carlo Oleari. Nlo single-top production matched with shower in powheg: s- and t-channel contributions. *arXiv*, hep-ph, Jan 2009.

[12] John Alwall, Pavel Demin, Simon de Visscher, Rikkert Frederix, Michel Herquet, Fabio Maltoni, Tilman Plehn, David L. Rainwater, and Tim Stelzer. Madgraph/madevent v4: The new web generation. *arXiv:0706.2334*, June 2007.

[13] arXiv:hep ph/0003033v1, editor. *Top Quark Physics*, volume 1999 CERN Workshop on SM physics (and more) at the LHC. CERN, CERN, 1999.

[14] S. Ask. Status of the forward physics projects in atlas. *arXiv:0706.0644*, 2007.

[15] ATLAS. https://twiki.cern.ch/twiki/bin/view/atlas/jetetmisspubliccollisionresults.

[16] ATLAS. Prospects for the top pair pair production cross-section at sqrt(s)=10 tev in the single lepton channel in atlas. ATL-PHYS-PUB-2009-087, 2009.

[17] M. Bähr, S. Giesele, M. Gigg, D. Grellscheid, K. Hamilton, O. Latunde-Dada, S. Plätzer, P. Richardson, M. H. Seymour, A. Sherstnev, and B. R. Webber. Herwig++ physics and manual. *The European Physics Journal C*, C(58):639–707, 2008.

[18] A. Buckley. Cedar: tools for event generator tuning. arXiv:0708.2655.

[19] A. Buckley. Tools for event generator tuning and validation. arXiv:0809.4638 IPPP/08/71, DCPT/08/142, MCnet/08/12.

[20] M. Cacciari and G. Salam. Dispelling the n^3 myth for the kt jet-finder. *http://arxiv.org/abs/hep-ph/0512210v2*, 2005.

[21] A. Caldwella, Daniel Kollara, and Kevin Kröninger. Bat – the bayesian analysis toolkit. *doi:10.1016/j.physletb.2003.10.071*.

[22] B. Carithers and P. Grannis. Discovery of the top quark. *Beam Line (SLAC)*, 25(3):4–16, 1995.

[23] S. Catani, M. Seymour, and et al. A general algorithm for calculating jet cross-sections in nlo qcd. *SPIRES*, 1996.

[24] The ATLAS Collaboration. Expected performance of the atlas experiment - detector, trigger and physics. *arXiv*, hep-ex, Jan 2008.

[25] G. Corcella, E. K. Irish, and M. H. Seymour. Herwig for top physics at the linear collider. *http://arxiv.org/abs/hep-ph/0012319v1*, 2000.

[26] Massimo Corradi. Combine. Private communication.

[27] G. Cortiana. Top quark pair production cross section at the tevatron. *arxiv:0804.1684*, 2008.

[28] E.Boos, V.Bunichev, M.Dubinin, L.Dudko, V.Edneral, V.Ilyin, A.Kryukov, V.Savrin, A.Semenov, and A.Sherstnev. Title: Comphep 4.5 status report. *arXiv:0901.4757*, 2009.

[29] E. Barberis et al. The matrix method and its error calculation. D0 Internal Note 4564, 2004.

[30] I. Abi et al. The tracking, calorimeter and muon detectors of the h1 experiment at hera. *Nucl.Instrum.Meth.*, A(386):348–396, 1997.

[31] F. Abe et al. (CDF collaboration). Observation of top quark production in ppbar collisions. *Fermilab-pub*, Mar 1995.

[32] V. M. Abazov et al. (D0 Collaboration). Measurement of the top quark mass in the lepton+jets final state with the matrix element method. *Physical Review*, D(74, 092005), 2006.

[33] C. Amsler et al. (Particle Data Group). The review of particle physics. *Physics Letters*, B667, 1 2008.

[34] F. Fiedler, A. Grohsjean, P. Haefner, and P. Schieferdecker. The matrix element method and its application in measurements of the top quark mass. *arXiv:1003.1316v1*, 2010.

[35] S. Frixione, P. Nason, and C. Oleari. Matching nlo qcd computations with parton shower simulations: the powheg method. *JHEP*, 11, November 2007.

[36] S. Frixione, P. Nason, and B. R. Webber. Matching nlo qcd and parton showers in heavy flavour production. *JHEP*, 08(007), 2003.

[37] G. Soyez G. Salam. A practical seedless infrared-safe cone jet algorithm. arXiv:0704.0292v2, 01 2007.

[38] T. Gleisberg, S. Höche, F. Krauss, M. Schönherr, S. Schumann, F. Siegert, and J. Winter. Event generation with sherpa 1.1. *JHEP*, Feb 2009.

[39] T. Gleisberg, S. Hoeche, and et al. Title: Event generation with sherpa 1.1. *arXiv:0811.4622*, 2008.

[40] K. Hamilton, P. Richardson, and J. Tully. A positive-weight next-to-leading order monte carlo simulation for higgs boson production. *arxiv:0903.4345v3*, May 2009.

[41] B. Holdom, W. S. Hou, M. Mangano, S. Sultansoy, and G. Ünel. Four statements about fourth generation. *arXiv:0904.4698v1*, 2009.

[42] P. B. Kersevan and E. Richter-Was. The monte carlo event generator acermc 2.0 with interfaces to pythia 6.2 and herwig 6.5. *arXiv:hep-ph/0405247v1*, 2004.

[43] M.L. Mangano and et al. Alpgen, a generator for hard multiparton processes in hadronic collisions. *arXiv:hep-ph/0206293*.

[44] B. R. Martin and G. Shaw. *Particle Physics*. Wiley, 2002.

[45] M.L.Mangano, M.Moretti, F.Piccinini, and M.Treccani. Matching matrix elements and shower evolution for top-quark production in hadronic collisions. *JHEP 0701 (2007) 013*.

[46] P. Nason. Recent developments in powheg. *RADCOR 2009 - 9th International Symposium on Radiative Corrections (Applications of Quantum Field Theory to Phenomenology)*, 2009.

[47] K. Nikolopoulos, D. Fassouliotis, C. Kourkoumelis, and A. Poppleton. Event-by-event estimate of muon energy loss in atlas. *IEEE Trans. Nucl. Sci.*, 54(1792–1796), 2007.

[48] A. Quadt. Top quark physics at hadron colliders. *Eur. Phys. J.*, C(48):835–1000, 2006.

[49] F. Maltoni R. Frederix. Top pair invariant mass distribution: a window on new physics. *JHEP 0901:047,2009*, 2009.

[50] A. Rotondi, P. Pedroni, and A. Pievatolo. *Probabilitá Statistica e Simulazione*. Springer, 2005.

[51] R. Di Sipio. http://svnweb.cern.ch/world/wsvn/bod3pdmaker. *http://pchb8.bo.infn.it/wiki/index.php/Portal/Top/BoD3PDMaker*.

[52] R. Di Sipio. Ricerca della supersimmetria nell'esperimento atlas studiando jet+etmiss. In *XCIII Congresso Nazionale della Societa' italiana di Fisica*, volume atticon3780. SIF, 2007.

[53] R. Di Sipio. Ricerca della supersimmetria nell'esperimento atlas tramite lo studio di eventi con 4 jet ed energia trasversa mancante (etmiss). In *XCIV Congresso Nazionale della Societa' Italiana di Fisica*, volume atticon4589. SIF, 2008.

[54] T. Sjöstran and et al. Title: Pythia 6.3 physics and manual. *arXiv:hep-ph/0308153*, 2003.

[55] S. Tarem, Z. Tarem, N. Panikashvili, and O. Belkind. Mugirl - muon identification in the atlas detector from the inside out. *Nuclear Science Symposium Conference Record IEEE*, 1:617–621, 2006.

List of Tables

List of Figures

Acknowledgements

I would like to thank prof. Antonio Zoccoli that made possible all of this and prof. Mauro Villa: they taught me never to accept a number without pondering and how to show my results to an audience of experts.

A special thank goes to dr. Graziano Bruni and dr. Lorenzo Bellagamba, who advised me throughout the development of this work from the very beginning. The two of them taught me how to tackle such a difficult topic and make everything (or most of it) to fit in place.

Part of this thesis has been developed with the supervision of prof. Jonathan Butterworth and dr. Emily Nurse of University College of London. I'm sure I will meet them again in the next years at CERN, and I hope there will be the possibility to work with them again in the future.

Last but not least, I would like to remember prof. Antonio Vitale who taught me never to forget the deepness of classical mechanics and the importance of being humble but firm when dealing with students.

Riccardo Di Sipio
Bologna, Italy
March 14, 2010